UNIVERSITY OF CALIFORNIA SAN DIEGO

Modeling and Design of All-Solid-State Batteries: From Materials to Interfaces

A dissertation submitted in partial satisfaction of the
requirements for the degree
Doctor of Philosophy

in

Materials Science and Engineering

by

Hanmei Tang

Committee in charge:

Professor Shyue Ping Ong, Chair
Professor Zheng Chen
Professor Ying Shirley Meng
Professor Francesco Paesani
Professor Kesong Yang

2019

The dissertation of Hanmei Tang is approved, and it is acceptable in quality and form for publication on microfilm and electronically:

_____

_____

_____

_____

_____

Chair

University of California San Diego

2019

DEDICATION

To all members of my family and friends.

TABLE OF CONTENTS

LIST OF FIGURES

LIST OF TABLES

ACKNOWLEDGEMENTS

I would like to express my special appreciation and thanks to my advisor Professor Dr. Shyue Ping Ong, for your support, guidance, and patience throughout my graduate studies. you have been a tremendous mentor for me. I wish to thank the members of my dissertation committee: professor Zheng Chen, professor Ying Shirley Meng, professor Francesco Paesani, and professor Kesong Yang for offering their time and kind supports.

I gratefully acknowledge the funding received from the Ofiice of Naval Research (ONR) Young Investigator Program (YIP) under the Award N00014-16-1-2621, the National Science Foundation (NSF) SI2-SSI Program under Award No. 1550423, the U.S. Department of Energy under Award No. DE-SC0012118, and the EBI-Shell program under contract number PT78832. I would also like to acknowledge our group members and postdoc alumni, especially the wonderful diffusion subgroup. Thank you for all the fun moments, active discussions, and generous help. A special thank you for the support I received through the collaborative work with Dr. Abhik Banerjee, Dr. Han Nguyen, and Erik Wu, as well as Ryan Stephens and Guy Verbist from Shell Oil Company.

Chapter 2, in part, is a reprint of the material “Atomate: A high-level interface to generate, execute, andanalyze computational materials science workflows” as it appears in Computational Materials Science, Kiran Mathew, Joseph H Montoya, Alireza Faghaninia, Shyam Dwarakanath, Muratahan Aykol, Hanmei Tang, Iek-heng Chu, Tess Smidt, Brandon Bocklund, Matthew Horton, John Dagdelen, Brandon Wood, Zi-Kui Liu, Jeffrey Neaton, Shyue Ping Ong, Kristin Persson, and Anubhav Jain, 2017 Nov 1;139:140-52, and a reprint of the material “Probing solid–solid interfacial reactions in all-solid-state sodium-ion batteries with first-principles calculations” as it appears in Chemistry of Materials, Hanmei Tang, Zhi Deng, Zhuonan Lin, Zhenbin Wang, Iek-Heng Chu, Chi Chen, Zhuoying Zhu, Chen Zheng, and Shyue Ping Ong, 2017 Dec 28;30(1):163-73. The dissertation author contributed to the NEB workflow section and author of the first paper, and was the primary investigator and author of the second paper.

Chapter 3, in full, is a reprint of the material "Understanding the Electrochemical Mechanisms Induced by Gradient Mg^{2+} Distribution of Na-Rich $Na_{3+x}V_{2-x}Mg_x(PO_4)_3$/C for Sodium Ion Batteries" as it appears in Chemistry of Materials, Hui Li, Hanmei Tang, Chuze Ma, Ying Bai, Judith Alvarado, Balachandran Radhakrishnan, Shyue Ping Ong, Feng Wu, Ying Shirley Meng, and Chuan Wu, 2018 Apr 3;30(8):2498-505. All simulations and corresponding data analysis were performed by the dissertation author.

Chapter 4, in full, is a reprint of the material "Probing solid–solid interfacial reactions in all-solid-state sodium-ion batteries with first-principles calculations" as it appears in Chemistry of Materials, Hanmei Tang, Zhi Deng, Zhuonan Lin, Zhenbin Wang, Iek-Heng Chu, Chi Chen, Zhuoying Zhu, Chen Zheng, Shyue Ping Ong, 2017 Dec 28;30(1):163-73. The dissertation author was the primary investigator and author of this paper.

Chapter 5, in full, is a reprint of the material "Revealing Nanoscale Solid-Solid Interfacial Phenomena for Long-Life and High-Energy All-Solid-State Batteries" as it appears in ACS applied materials & interfaces, Abhik Banerjee, Hanmei Tang, Xuefeng Wang, Ju-hsiang Cheng, Han Nguyen, Minghao Zhang, Darren Tan, Thomas Wynn, Erik Wu, Jean-Marie Doux, Tianpin Wu, Lu Ma, George E Sterbinsky, Macwin Dsouza, Shyue Ping Ong, and Ying Shirley Meng, 2019 Oct 23. The dissertation author was the primary investigator and author of this paper.

VITA

2014	B. S. in Processing Engineering, Northeastern University, China
2015	M. S. in Materials Science and Engineering, University of California, San Diego, USA
2019	Ph. D. in Materials Science and Engineering, University of California, San Diego, USA

PUBLICATIONS

Tang H, Deng Z, Lin Z, Wang Z, Chu IH, Chen C, Zhu Z, Zheng C, Ong SP, "Probing solid–solid interfacial reactions in all-solid-state sodium-ion batteries with first-principles calculations", *Chemistry of Materials*, 2017 Dec 28;30(1):163-73.

Banerjee A, Tang H, Wang X, Cheng JH, Nguyen H, Zhang M, Tan D, Wynn T, Wu E, Doux JM, Wu T, "Revealing Nanoscale Solid-Solid Interfacial Phenomena for Long-Life and High-Energy All-Solid-State Batteries", *ACS applied materials & interfaces*, 2019 Oct 23.

Chen C, Deng Z, Tran R, Tang H, Chu IH, Ong SP, "Accurate force field for molybdenum by machine learning large materials data", *Physical Review Materials*, 2017 Sep 15;1(4):043603.

Mathew K, Montoya JH, Faghaninia A, Dwarakanath S, Aykol M, Tang H, Chu IH, Smidt T, Bocklund B, Horton M, Dagdelen J., "Atomate: A high-level interface to generate, execute, and analyze computational materials science workflows.", *Computational Materials Science*, 2017 Nov 1;139:140-52.

Li H, Tang H, Ma C, Bai Y, Alvarado J, Radhakrishnan B, Ong SP, Wu F, Meng YS, Wu C, "Understanding the Electrochemical Mechanisms Induced by Gradient Mg^{2+} Distribution of Na-Rich $Na_{3+x}V_{2-x}Mg_x(PO_4)_3$/C for Sodium Ion Batteries", *Chemistry of Materials*, 2018 Apr 3;30(8):2498-505.

Shi Y, Tang H, Jiang S, Kayser LV, Li M, Liu F, Ji F, Lipomi DJ, Ong SP, Chen Z, "Understanding the electrochemical properties of naphthalene diimide: implication for stable and high-rate lithium-ion battery electrodes", *Chemistry of Materials*, 2018 Apr 27;30(10):3508-17.

Zheng C, Mathew K, Chen C, Chen Y, Tang H, Dozier A, Kas JJ, Vila FD, Rehr JJ, Piper LF, Persson KA, "Automated generation and ensemble-learned matching of X-ray absorption spectra", *npj Computational Materials*, 2018 Mar 20;4(1):12.

Zhou J, Shen L, Costa MD, Persson KA, Ong SP, Huck P, Lu Y, Ma X, Chen Y, Tang H, Feng YP, "2DMatPedia, an open computational database of two-dimensional materials from top-down and bottom-up approaches", *Scientific data*, 2019 Jun 12;6(1):86.

ABSTRACT OF THE DISSERTATION

Modeling and Design of All-Solid-State Batteries: From Materials to Interfaces

by

Hanmei Tang

Doctor of Philosophy in Materials Science and Engineering

University of California San Diego, 2019

Professor Shyue Ping Ong, Chair

All-solid-state batteries show its great potential for being the next-generation source of clean energy barely with safety issues. While current research progress suggests the bottleneck of commercialization of all-solid-state batteries is the high resistivity at the electrode/SE interfaces. The aim of this thesis is to demonstrate how computational efforts can help understand and tackle the interface issues.

The content comprises the following three projects: the methodology development (Chapter 2), the optimization of bulk materials (Chapter 3), and combined experimental and theoretical investigation into reactive interfaces (Chapter 4 & 5).

In the first project, we aimed to develop and improve the computational workflow in

material science research, especially those related to the interfaces. In the first part of this project, the Nudged Elastic Band (NEB) workflow has been developed with high automation and flexibility; and in the second part, an extension to a traditional molecular dynamics workflow specifically for tracking interface reactions has been implemented.

The intrinsic properties of bulk materials are important to the interfacial properties and, thus, the performance of the full-cell battery. In the second project, we illustrated a computational aided design of bulk material, the Mg-doped $Na_3V_2(PO_4)_3$ cathode $Na_{3+x}V_{2-x}Mg_x(PO_4)_3$/C.

The third project includes chapters 4 & 5, which are interfacial investigations on Na-ion and Li-ion, respectively. In chapter 4, we have demonstrated how thermodynamic approximations based on assumptions of fast alkali diffusion and multi-species equilibrium can be used to effectively screen combinations of Na-ion electrodes, solid electrolytes and buffer oxides for electrochemical and chemical compatibility. In addition to the thermodynamic approximation, *ab initio* molecular dynamics simulations of the $NaCoO_2$/Na_3PS_4 interface model predict that the formation of SO_4^{2-}-containing compounds and Na_3P are kinetically favored over the formation of PO_4^{3-}-containing compounds, which has been validated through XPS recently. Chapter 5 investigate the source of reactivity between the sulfide solid electrolyte Li_6PS_5Cl (LPSCl) and the high-voltage cathode $LiNi_{0.85}Co_{0.1}Al_{0.05}O_2$ (NCA). And both experimental and computational results demonstrated improved stability between NCA and LPSCl after incorporation of the $LiNbO_3$ coating.

Chapter 1

Introduction

1.1 Background of Research

A battery is a device converting storing the electrical energy in the form of chemical energy, and this electrochemical process is reversible in a rechargeable battery (or a secondary battery). A typical SSAB consists of a positive and a negative insertion electrode, and the mobile ion-conducting electrolyte in between. A schematic diagram of a rechargeable alkali-ion battery is shown in Figure 1.1 during its discharge process or the discharge electrochemical reaction. In the discharge process, mobile ions move from the anode (electropositive electrode) side to intercalate into the cathode (electronegative electrode) side through the solid electrolyte. At the same time the electrons (e^-) move from anode to cathode through an external wire. And the alkali ions A^+ move to the opposite direction during the charging process.

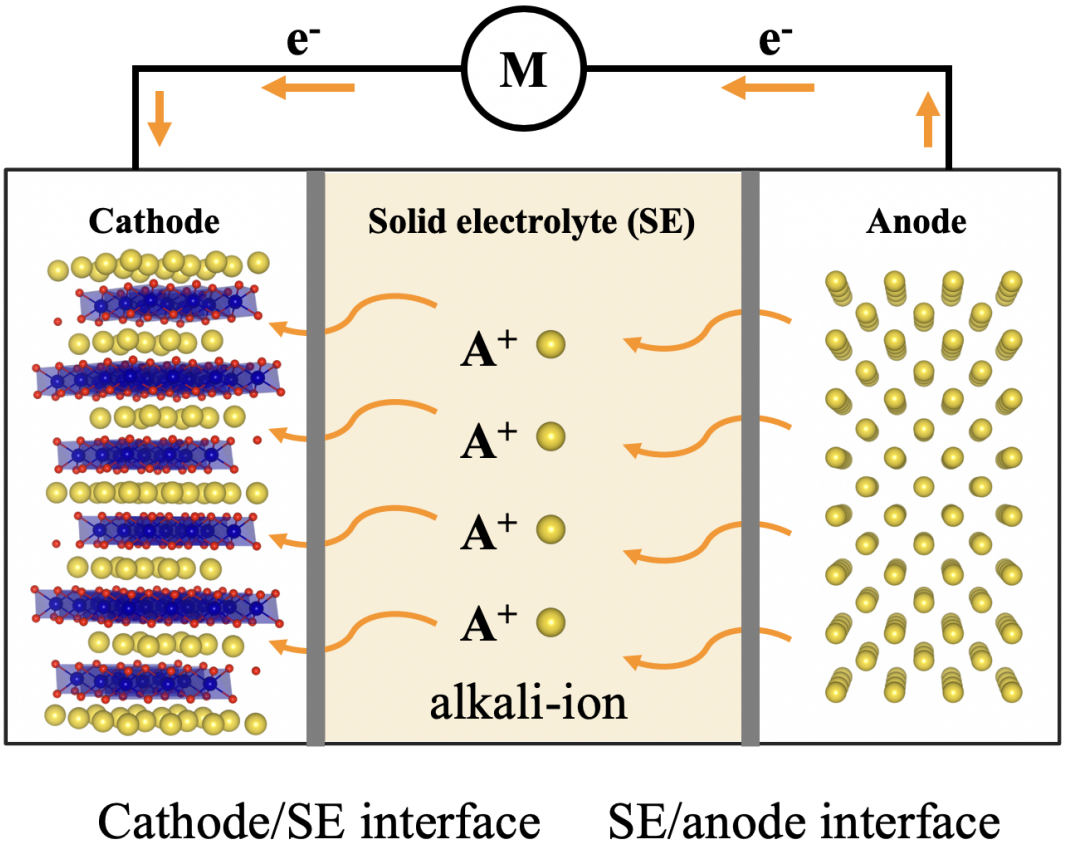

Figure 1.1: Schematic illustration of a rechargeable all-solid-state alkali-ion (A^+, yellow circles) battery during a discharge electrochemical reaction. During discharge process, mobile ions move from the anode side to intercalate into the cathode side through the solid electrolyte. In the same time the electrons (e^-) move from anode to cathode through an external wire.

Energy storage devices are critical in many aspects of modern society, such as portable devices, electric vehicles, and the utility grid. [1] The demands for rechargeable batteries that have high energy density, long cycle lives without safety issues are rapidly growing. Moreover, developing better electrochemical systems are critical to the environment we live in. Switching from fuels to electricity is one of the critical changes that have to be made to meet the requirements of global decarbonization. [2] These have been motivating a wide range of research and development efforts over the past decades.

The history of the battery can be traced back to 1800 when Volta's cell was invented. Until very recently in 1967, sodium β-alumina was found to have high ionic conductivity, which

eventually opened up the possibility to build rechargeable all-solid-state batteries using a solid electrolyte (SE). [3] An all-solid-state alkali-ion battery (SSAB) is considered as a safer, more energy-dense alternative to the conventional organic-liquid-electrolyte-based batteries. [4] At the same time, SSABs potentially provide significant gains in system-level energy densities through device optimization (e.g., stacking) or enabling new chemistries (e.g., high-voltage cathodes and alkali metal anodes). [5, 6].

1.2 Review of Computational Studies on Interfaces

In the past decades, research has been a focus on improving the intrinsic conductivity of electrode and electrolyte materials. However, the performance of current SSABs still falls far short of expectations due to a lack of electrode/SE combinations that yield high energy density and high cycling stability. For example, the thiophosphate-type superionic conductors have emerged as some of the most promising SE materials in terms of high ionic conductivity, their compatibility with electrodes in terms of electrochemical and chemical stability are still a significant impediment to their practical application. [7] The high instability and resistivity at the the interfaces can be a result of the incompatible electrode and SE, the poor mechanical contact, or a high internal strain.

Density functional theory (DFT) simulations have been proven as a powerful tool to model and even design bulk material with desired properties (e.g. lower activation energy for superionic conductors), reveal the interfacial reactions, as well as help understand the underlying mechanism of experimental observations. [8, 9, 10, 11]

Computational approaches have been widely applied in studying bulk components of SSABs, contributing significant insights into understanding the nature of solid-state ion conduction property and diffusion mechanism. The most commonly-used computational tools are molecular dynamics (MD) and Nudged Elastic Band (NEB) calculations. For example, *ab initio* molecular

dynamics (AIMD) was used in the computation-assisted discovery of the fast conducting Na ion electrolyte $Na_{10}SnP_2S_{12}$, which predicted a migration barrier (0.317 eV) close to the experiment result (0.354 eV). [12] Using first principles calculations, Chu et al. revealed that Cl^- doping with the concomitant introduction of Na vacancies will result in enhanced ionic conductivity of $>$ 1 mS/cm at 300 K in the t-Na_3PS_4 superionic conductor, and this prediction has been successfully verified by experiments in a full TiS_2/Cl-Na_3PS_4/Na cell. [13]

Modeling and simulations for interfaces are much more complex than those in bulk materials. In general, computational approaches can be roughly categorized into thermodynamic and kinetic methods. Thermodynamic approaches provide fast estimations of the compatibility of a given electrode/SE interface. Ong, Mo, and Ceder [14, 15] first proposed the grand potential approximation to predict SE phase equilibria at the high and low voltage limits in the $Li_{10}GeP_2S_{12}$ (LGPS) family of SEs. The predicted electrochemical decomposed products have been validated through XPS. [16] A number of electrode/SE combinations have been evaluated with regard to the chemical and electrochemical stability in later works, [10, 9, 17, 11] and the intrinsic instability of interfaces and the potential benefit of the interphase layer have been revealed.

Kinetic methods are more powerful tools to visualize the interface evolution, however; they are very rarely applied in computational studies on interfaces in SSABs. Tian et al. reported a combined experimental and theoretical study of the thiophosphate-type electrolyte and layered cathodes. [18] A more comprehensive study in interfacial reactions of sodium-ion batteries are illustrated in the more recent work by the author. [11]

1.3 Project Overview

A tightly integrated combination of first principles calculations and experiments can guide and accelerate the design and optimization of electrode/SE combinations for Li and Na-ion all-solid-state batteries. In this dissertation, four first-authored and collaborative projects are put

together to demonstrate computational effort to tackle interface issues in SSABs.

1.3.1 Project 1: Workflow and analysis package development

DFT simulation is proven to be an accurate and reliable approach in material science. These calculations are, however, very costly in time and computing resources. When it comes to high-throughput screenings, the large amount of data to be managed could cause problems. Atomate is a package developed to meet this requirement. The highly repetitive tasks can be well-managed by workflow, which automate DFT calculations and post-analyses.

Diffusion properties such as activation energy and conductivity are key to solid-state ionic conductors. The most commonly used approaches are AIMD and NEB. In this project, we developed an automatic NEB workflow accepting flexible inputs. We also implemented a post-analysis module for the traditional AIMD workflow, which accepts simulation in both NVT and NPT ensembles and a series of visualization tools.

1.3.2 Project 2: Optimization of bulk materials

In the second project, we aimed to improve the conductivity of the well-known sodium cathode material $Na_3V_2(PO_4)_3$ by high-throughput all available divalent dopants, which are Ni, Mg, Cu, Cr, Zn, Pd, Ag, Ca, Sr and Ba. The stability of the doped compositions with regard to the doping concentration is analyzed. The results indicate doping with Mg^{2+} and Ni^{2+} are energetically-preferred in $Na_3V_2(PO_4)_3$ at V sites and additional Na are introduced to keep charge neutral. Experiments also verified the improved conductivity in $Na_{3+x}V_{2-x}Mg_{0.05}(PO_4)_3$ at 0.05 doping concentration.

1.3.3 Project 3: Computational investigation of solid-solid interfaces

In the third project, we present two stand along works on Na-ion and Li-ion battery, respectively.

The first project is a hierarchical computational approaches to model heterogeneous interfaces in SSABs. In studying interfaces, there are thermodynamic and kinetic approximations that can applied together to get a more accurate description of the compositions change at the reactive interfaces. We evaluated well-known electrode/SE(buffer) combinations using multiple criteria, and we have identified the source of reactivity at oxide cathode and thiophosphate SE is the formation of PO_4^{3-}. Additionally, we also identified a few promising buffer materials, Sc_2O_3, SiO_2, TiO_2, ZrO_2 and HfO_2.

The second project is a combined experimental and computational work on Li-ion battery at NCA/LPSCl interface. Thermodynamic and kinetic approaches have identified the source of reactivity at this interface is the formation of Li_3PO_4, M_xS_y and LiCl. This conclusion is consistent in experimental observation, prediction using thermodynamic approaches. Formation of the elemental S have been identified from AIMD trajectories, which agrees with the electrochemical product found experimentally. This is also reported the first time that AIMD is able to simulate the electrochemical reaction.

1.3.4 Chapter Index

The dissertation is divided into the following chapters. A brief description for each subsequent chapter is listed as below:

- Chapter 2 is the methodology in studying interfaces, including the automation of computational workflow and analysis package development.
- Chapter 3 contains a case study of computational aided design and optimization of the superionic conductor by comparing diffusion properties among different divalent-doped

$Na_3V_2(PO_4)_3$.

- Chapter 4 is a hierarchical study of interfaces in all-solid-state sodium ion batteries.
- Chapter 5 is a combined experimental and computational investigation for the reactive interface NCA/LPSCl.

Chapter 2

Methodology

2.1 Computational Materials Science Workflows

2.1.1 Overview

Computational materials science methods are continually growing in predictive power due to advances in theory, computing, and software development. Today, there exists several examples of new functional materials such as batteries, [19, 20] thermoelectrics, [21, 22] and catalysts, [23, 24] that have been designed primarily through such methods [6] and the use of computations has in some cases proven to save significant R&D costs and time. As computational methods become applicable to a greater span of problems, the audience that could potentially benefit from their use grows. However, computational softwares such as density functional theory calculation codes typically require careful and manual setup of many parameters. The interface for performing calculations is typically highly tuned for performing a few very detailed studies. However, emerging applications efforts towards high-throughput screening for functional materials and building libraries of materials properties may involve thousands or even millions of calculations, for which it would be impossible to manually generate input files or fix various error messages that occur during such calculations. In addition, learning to correctly conduct multiple

different types of analyses is difficult: calculation procedures are typically not well documented or even standardized, and certain types of calculations involve multiple, labor-intensive steps prone to errors. These difficulties can lead to inefficient and in some cases incorrect usage of these tools, hampering user productivity and data integrity. Thus, there have previously been multiple efforts to build abstraction layers intended to facilitate the use of computational methods. Such efforts include commercial offerings such as Medea, Materials Studio, and GoVasp (now part of Medea) and academic codes such as AiiDA, MAST, qmpy/OQMD, ASE, AFLOW, the Harvard Clean Energy Project, iochem-bd, Quixote, and our own previous efforts (MPWorks and an earlier Java/SQL-based framework). The common goals of these frameworks are multi-fold. First, they enhance productivity by freeing researchers to focus their attention on scientific aspects of the problem rather than the minutia of calculation execution. Second, they create a set of easily replicable and testable community standards for simulations. Finally, they enable new applications such as high-throughput computing by automating many tasks that are typically performed manually.

Atomate is a redesign of our previous Java/SQL based high-throughput infrastructure [25] as well as our second-generation Python/Mongo MPWorks effort, which powered the Materials Project [26] database of over 1 million individual calculations. Atomate aims to improve the extensibility, usability, and composability of workflows over our previous efforts. One major distinguishing feature of atomate versus many similar efforts is that it is built on top of multiple powerful open-source tools including pymatgen (software to generate/manipulate structures, create input files and post process output files) [27], custodian (software to recover from calculation errors), and FireWorks (a workflow library) [28]. It also makes use of external libraries such as Phonopy for specialized calculations. This design allows almost all the source code of atomate itself to be dedicated to high-level specifications of calculation procedure. In addition, atomate contains tools both for executing calculations as well as managing the results within a well-structured database so that one can not only perform calculations but efficiently

analyze their outputs.

2.1.2 Atomate Nudged Elastic Band (NEB) Workflow

Understanding the diffusion process and mechanism is crucial for superionic conductors. Climbing-image nudged elastic band (CI-NEB) approach has been widely employed to study the kinetics of materials such as the migration barriers of the mobile ions. [29] Compared to the traditional NEB approach [30], CI-NEB can accurately determine the transition state along the migration path (and hence the associated migration barrier) with less computational effort. A standard CI-NEB calculation consists of five major steps (see the NEB workflow Figure 2.1):

1. initial relaxation of the parent structure that does not contain any impurities/defects.
2. construction of the initial and final structures of the migration path (also known as end-point structures) from the parent structure.
3. relaxation of the two end-point structures.
4. construction of the initial guess of the intermediate structures (also known as the image structures) along the migration path.
5. CI-NEB calculation that yields the minimum-energy migration path between the two end-point structures, in which the transition state is also identified.

In atomate, we implement a CI-NEB workflow that can be launched through three different methods (see Figure 2.1). As a first method, the user can provide a parent structure along with a pair of atomic indices that define the migration path under the single vacancy diffusion mechanism. Alternatively, the user can provide two end-point structures under different diffusion mechanisms. Note that the construction of the image structures is required in both scenarios. This can be achieved by using either the traditional linear interpolation of the atomic coordinates between

the end-point structures or the image dependent pair potential (IDPP) approach [31]. The former is implemented in pymatgen itself whereas the latter is implemented in pymatgen-diffusion, an add-on to the pymatgen package [27, 32]. The IDPP approach has been shown to substantially improve the convergence speed of CI-NEB calculations and is thus set as the default approach for initial path construction. In the third scenario, the user provides a complete migration path comprising both end-point and image structures. To further accelerate the convergence speed of CI-NEB, the default workflow performs two rounds of CI-NEB calculations, wherein looser input parameters are used in the first round and tighter input parameters are used in the second round of calculations. All the preset settings in the CI-NEB workflow have been tested and tend to improve the overall efficiency in CI-NEB calculations, although the user can tune these parameters as needed for their study.

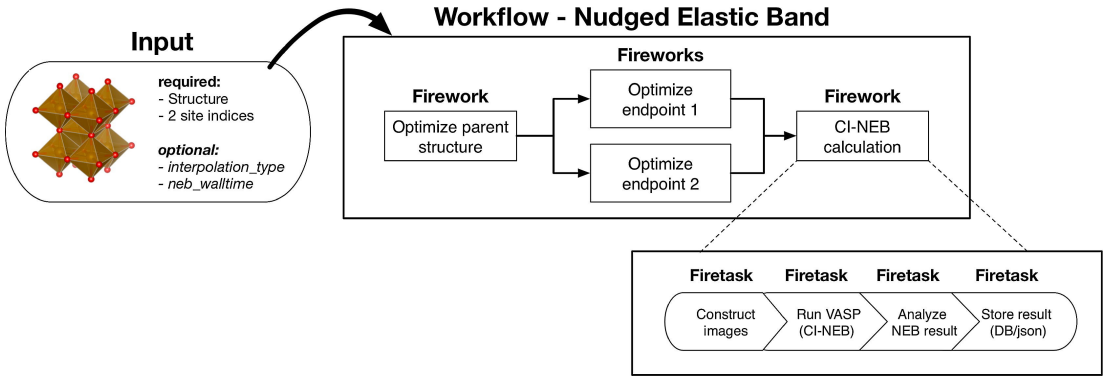

Figure 2.1: Workflow diagram for Nudged Elastic Band (NEB) workflow: NEB workflows proceed via optimization of an initial parent structure and two end points. From these, an intermediate reaction path is estimated and a CI-NEB calculation conducted. The CI-NEB workflow also features automatic restart functionality since NEB calculations often exceed allowed walltimes on supercomputing resources. CI-NEBs may also be calculating using two images, rather than a single parent structure with specified sites.

2.1.3 *ab initio* molecular dynamics (AIMD) Workflow

In addition to NEB calculations, *ab initio* molecular dynamics (AIMD) is another frequently used simulation to get diffusion properties. Dr. Ong group has developed an in-house software platform for the automated *ab initio* molecular dynamics workflow, a standard database

with a user-friendly interface. [32]

As an extension of the AIMD workflow, a post-analysis of the trajectories using the radial distribution functions (RDFs) has been used to detect the changes in bonding during the simulation. It is useful, especially in revealing the chemical process occurring at the solid-solid heterogeneous interface. This post-analysis has been coded into Pymatgen-diffusion package.

Another useful extension has been made to the original AIMD workflow is the NpT-NVT scheme, which further makes the simulation more realistic and reliable. The initial NpT section greatly release the artifical strain, and thus eliminate those unreasonable reaction at the interface. For example in the simulation for hetorogeneous interface in the all-solid-state batteries, the simulations in the NpT ensemble at 300 K were first carried out until the volume of the cell is converged to within 2%. This step is necessary to minimize the interfacial stress caused by the lattice misfit, and typically occurs within ˜4 ps of simulation time. For large systems with a few hundred of atoms, e.g. the solid-electrolyte/electrode interfaces studied in this work, the accessible time scales are even shorter. Figure 2.2 below plots the pressure and volume variation of the $NaCoO_2$/Na_3PS_4 interface simulation as a function of time. It clearly shows that both pressure and volume converge within the first 2-4 picoseconds.

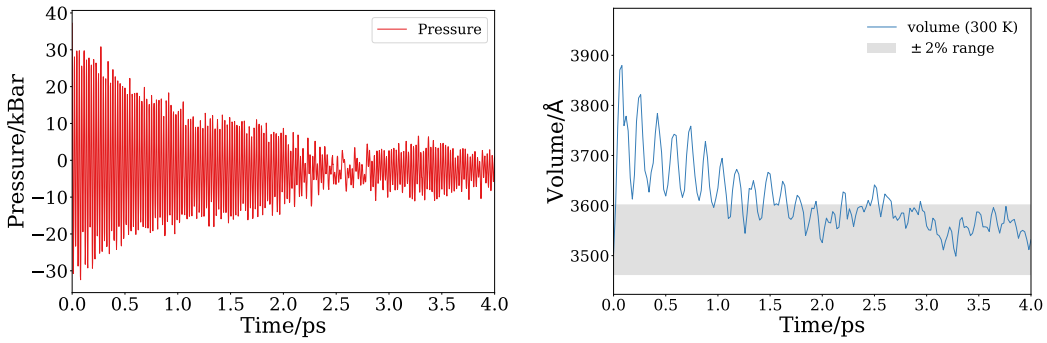

Figure 2.2: Pressure and volume variation of $NaCoO_2$/Na_3PS_4 interface as a function of time. Both pressure and volume converge within the first 2-4 picoseconds in the simulation.

2.2 Models for Solid-Solid Interfaces

Here, we will outline the general principles behind the various first principles approaches to predict solid-solid interface equilibria/reactivity. Figure 2.3 provides an overview of the three models that will be discussed in this section, arranged in the order of complexity. The bottom two models are based on thermodynamic approximations, and they have been used in previous works on Li SEs, [15, 14, 10, 17, 9, 33, 34] while the model on the top of the pyramid is an explicit interfacial model simulated at finite temperatures. We will discuss these models in the context of SSNaBs, though the models are similarly applicable to SSLiBs.

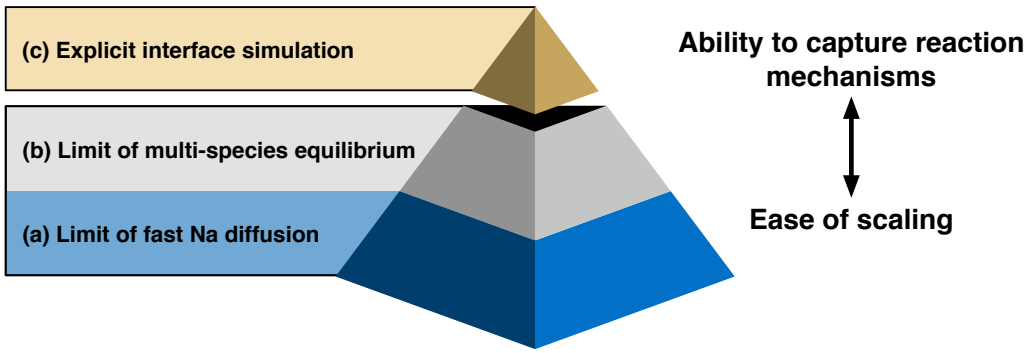

Figure 2.3: Hierarchy of models for solid-solid interface reactions. (a) Fast diffusion of alkali-ion (grand potential phase diagram); (b) multi-species equilibrium e.g., slow diffusion or extremely long time scale (reaction prediction using pseudo-binary phase diagram); (c) *ab initio* molecular dynamics (AIMD), accounting for different multi-species mobilities and interactions at finite temperatures. The thermodynamic models at the bottom of the pyramid are computationally less costly but make various assumptions on species mobilities. The AIMD approach captures kinetics at finite temperatures, but the high computational cost limits such simulations to small model systems and short simulation time scales.

2.2.1 Approach 1: Fast diffusion of alkali-ion

Under the assumption that Na is the main mobile specie, the SE material can be treated as an open system to Na described by chemical potential μ_{Na}. The SE is subjected to a maximum range of electrochemical potential when the battery is fully charged, where the desodiated cathode is effectively a Na sink at low μ_{Na} and the sodiated anode is effectively a Na source at high

μ_{Na}. The electrochemical window of a SE is essentially the μ_{Na} or voltage range in which the composition of SE is stable against either Na extraction or insertion, which can be estimated using the DFT grand potential phase diagram at various μ_{Na}.[35] The Na grand potential is given by

$$\phi(c,\mu_{\text{Na}}) = E(c) - \mu_{\text{Na}}N(c), \tag{2.1}$$

where $E(c)$ is the total energy from density functional theory (DFT) calculations, and $N(c)$ is the number of Na atoms of that particular phase with composition c. μ_{Na} is related to the voltage V with respect to the Na metal anode by

$$V = -\frac{\mu_{\text{Na}} - \mu^0_{\text{Na}}}{e}, \tag{2.2}$$

where μ^0_{Na} is the Na chemical potential of Na metal, and e is the electron charge.

In essence, one can view this as an estimate of the **electrochemical (grand canonical) stability** of the SE with respect to voltage. Henceforth, we will simply refer to this estimate as the **electrochemical stability** for brevity.

2.2.2 Approach 2: Multi-species equilibrium

In this approach, the assumption is that the two materials at a heterogeneous interface react to form the most favorable products under full thermodynamic equilibrium.[33, 17, 9, 34] The most favorable reaction is determined by constructing the pseudo-binary phase diagram between the two materials, a and b (e.g., between the $NaCoO_2$ cathode and the Na_3PS_4 SE), and finding reaction ratio resulting in the most negative reaction energy:

$$\Delta E(c_a,c_b) = \min_{x\in[0,1]} \frac{1}{N}\{E_{\text{eq}}[xc_a + (1-x)c_b] - xE[c_a] - (1-x)E[c_b]\}, \tag{2.3}$$

where c_a, c_b are the compositions of phases a and b, respectively, x is the ratio of c_a, and $E[c_a]$, $E[c_b]$ are the DFT total energy of phases a and b, respectively. $E_{\text{eq}}(c)$ is the energy of phase equilibria at composition c. N is a normalization factor, which is equal to the total number of atoms involved in the reaction. $\Delta E(c_a, c_b)$ may then be regarded as an estimate of the **chemical (equilibrium) stability** of the two materials with each other. Henceforth, we will simply refer to this estimate as the **chemical stability** for brevity. The more negative the $\Delta E(c_a, c_b)$, the greater the thermodynamic driving force for the two materials to react at a heterogeneous interface.

In addition, we can also estimate the volume change ΔV as a result of the reaction at a heterogeneous interface by comparing the volumes to products of the reaction to that of the reactants in the reaction. The final DFT relaxed volumes of each reactant/product are used in this estimate. A negative ΔV means that the volume of the products is smaller than those of the reactants, which may cause the formation of voids and loss of contact at the interface. On the other hand, a positive ΔV means that the volume of the products is larger than those of the reactants, which may cause the build-up of stresses and cracks at the interface.

2.2.3 Approach 3: Explicit interface simulation

In the third approach, finite temperature *ab initio* molecular dynamics (AIMD) simulations are carried out on explicit models constructed for solid-solid interfaces in a SSNaB, as shown in Figure 2.4.

2.2.4 Interface construction

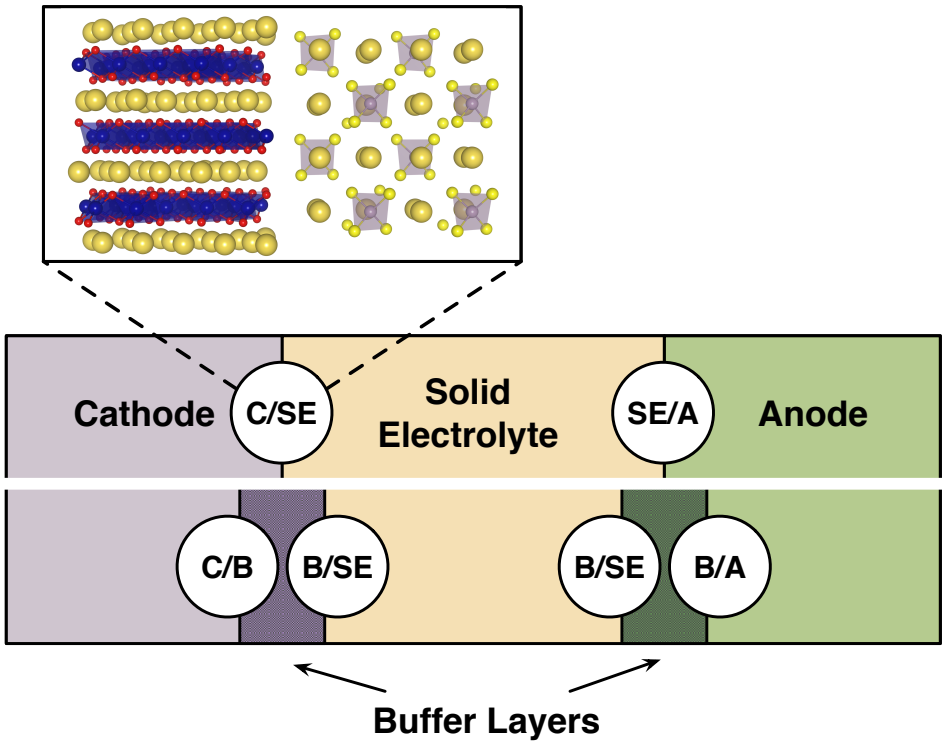

Figure 2.4: Schematic diagram of interfaces in SSNaBs without buffer layers (upper) and with buffer layers (lower). Letters in the figure denote the cathode (C), the solid electrolyte (SE), the anode (A) and the buffer layer (B).

The interface models were constructed using slabs of electrode, buffer layer or SE material. The orientation of the cathode slab was chosen such that it is a low-energy surface appearing in the calculated Wulff shape [36] that also presents facile channels for Na diffusion. A similar criterion was used in previous work. [37] The spacing between two materials was initially set at 2.5 Å. To achieve a good compromise between the number of atoms in the model and the misfit strain at the interface, we used the algorithm proposed by Stradi et al. [38] to identify the optimal supercell combination based on the following criteria:

- Lattice misfit parameter $m < 6\%$.

$$m = \frac{|p_i - p_s|}{p_i} \times 100\% \tag{2.4}$$

where p_i and p_s are perimeters of the unit cell ab-plane of the interface and the slab.

- Mean absolute strain $\bar{\varepsilon} < 10\ \%$.

$$\bar{\varepsilon} = \frac{|\varepsilon_{xx}| + |\varepsilon_{xy}| + |\varepsilon_{yy}|}{3} \tag{2.5}$$

where ε_{xx}, ε_{xy} and ε_{yy} are components of plane strain caused by matching one slab with another.

Changes in bonding were tracked over the course of AIMD simulations of at least 22 ps (with transition metal) and 160 ps (without transition metal) by comparing the radial distribution functions (RDFs) of various species at the interface with those of all known reference crystalline compounds within the chemical system of interest. For instance, in the case of Na_3PS_4/Na interface, the interfacial RDFs are compared with those of all known compounds in the Na-P-S chemical space, i.e., all Na, P, S, Na_xP_y, Na_xS_y, P_xS_y and $Na_xP_yS_z$ phases in the Materials Project (MP) database[26, 39] with an energy above hull (E_{hull}) of less than 20 meV/atom. The E_{hull} is a measure of the stability of a reference material, and here, we limit the reference collection to relatively stable phases. We will discuss our systematic process of elimination to identify matching reference compounds, e.g., by noting the absence or presence of well-defined bond lengths such as those for PO_4^{3-}, SO_4^{3-}, PS_4^{3-} tetrahedra, in the Results section. It should also be noted that we did not explicitly set any interfacial reactions are driven by the inherent concentration/chemical potential gradients across the interface, and the voltage is not explicitly set in the AIMD simulations.

2.3 Acknowledgement

Chapter 2, in part, is a reprint of the material “Atomate: A high-level interface to generate, execute, andanalyze computational materials science workflows” as it appears in Computational

Materials Science, Kiran Mathew, Joseph H Montoya, Alireza Faghaninia, Shyam Dwarakanath, Muratahan Aykol, Hanmei Tang, Iek-heng Chu, Tess Smidt, Brandon Bocklund, Matthew Horton, John Dagdelen, Brandon Wood, Zi-Kui Liu, Jeffrey Neaton, Shyue Ping Ong, Kristin Persson, and Anubhav Jain, 2017 Nov 1;139:140-52, and a reprint of the material "Probing solid–solid interfacial reactions in all-solid-state sodium-ion batteries with first-principles calculations" as it appears in Chemistry of Materials, Hanmei Tang, Zhi Deng, Zhuonan Lin, Zhenbin Wang, Iek-Heng Chu, Chi Chen, Zhuoying Zhu, Chen Zheng, and Shyue Ping Ong, 2017 Dec 28;30(1):163-73. The dissertation author contributed to the NEB workflow section and author of the first paper, and was the primary investigator and author of the second paper.

Chapter 3

Understanding the Electrochemical Mechanisms Induced by Gradient Mg^{2+} Distribution of Na-Rich $Na_{3+x}V_{2-x}Mg_x(PO_4)_3$/C for Sodium Ion Batteries

3.1 Introduction

Because of the low cost and abundance of sodium element in the Earth's crust, sodium ion batteries (SIBs) are now attracting more attention for grid-scale energy storage applications. [40, 41, 42, 43] In addition, because of the lower half-reaction potential of SIBs than that of lithium ion batteries (LIBs), [44] SIBs can be used in electrolyte systems with lower decomposition potential such as water-based electrolytes, which makes it inexpensive compared to LIBs. Recently, SIBs have been investigated extensively including cathodes, anodes, and electrolytes. However,

practical applications of SIBs are limited because of the larger ionic radius of the sodium ion compared to that of the lithium ion (1.02 Åfor Na^+ vs 0.76 Åfor Li^+) and higher equivalent weight of Na than that of Li. [45, 46] Thus, it is necessary to find more suitable electrode materials with good structural stability and electrochemical performance to enable more SIB applications.

Because of the highly covalent three-dimensional framework that generates large interstitial space where sodium ions may easily diffuse during the charging/discharging process, [47, 48, 49, 50, 51] NASICON-structured compounds are considered as prospective cathode material for sodium ion batteries [52, 53, 54] and hybrid ion batteries. [55] Among various sodium super ion conductor (NASICON)-structured compounds, $Na_3V_2(PO_4)_3$ shows superior performances. It is worth mentioning that $Na_3V_2(PO_4)_3$ possesses a rhombohedral $R\bar{3}c$ symmetry which benefits sodium ion diffusion. Moreover, $Na_3V_2(PO_4)_3$ displays a high voltage plateau (3.4 V) that is relatively higher than that of most other Na ion battery (NIB) cathode materials. [56] The high specific energy density ($\sim$400 Wh/kg) and high thermal stability of $Na_3V_2(PO_4)_3$ are suitable for large-scale energy storage.[57, 58]

Although $Na_3V_2(PO_4)_3$ has many advantages, low electrical conductivity (similar to $Li_3V_2(PO_4)_3$ and $LiFePO_4$) significantly limits its electrochemical performance. [59, 60, 61] Until now, coating various carbon materials, reducing the particle size, and doping metal ions have been adopted to improve the electrochemical performance and cation doping is an effective and simple way to modify $Na_3V_2(PO_4)_3$. Mg^{2+}, [62] Fe^{3+}, [63] Cr^{3+}, [64] Al^{3+}, [65] Mn^{2+}, [66, 67] K^+, [49] and Ni^{2+} [68] have been doped into $Na_3V_2(PO_4)_3$. The results show that all doped samples display enhanced electrochemical performance. However, most of the papers were committed to improving the electrochemical performance, while the mechanistic understanding on the effects of cation doping of $Na_3V_2(PO_4)_3$ is still ambiguous and not comprehensive.

In this work, we first use density functional theory (DFT) method to determine the most preferred doping mechanism for Mg. Then we implemented a screening process to identify all possible divalent dopants under this mechanism. We find the following: (1) Mg^{2+} tends to

substitute on the V site and extra sodium ions are introduced to keep the charge neutral; (2) Ni^{2+}- and Mg^{2+}-doped structures are of the highest chemical stability, which corresponds with our initial guess; and (3) the cost-effective Mg ion was chosen to be doped into $Na_3V_2(PO_4)_3$. To further determine the optimal doping concentration of Mg^{2+}, where computational screening is hindered by the max atom number of the unit cell, a series of Mg^{2+}-doped Na-rich $Na_{3+x}V_{2-x}Mg_x(PO_4)_3$/C ($x$ = 0, 0.05, and 0.1) were synthesized by the sol–gel method. The effects of Mg^{2+} doped on the crystal structure, Mg^{2+} doping site, and the distribution of Mg^{2+} within the particles for the electrochemical performance will be discussed further in detail.

3.2 Methods

3.2.1 Sample Preparation

All $Na_{3+x}V_{2-x}Mg_x(PO_4)_3$/C ($x$ = 0, 0.05, and 0.1) samples were synthesized by the sol–gel method. Stoichiometric amounts of NaOH, NH_4VO_3, $NH_4H_2PO_4$, $Mg(CH_3COO)_2$, and citric acid were used as raw materials. First, NH_4VO_3 was dissolved in deionized water and stirred at 80 °C. Citric acid solution, NaOH solution, $Mg(CH_3COO)_2$ solution, and $NH_4H_2PO_4$ solution were added into the above NH_4VO_3 solution while stirring everything at 80 °C. After several hours, all the water evaporated and the solution subsequently turned into a gel. The gel was calcinated at 800 °C in the flowing argon atmosphere for 8 h to obtain $Na_{3+x}V_{2-x}Mg_x(PO_4)_3$/C with the respected composition (x = 0, 0.05, and 0.1). All chemicals were used directly without any further purification.

3.2.2 Characterization

X-ray diffraction (XRD) measurements on all the materials were performed using Cu Kα radiation to identify the crystalline phase. Rietveld refinement was performed using FullProf

software. Na-ion conductivity was measured with electrochemical impedance spectroscopy using an impedance analyzer Solartron 1255B) in the frequency range of 100 kHz to 10 mHz at 25, 50, and 60 °C. Inductively coupled plasma (ICP) analysis was performed using a PerkinElmer 3700 optical emission plasma spectrometer.

The structure of the Na-rich $Na_{3.05}V_{1.95}Mg_{0.05}(PO_4)_3$/C sample was investigated by using a FEI Tecnai G2 F20 transmission electron microscope equipped with selected area electrode diffraction patterns and the scanning transmission electron microscope (STEM) operated at 200 kV.

3.2.3 Computational Methods

Density Functional Theory Calculations

All density functional theory (DFT) calculations were performed using Vienna Ab initio Simulation Package [69] within the projector augmented wave method. [70] The Perdew-Burke-Ernzerhof generalized gradient approximation [71] with Hubbards correction (GGA+U) was used for the exchange-correlation functional. For all DFT energy calculations, a plane-wave cutoff of 520 eV and a k-point density of at least 1000/(number of atoms in unit cell) and spin-polarized condition were used for all cases. All structure manipulations and postanalysis were carried out using Python Materials Genomics (Pymatgen) package. [27]

Structure Generation

The initial disordered structure was obtained from Inorganic Crystal Structure Database (ICSD) [72] ($Na_{3.803}V2.5(PO_4)_3$: ICSD no. 248140). The lowest energy structure was identified by computing the ground-state energy of all symmetrically distinct atomic configurations [32] enumerated using the algorithm of Hart and Forcade. [73]

For doped chemistries, all symmetrically distinct ordering of $Na_{3+x}V_{2-x}M_x(PO_4)_3$ and

$Na_3V_{2-x}M_x(PO_4)_3$ were enumerated using the aforementioned algorithm for x = 0.0625, 0.125, 0.25, and 0.5.

Divalent Dopants Selections

Some divalent ions are not suitable for dopants; thus, they are excluded: (1) Radioactive elements: Tc and Pm and from Bi to the end of the periodic table. (2) Nobel metals: Rh, Ir, Pt, and Au. (3) Elements with toxicity: Cd and Hg. (4) Elements where the divalent state is not available: alkali metals, noble gases, etc. As a result, Ni, Mg, Cu, Cr, Zn, Pd, Ag, Ca, Sr, and Ba are selected as potential dopants.

Phase Stability and Dopant Formation Energy

The phase stability of a given compound $Na_xV_yP_zO_uM_v$ (M is the dopant species) was estimated using the energy above the convex hull (E_{hull}) [35] in the corresponding Na–V–P–O–M phase diagram. Precomputed data used in phase diagram construction can be obtained from the Materials Project (MP) [26] database using the Materials Project API. [39] The E_{hull} value of stable phases is 0 meV/atom. The higher the E_{hull} is, the less stable the compound is predicted to be. In this work, an E_{hull} value of 20 meV/atom is chosen as the cutoff value beyond which the chemistry is considered to be unstable to be synthesized.

The neutral dopant formation energy was calculated using the formalism reported by Wei et al., [74] which indicates the dopability of the dopant into the host material. Specifically, the dopant formation energy is calculated using the formalism:

$$E_f[M] = E_{tot}[M] - E_{tot}[bulk] - \sum_i n_i \mu_i, \tag{3.1}$$

where $E_{tot}[M]$ and $_{tot}[bulk]$ are the total energies of the structure with and without the neutral dopant M, respectively. n_i is the number of species i that is being added ($n_i > 0$) or removed ($n_i < 0$). μ_i is the atomic chemical potential of species i that varies based on different

experimental conditions. Then the lower bound of the dopant formation energy was calculated, which is equal to the difference of decomposition energies between the doped and host materials.

3.2.4 Electrochemical Tests

Electrochemical measurements of $Na_{3+x}V_{2-x}Mg_x(PO_4)_3$/C ($x$ = 0, 0.05, and 0.1) samples were carried out using CR2016 coin cells. Na metal was used as the counter electrode. The electrodes were made by mixing the active material, carbon black, and poly(vinylidene fluoride) in an 8:1:1 ratio. Then the electrodes were dried at 100 °C for 10 h. Afterward, 10 mm diameter circular disk electrodes were cut to form the electrode. The mass loading of the active material on the electrode was about 4.0 mg cm^{-2}. The cells were cycled in 1 M NaPF6 in PC while using glass fiber (Whatman GF/F) as the separator. Galvanostatic experiments were carried out using an Arbin BT2000 battery testing system. The voltage range was maintained between 2.5 and 4.0 V. Before the galvanostatic charging/discharging tests, the batteries underwent an aging process for over 2 h to make sure $Na_{3+x}V_{2-x}Mg_x(PO_4)_3$/C ($x$ = 0, 0.05, and 0.1) was fully soaked by the electrolyte.

3.3 Results and Discussion

All synthesized samples $Na_{3+x}V_{2-x}Mg_x(PO_4)_{3/}C$ (x = 0, 0.05, and 0.1) were found to crystallize in the NASICON structure ($R\bar{3}c$ space group, rhombohedral unit with 2 Na in 18e position and 1 Na in 6b position). The XRD patterns are shown in Figure 3.1 and the Rietveld analysis of the sample with x = 0 and 0.05 are reproduced in Figure 3.2. The refinement was done by the FullProf program. [62, 68] Figure 3.2 shows that the calculated pattern matches well with the observed pattern. The structural parameters of $Na_3V_2(PO_4)_3$/C and $Na_{3.05}V_{1.95}Mg_{0.05}(PO_4)_3$/C phases as determined from the Rietveld refinement are illustrated in Table 3.1. The reasonably small R factors show that a single phase was obtained and no impurity phases were detected at

the resolution of our X-ray diffractometer.

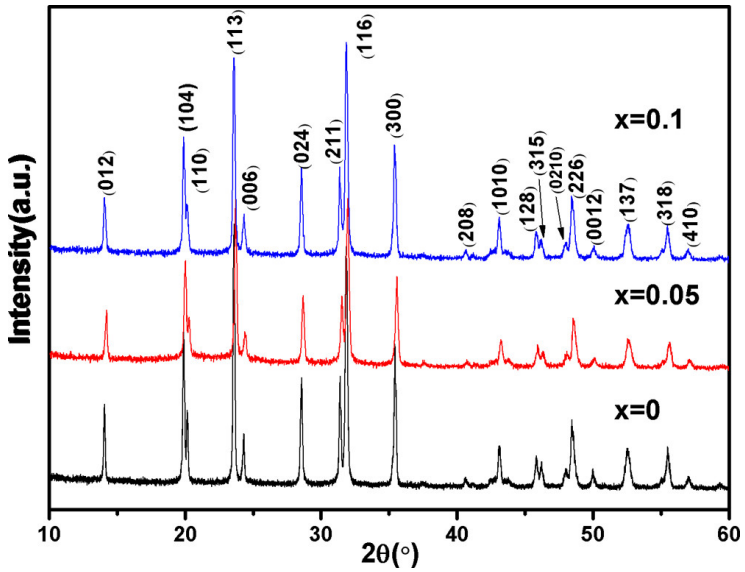

Figure 3.1: XRD patterns of $Na_{3+x}V_{2-x}Mg_x(PO_4)_3$/C ($x$ = 0, 0.05, and 0.1)

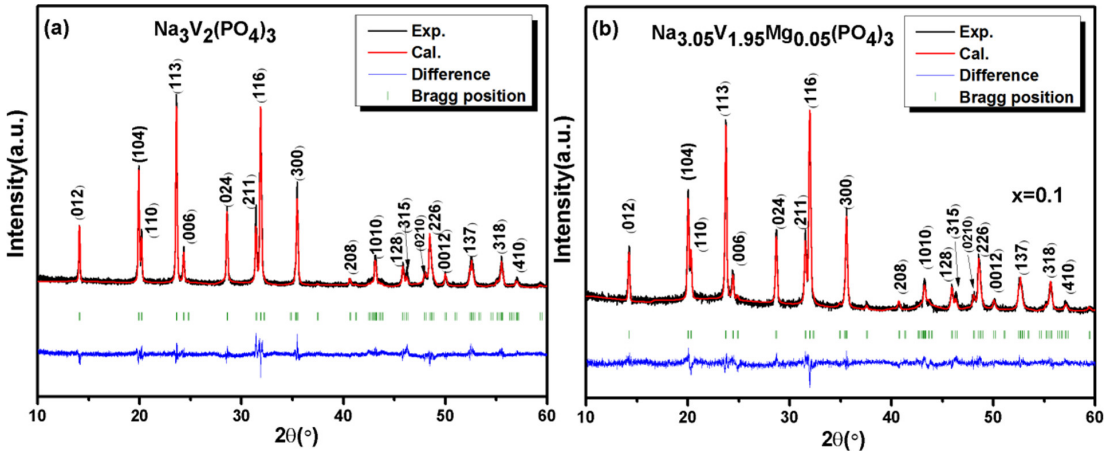

Figure 3.2: XRD Rietveld refinement results of (a) $Na_3V_2(PO_4)_3$/C and (b) $Na_{3.05}V_{1.95}Mg_{0.05}(PO_4)_3$/C.

To confirm that Mg^{2+} doping can improve the $Na_3V_2(PO_4)_3$ performance, electrochemical measurements of $Na_{3+x}V_{2-x}Mg_x(PO_4)_3$/C ($x$ = 0, 0.05, and 0.1) samples were carried out, as shown in Figure 3.3. The cycle performance at 1 and 10 C are displayed in parts (a) and (b), respectively, of Figure 3.3. It is clear that Mg^{2+}-doped samples present superior cycle

Table 3.1: Structural Parameters of $Na_3V_2(PO_4)_3$/C (pristine) and $Na_{3.05}V_{1.95}Mg_{0.05}(PO_4)_3$/C (doped) determined from XRD Rietveld Refinement

	a (Å)	c (Å)	V (Å^3)	R_p (%)	R_{wp} (%)	R_b (%)	Na1	Na2	V	Mg
pristine	8.72	21.83	1438.00	4.69	6.26	9.29	0.98	2.06	1.95	0.05
doped	8.72	21.80	1436.37	5.34	6.91	6.47	1.00	2.00	2.08	0.00

performance at both 1 and 10 C. When cycled at 1 C, all the samples deliver similar initial specific capacity; however, after 180 cycles the capacity of $Na_{3.05}V_{1.95}Mg_{0.05}(PO_4)_3$/C is almost 10 $mAh \cdot g^{-1}$ higher than that of $Na_3V_2(PO_4)_3$/C. When cycled at 10 C, the difference in electrochemical performance between undoped sample and Mg^{2+}-doped sample are more evident. For $Na_{3.05}V_{1.95}Mg_{0.05}(PO_4)_3$/C, the initial capacity is 96.7 $mAh \cdot g^{-1}$, and it has a capacity retention of 88.9% after 180 cycles. However, the undoped $Na_3V_2(PO_4)_3$/C can deliver only 88.8 and 63 $mAh \cdot g^{-1}$ at the first cycle and after 180 cycles, respectively.

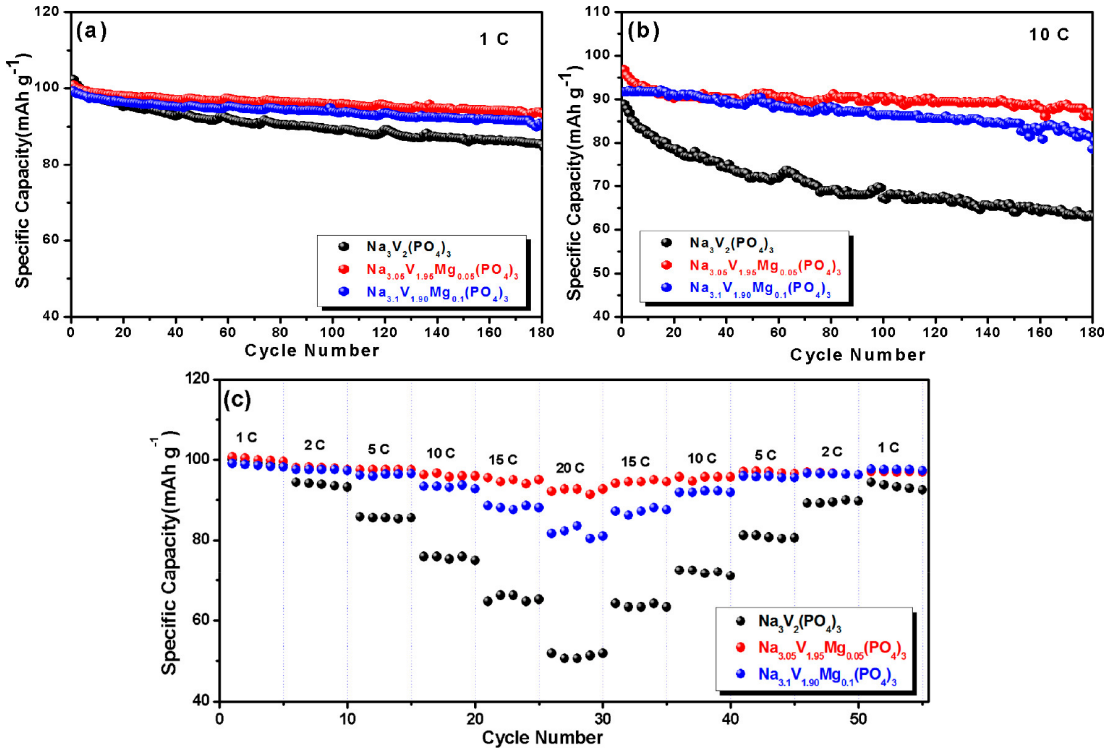

Figure 3.3: Electrochemical performance of $Na_{3+x}V_{2-x}Mg_x(PO_4)_3$/C ($x$ = 0, 0.05, and 0.1): (a) cycle performance at 1 C, (b) cycle performance at 10 C, and (c) rate performance.

The rate performance is shown in Figure 3.3c. It is obvious that the rate ability of Mg^{2+}-doped $Na_3V_2(PO_4)_3$/C is better than that of the undoped sample. $Na_{3.05}V_{1.95}Mg_{0.05}(PO_4)_3$/C delivers 95.5 and 92.1 $mAh \cdot g^{-1}$ at 15 and 20 C, respectively, whereas $Na_3V_2(PO_4)_3$/C delivers only 64.7 and 50.6 $mAh \cdot g^{-1}$ at the same rates. The above results demonstrate that doping can improve the electrochemical performance. In addition, it is found that the higher the rate, the greater the difference in the electrochemical performance between the Mg^{2+}-doped sample and the undoped sample.

The reason for the enhanced electrochemical performance of the doped samples is explored. According to previous reports, [75, 76] there are Na site and V site for $Na_3V_2(PO_4)_3$ to substitute. There are also two Na sites for $Na_3V_2(PO_4)_3$ and the crystal structure is displayed in Figure S1 of the Supporting Information. Na(1) site has sixfold coordination situated between two adjacent $V_2(PO_4)_3$ units along the z axis. Na(2) site has eightfold coordination located at the same z value as the phosphorus atoms between two PO4 tetrahedra. For each formula, there are three positions for Na(2) and one position for Na(1). The sodium ions at the Na(2) site are electrochemically active when $Na_3V_2(PO_4)_3$ is used as cathode of SIBs. For $Na_3V_2(PO_4)_3$, two of the three sodium ions are in the Na(2) site and the remaining sodium ions are located in the Na(1) site. Because of the different valences among Mg^{2+}, V^{3+}, and Na^+, the molar ratio of V^{3+} and Na^+ is changed to keep the charge balance when Mg^{2+} migrates to a different site. Because of the complexity of the crystal structure and the valence of the elements, identifying the doping site is vital to understand how the dopant influences the electrochemical properties. Three mechanisms of Mg^{2+}-doped $Na_3V_2(PO_4)_3$ are studied and illustrated in Table 3.2. The detailed crystal structure corresponding to the different mechanisms is shown in Figure 3.4. In Figure 3.4a, one Na^+ in the Na(2) site disappears when a Mg^{2+} replaces one Na^+ because of the lower valence of Na^+ compared to that of Mg^{2+}. As a result, the electrochemically active Na decreases as Mg^{2+} increases and moves to the Na site. In mechanism 2, charge compensation is achieved by a V^{3+} becoming V^{4+}, which reduces the available redox couples for storage. Finally,

in mechanism 3, an additional Na^+ is introduced to the Na(2) site (Figure 3.4 c) when Mg^{2+} is doped into the V site and V^{3+} does not change the valence; hence, more electrochemical Na^+ is inserted into the crystal. To determine which mechanism happens in this work, several methods are used and discussed below.

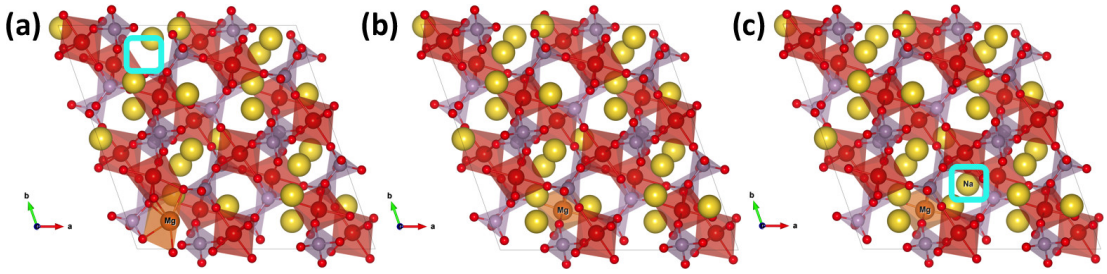

Figure 3.4: Crystal structure of $Na_3V_2(PO_4)_3$ by first-principles calculation: (a) when Mg^{2+} goes to the Na site, (b) when Mg^{2+} goes to the V site and V3+ changes the valence to keep charge balance, and (c) when Mg^{2+} goes to the V site and more Na^+ are introduced to keep the charge balance.

Table 3.2: Mechanisms of Mg^{2+}-Doped $Na_3V_2(PO_4)_3$.

	Mechanism 1	Mechanism 2	Mechanism 3
doping site	Na site	V site (V valence changes)	V site (Na is introduced)
compound	$Na_{3-2x}V_2Mg_x(PO_4)_3$	$Na_3V_{2-x}Mg_x(PO_4)_3$	$Na_{3+x}V_{2-x}Mg_x(PO_4)_3$

Li et al. [77] proposed an effective way to explore the preferred doping site in polyanion materials. Their formula is shown as follow:

$$D_{M1(2)} = |(X_M - X_{M1(2)})/X_{M1(2)}| + |(r_M - r_{M1(2)})/r_{M1(2)}| \tag{3.2}$$

where X_M and $X_{M1(2)}$ are electronegativity values of the dopant and the substituted ion and r_M and $r_{M1(2)}$ are the ionic radius of the dopant and the substituted ion. If $D_{\mathrm{M1}} < D_{\mathrm{M2}}$, the dopant tends to go to the M1 site, while if $D_{\mathrm{M1}} > D_{\mathrm{M2}}$, the dopant prefers to occupy the M2 site. According to the above formula, the values for Mg^{2+}-doped $Na_3V_2(PO_4)_3$/C are $D_{\mathrm{V}} = 0.3228$

and D_{Na} = 0.521. Mg^{2+} goes to the V site for Mg^{2+}-doped $Na_3V_2(PO_4)_3$/C since D_{Na} is greater than D_V.

The doping site was studied by first-principles calculations. Table 3.3 shows the phase stability represented by E_{hull} with respect to the different Mg^{2+} doping mechanism. Mechanism 3 is most probable as shown in Table 3.3. Mg^{2+} is inclined to go to the V site, which is consistent with the above empirical formula. It can be concluded that more Na^+ is introduced to the crystal structure to keep the charge balance.

Table 3.3: E_{hull} (meV/atom) and E_f (meV/f.u.) for Different Doping Sites of Mg^{2+} in $Na_3V_2(PO_4)_3$

	$Na_{3-2x}V_2Mg_x(PO_4)_3$		$Na_3V_{2-x}Mg_x(PO_4)_3$		$Na_{3+x}V_{2-x}Mg_x(PO_4)_3$	
	E_{hull}	E_f	E_{hull}	E_f	E_{hull}	E_f
$x = 0.0625$	0	0	1.92	613.86	0	0
$x = 0.125$	1.51	239.59	3.14	502.36	0.47	75.46
$x = 0.25$	4.63	365.89	4.45	356.17	0.21	16.66
$x = 0.5$	10.74	418.93	4.77	190.61	0	0

On the basis of the above results, first-principles calculations were carried out only under mechanism 3 to find potential doping species and the preferred doping concentration among divalent ions [Ni^{2+}, Mg^{2+}, Cu^{2+}, Cr^{2+}, Zn^{2+}, Pd^{2+}, Ag^{2+}, Ca^{2+}, Sr^{2+}, and Ba^{2+}]. The chemical stability and doping concentration (x = 0.0625, 0.125, 0.25, and 0.5) relationship for both mechanisms are shown in Figure 3.5, which indicates that the phase stability decreases as dopant concentrates. However, Mg^{2+}-doped chemistries remain relatively stable within the tested dopant concentrations. This observed stability may be due to the similar ionic radius of Mg^{2+} (86 pm) and V^{3+} (78 pm), which alleviates the structural distortion from doping.

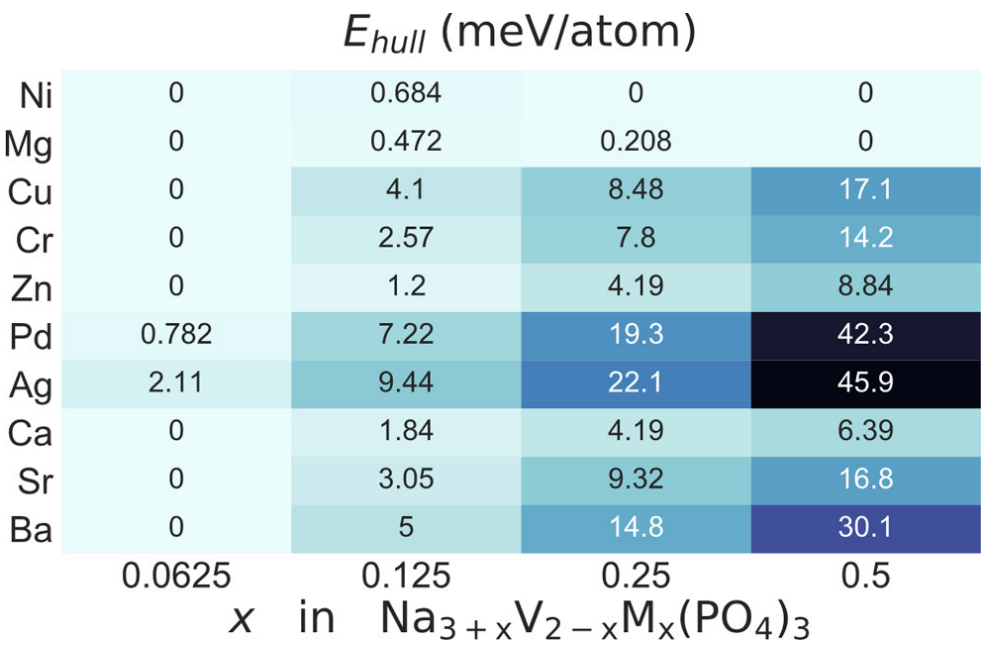

Figure 3.5: Chemical stability (E_{hull}) of substitutional divalent dopants in $Na_3V_2(PO_4)_3$. To maintain charge balance after substitution on V sites, extra sodium ions are introduced.

All the theoretical results above show that Mg^{2+} prefers to go to the V site and the doping site was proved by an experimental method. Because of the different valence numbers between Mg^{2+}, V^{3+}, and Na^{+}, the molar ratio of V and Na is changed to keep the charge balance when Mg^{2+} goes to the different sites as discussed above. The comparison of the Na/V ratio trend for different doping sites is displayed in Figure 3.6. It is found that the Na/V trend from ICP is consistent with the Na/V ratio of theoretical value (Mg^{2+} is doped on V site). The experimental results demonstrate that Mg^{2+} goes to the V site and more Na^{+} is introduced to $Na_3V_2(PO_4)_3$ crystal structure to keep the charge balance. Hence, Mg^{2+}-doped $Na_3V_2(PO_4)_3$/C shows better electrochemical performance because inserting excess Na^{+} is electrochemically active during the charging/discharging process.

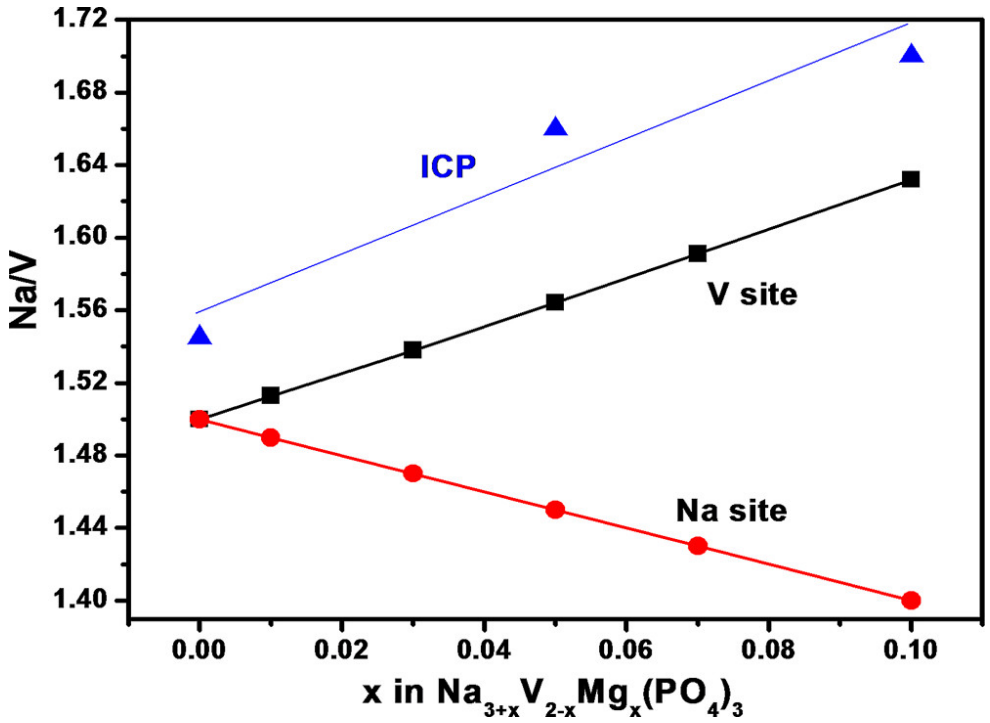

Figure 3.6: Na/V ratio for Mg^{2+}-doped $Na_3V_2(PO_4)_3$/C when doped at different sites and Na/V ratio for the ICP results.

To explain the reason for the enhanced electrochemical performance at high rates for Mg^{2+}-doped $Na_3V_2(PO_4)_3$/C, the crystal structure and kinetic properties were investigated in detail. The unit cell volumes of $Na_{3+x}V_{2-x}Mg_x(PO_4)_3$ from first-principles calculation are provided in Table 3.4. When *x* increases from 0 to 0.0625, the volume increases from 1438.74 to 1499.52, that is, by 4%. However, the XRD refinement results show a volume increase from 1436.374 to 1438.004 when *x* increases from 0 to 0.05, which is only about 0.1% of the volume change. It is worth noting that the model from calculation is built based on the uniform distribution of Mg^{2+}. From the noticeable difference of volume changes between first-principles calculation and XRD Rietveld refinement, it can be inferred that Mg^{2+} is not evenly distributed in the bulk.

To verify this assumption, the internal resistance of sodium half cell assembled with $Na_3V_2(PO_4)_3$/C and $Na_{3.05}V_{1.95}Mg_{0.05}(PO_4)_3$/C were evaluated. The Nyquist plots are shown in Figure 3.7. In the Nyquist plots, each impedance spectrum consists of a depressed semicircle at

Table 3.4: Volume of $Na_{3+x}V_{2-x}Mg_x(PO_4)_3$ from First-Principles Calculations

Sample	$x = 0$	$x = 0.0625$	$x = 0.125$	$x = 0.25$
V	1438.74	1499.52	1502.19	1504.62

high frequency and a slope line in the low-frequency range. The high-frequency region of the semicircle is attributed to interfacial resistance between the electrode and the electrolyte (ion migration through the surface layer and the charge-transfer reaction through the electrode–electrolyte interphase), while the slope line is due to Warburg impedance, which originates from the diffusion of sodium ions into the bulk of the electrode material. [78, 79, 80] In Figure 3.7a, the semicircle is hardly changed at different temperatures in $Na_3V_2(PO_4)_3$/C; however, when Mg^{2+} is doped into $Na_3V_2(PO_4)_3$, the interfacial resistance decreases as the temperature increases, shown in Figure 3.7b. It can be concluded that Mg^{2+} doping has a significant impact on the interface of $Na_3V_2(PO_4)_3$/C. Furthermore, the sodium ion diffusion coefficient (DNa^+) in the bulk of the particles was calculated according to the plots in the low-frequency region and the results are displayed. For the undoped and Mg^{2+}-doped samples, the diffusion coefficient of sodium ion at different temperatures is very similar, which means that Mg^{2+} doping has little influence on the diffusion coefficient of sodium ions in the bulk of the particle. Combined with the results of crystal volume change, interfacial resistance changes, and ion diffusion in the bulk, Mg^{2+} is mainly distributed on the surface of particles as illustrated in Figure 3.8.

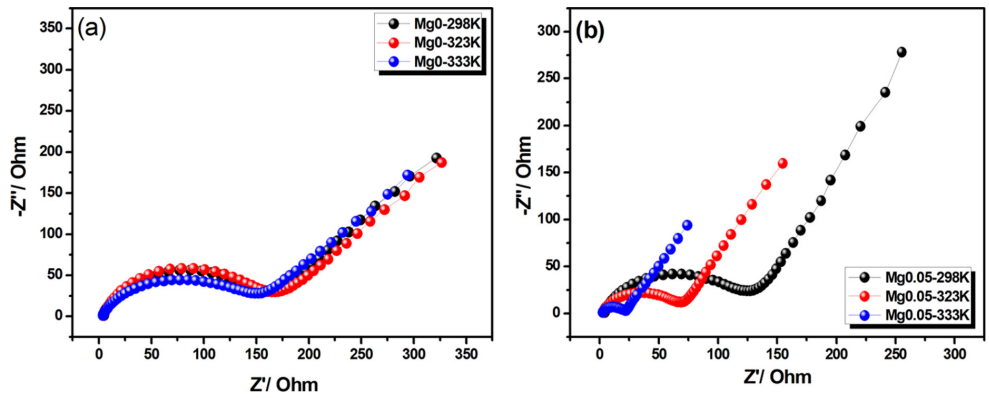

Figure 3.7: Nyquist plots of (a) $Na_3V_2(PO_4)_3$/C and (b) $Na_{3.05}V_{1.95}Mg_{0.05}(PO_4)_3$/C at 298 K (black), 323 K (red), and 333 K (blue).

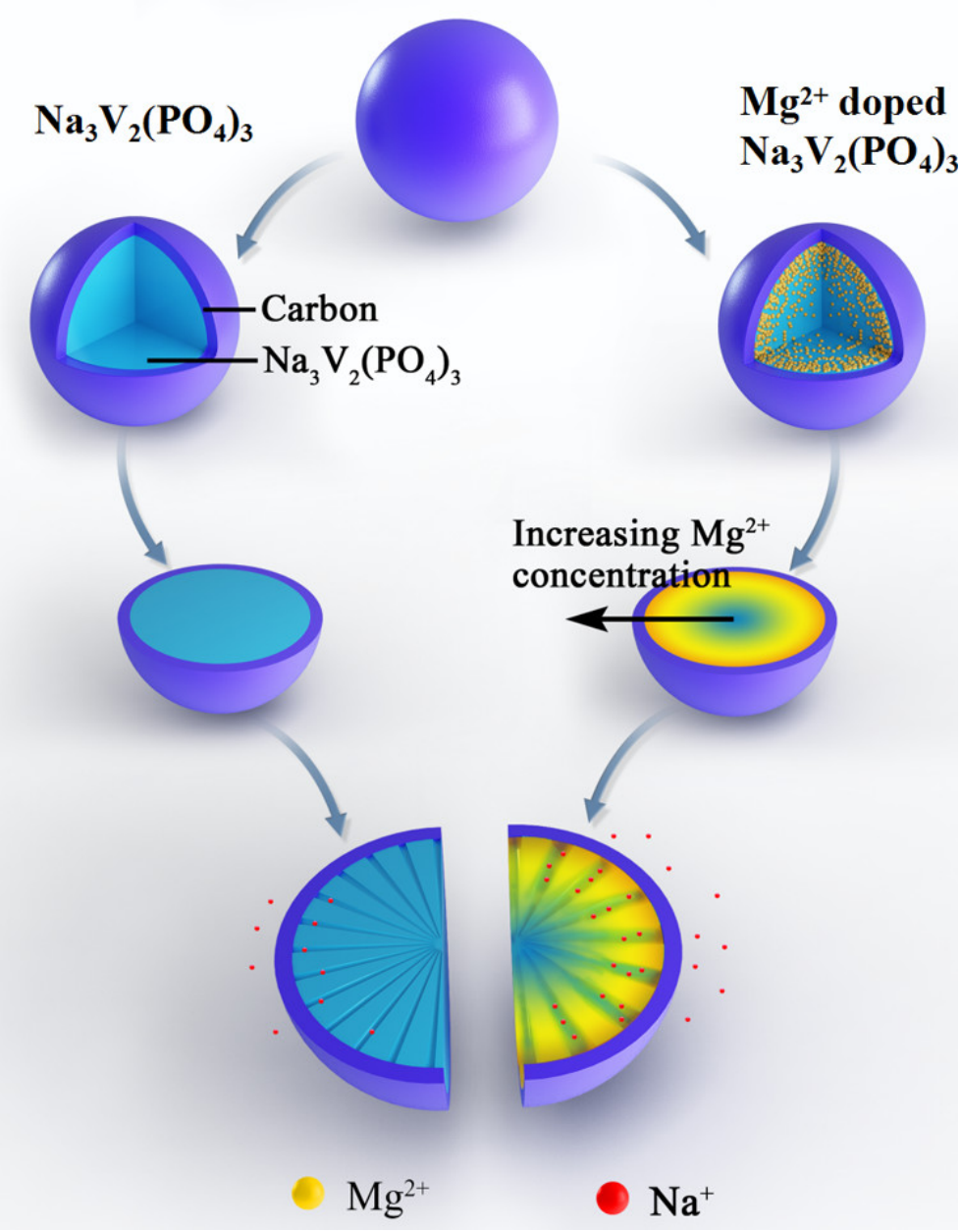

Figure 3.8: Schematic illustration of sodium ion diffusion channel in undoped and Mg^{2+}-doped $Na_3V_2(PO_4)_3$/C.

It is well-known that cation doping improves the electrochemical performance mainly because of the structural stability and enhanced ionic and electronic conductivity induced by the doped ion. [60, 80, 81] However, the enhanced electrochemical performance is also related to the doped ion distribution. Nonuniform distribution of Mg^{2+} may lead to stratification of

$Na_3V_2(PO_4)_3$ particles. As shown in Figure 3.8, most of the Mg^{2+} are distributed on the particle surface layer and less Mg^{2+} are disseminated in the bulk of $Na_3V_2(PO_4)_3$ particle. This is further demonstrated in the Supporting Information. According to previous reports, cation doping can enlarge the Na ion diffusion pathway. [68] Hence, nonuniform distribution of Mg^{2+} doping brings out faster Na^+ diffusion on the surface than that in the bulk of the particle. At the same time, shown in the SEM image of $Na_3V_2(PO_4)_3$/C, the microscale particle size hinders the electrochemical performance with the long ionic diffusion distance. [82] When batteries are cycled at high rates, it is hard for Na^+ to go into the bulk of $Na_3V_2(PO_4)_3$/C particle because of the short time for such a long ionic diffusion distance. As a result, the electrochemical reaction occurs mainly on the surface of the particle. The surface property of active material is vital for electrochemical reaction since effective charge carriers must successfully diffuse to the surface and undergo interfacial charge transfer. [83] Therefore, the modified surface property for Mg^{2+}-doped samples leads to the superior electrochemical performance compared to that of the undoped sample.

3.4 Conclusion

In summary, a series of Na-rich $Na_{3+x}V_{2-x}Mg_x(PO_4)_3$/C ($x$ = 0, 0.05, and 0.1) cathode materials were synthesized by the sol–gel method. All doped samples display improved electrochemical performance, especially at high rates. To probe how Mg^{2+} doping affects the electrochemical performance of $Na_3V_2(PO_4)_3$/C, the doping site was explored by empirical formula, first-principles calculation, and ICP. The results indicate that Mg^{2+} prefers to go to the V site and extra Na^+ is introduced to $Na_3V_2(PO_4)_3$/C crystal to keep the charge balance. Because the extra Na^+ is located in the Na(2) site, it not only increases the electrochemically active Na^+ content but also stabilizes the crystal structure. In addition, the distribution of Mg^{2+} in the $Na_3V_2(PO_4)_3$/C particle also influences the electrochemical performance. Combined with the results of the crystal volume shifts, interfacial resistance changes, and ion diffusion in the bulk, it can be concluded

that Mg^{2+} distributes on the surface of $Na_3V_2(PO_4)_3$/C particle. This will facilitate the surface reaction during charging/discharging, leading to excellent rate performance of the material.

3.5 Acknowledgement

Chapter 3, in full, is a reprint of the material "Understanding the Electrochemical Mechanisms Induced by Gradient Mg^{2+} Distribution of Na-Rich $Na_{3+x}V_{2-x}Mg_x(PO_4)_3$/C for Sodium Ion Batteries" as it appears in Chemistry of Materials, Hui Li, Hanmei Tang, Chuze Ma, Ying Bai, Judith Alvarado, Balachandran Radhakrishnan, Shyue Ping Ong, Feng Wu, Ying Shirley Meng, and Chuan Wu, 2018 Apr 3;30(8):2498-505. All simulations and corresponding data analysis were performed by the dissertation author.

Chapter 4

Probing Solid-Solid Interfacial Reactions in All-Solid-State Sodium-Ion Batteries with First-Principles Calculations

4.1 Introduction

All-solid-state rechargeable alkali-ion batteries (SSABs) have garnered significant interest in recent years.[84] By replacing flammable organic solvent electrolytes with non-flammable solid electrolytes, SSABs promises to be a safer energy storage architecture, while at the same time, potentially provide significant gains in system-level energy densities through device optimization (e.g., stacking) or enabling new chemistries (e.g., high-voltage cathodes and alkali metal anodes).[5, 85]

Despite ground-breaking discoveries of novel solid electrolyte (SE) chemistries exhibiting superionic alkali conductivities,[86, 87, 88, 89, 90, 91] a major challenge that remains is the unsatisfactory rate performance and cycling stability of SSABs due to the high resistance and poor stability of electrode/SE interface. For example, though the $Li_{9.54}Si_{1.74}P_{1.44}S_{11.7}Cl_{0.3}$ based

on the $Li_{10}GeP_2S_{12}$ (LGPS) structure first reported by Kato et. al. [92] has one of the highest Li^+ conductivities (25 mS/cm), its extremely poor electrochemical stability and interfacial side reactions render it far less practical than $Li_{9.6}P_3S_{12}$, a material reported in the same work with a significantly lower conductivity (1.2 mS/cm) but much better interfacial stability. For Na-ion chemistry, most reported room-temperature solid-state Na batteries reported thus far suffer from limited capacity or significant capacity degradation during cycling. [91, 93, 94, 95, 13, 96, 97]

It is therefore not surprising that researchers have escalated their efforts at understanding and addressing these interfacial issues in SSABs. On the experimental front, X-ray photoelectron spectroscopy (XPS) has emerged as a common approach to probe and identify the species present at the buried electrode/SE interface.[16, 98, 18] The application of buffer layers such as Al_2O_3 has been demonstrated to be an effective approach in improving the wetting of the electrode/SE interface (especially for Li metal anodes),[99] as well as a protective barrier to electrode/SE reactions (especially for sulfide SEs).[100, 101, 102] Also, first principles calculations have emerged as an important complementary tool to precisely probe interfacial reactions[103, 104] and the electrochemical stability of SEs. Ong, Mo and Ceder[14, 15] first developed the first principles Li grand potential approximation to predict the SE phase equilibria at the high and low voltage limits in the LGPS family of SEs. This approximation has been shown to be remarkably effective, as evidenced by subsequent experimental confirmation of the predicted reaction phases via XPS measurements.[16] Later, these approaches were further extended to extensive studies of most well-known Li and Na SEs [10, 17, 9, 33, 34, 13]. More recently, Tian et al. reported a combined experimental and theoretical study of the compatibility of the Na_3PS_4 and Na_3PSe_4 SEs with layered transition metal oxide ($NaTmO_2$, Tm = Cr, Mn, Fe, Co, Ni) cathodes.[18]

In this work, we will attempt to address two crucial gaps in previous works. First, previous works have primarily focused on thermodynamic approximations to interfacial phase equilibria; kinetic effects are only accounted for to a limited extent,[18] if at all. Second, a comprehensive assessment of Na-ion electrode/SE interactions have not been performed, and

in general, there is a lack of guidance on effective materials selection strategies for cathode/SE, anode/SE, and buffer layers for all-solid-state Na-ion batteries (SSNaBs). In the subsequent sections, we will first outline the various approximation methodologies for predicting interfacial phase equilibria, including explicit kinetic interface model analysis using *ab initio* molecular dynamics (AIMD) combined with radial distribution function analysis. This is followed by a comprehensive study of the reactions between the common cathode, anode and SE chemistries currently under consideration for SSNaBs, along with recommended materials selection strategies. Furthermore, we will also attempt to provide a rough estimate of the chemo-mechanical effect of these reactions, a factor not considered in previous works.

4.2 Methods

4.2.1 Materials Selection

The relatively low computational cost of the thermodynamic approaches 1 and 2 above permit a high-throughput analysis of a large number of material combinations forming the interface, especially if pre-computed energies and volumes from MP database are used where available. As such, we have performed a comprehensive analysis covering most well-known SE, cathode and anode materials across a broad range of chemistries currently of interest in the Na-ion battery community, as tabulated in Table 4.1.

More details regarding selected structures for thermodynamic interfacial reactivity assessments can be found in Supporting Information.

Given the high computational expense of AIMD simulations of interfacial systems, approach 3 was applied only for one model battery system: layered O3-$NaCoO_2$ cathode, Na_3PS_4 SE and Na metal anode, with Al_2O_3 as the model buffer layer. For the $NaCoO_2$ cathode, both the half-discharged and fully-discharged cathode materials were modeled to assess the effect of

Table 4.1: List of cathodes, solid electrolytes, anodes and buffer layer materials studied using thermodynamic approaches 1 and 2.

Category	Materials
Solid electrolytes	NASICON $Na_3Zr_2Si_2PO_{12}$, Na_3PS_4, Na_3AsS_4, Na_3SbS_4, Na_3PSe_4
Cathodes	Layered $NaMO_2$ (M = Cr, Mn, Fe, Co, Ni), Layered TiS_2, $NaFePO_4$, Na_2FePO_4F, $Na_3V_2(PO_4)_3$, $Na_3V_2(PO_4)_2F_3$, $Na_2Fe_2(SO_4)_3$
Anodes	Na metal, $Na_2Ti_3O_7$
Buffer layers	ZnO, CdO, Al_2O_3, Sc_2O_3, Y_2O_3, La_2O_3, SiO_2, TiO_2, ZrO_2, HfO_2, Nb_2O_5, Ta_2O_5

state of charge on the interfacial reactivity. All structures used to construct interfaces are relaxed structures from MP database, and details are tabulated in Table 4.2.

Table 4.2: Selected structures for interface constructions.

	Cathode	Solid electrolyte	Anode	Buffer layer
Formula	$NaCoO_2$	Na_3PS_4	Na	Al_2O_3
MP id	mp-18921	mp-985584	mp-127	mp-1143
Space group	$R\bar{3}m$	$I\bar{4}3m$	$Im\bar{3}m$	$R\bar{3}c$
Slab orientation	$(10\bar{1}0)$	(001)	(001)	(0001)

4.2.2 DFT Calculation Parameters

All calculations were carried out using the Vienna *Ab initio* Simulation Package (VASP)[69] within the projector augmented wave approach[70] using the Perdew-Burke-Ernzerhof generalized-gradient approximation (GGA) functional.[71]

For total energy calculations, a mixing scheme combining GGA calculations with or without Hubbard (+U) correction was applied to treat electron insulators and conductors properly.[105] All parameters, such as plane wave energy cutoff of 520 eV and k-points density of at least

1000/(number of atoms), were chosen in a consistent manner with those used in MP as implemented in Python Materials Genomics (pymatgen)[27] package. All calculations were spin-polarized starting from a high-spin ferromagnetic configuration, except for Co which is initialized with low spin.

For AIMD simulations, non-spin-polarized were performed using a minimal Γ point k-point grid and a time step of 2 fs. The use of non-spin-polarized calculations is a necessary approximation to ensure the AIMD simulations can be performed at a reasonable cost, and we do not expect the key results (reaction mechanisms and products at the interface) to be significantly affected by this approximation. Simulations in the NpT ensemble at 300 K were first carried out until the volume of the cell is converged to within 2%. This step is necessary to minimize the interfacial stress caused by the lattice misfit, and typically occurs within ˜4 ps of simulation time. The pressure of NpT simulations was kept at 1 atm with the Langevin thermostat [106], and a larger plane-wave energy cutoff of 400 eV (without oxygen) or 600 eV (with oxygen) was used to avoid the undesired Pulay stress error. This is followed by NVT simulations at 300 K using a smaller energy cutoff of 280 eV (without oxygen) or 400 eV (with oxygen) and the Nose-Hoover thermostat. All calculations were carried out using an automated in-house AIMD workflow software.[32]

4.3 Results

4.3.1 Electrochemical (Grand Canonical) Stability

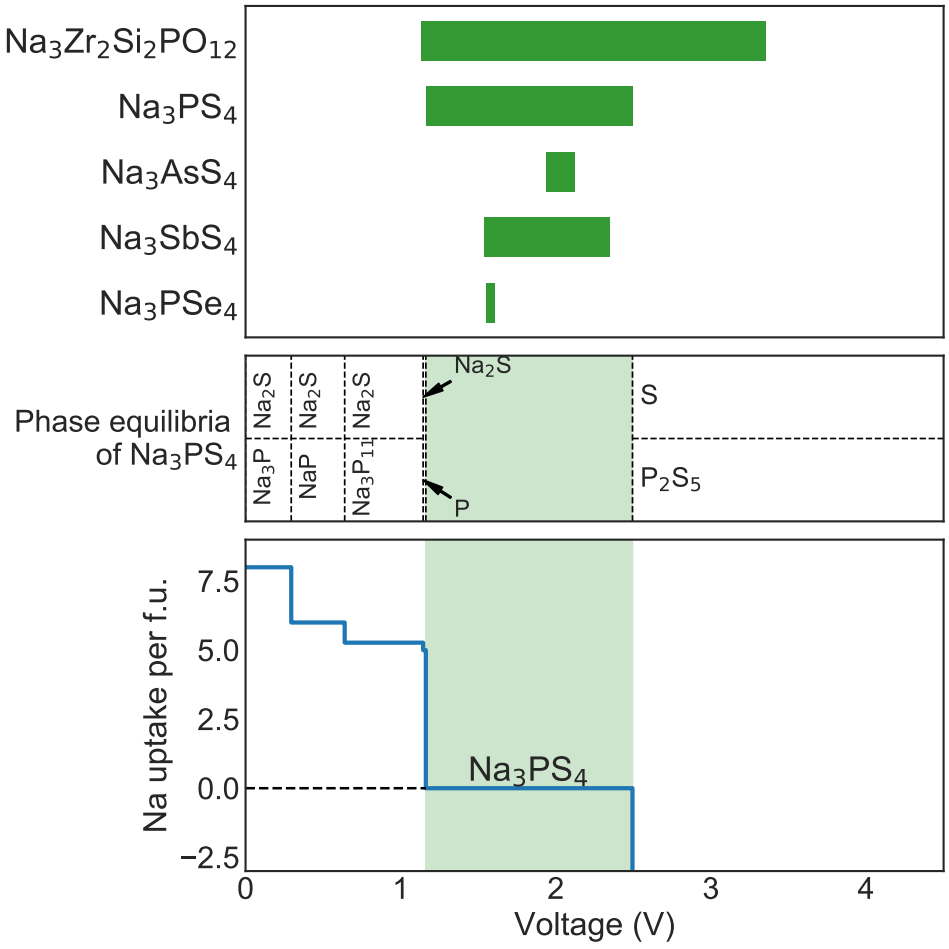

Figure 4.1: (top) Electrochemical stability of studied solid electrolytes. (middle) Predicted phase equilibria at different voltage (μ_{Na}) ranges for one example solid electrolyte - Na_3PS_4. (bottom) Na uptake per formula unit of Na_3PS_4 versus voltage.

Figure 4.1 shows the predicted electrochemical window of various SEs calculated using the grand potential phase diagram approach. We find that none of the commonly studied Na SEs are stable against Na uptake at a voltage close to Na metal. Generally, the NASICON $Na_3Zr_2Si_2PO_{12}$ oxide SE has better cathodic as well as anodic stability compared to the sulfide

SEs, which in turn have better cathodic and anodic stability compared to the selenide (Na_3PSe_4).

Figure 4.1 also shows the predicted phase equilibria and Na uptake versus voltage for the Na_3PS_4 SE. The predicted products at the Na metal anode voltage are Na_3P and Na_2S, in good agreement with XPS measurements of Na_3PS_4 after Na metal deposition.[98] We also note that Na_3AsS_4 and Na_3SbS_4 show significantly narrower electrochemical windows than Na_3PS_4. This is due to the fact that As and Sb are redox-active elements. Interestingly and somewhat counterintuitively, both the immediate cathodic and anodic decomposition of Na_3AsS_4 and Na_3SbS_4 occur with the reduction of As/Sb from the 5+ to the 3+ oxidation state, with the formation of Na_2S with Na uptake (reduction at low voltage) and S with Na extraction (oxidation at high voltage). Details of the reaction products are provided in Supporting Information.

It should be noted that the predicted products for Na_3PS_4 and Na_3PSe_4 differ slightly from those in earlier work by Tian et al. [18] because this study uses only data available in the Materials Project without including predicted phases. Nevertheless, the main qualitative conclusion is the same, which is that both Na_3PS_4 and Na_3PSe_4 have limited electrochemical windows, which are much narrower than those from cyclic voltammetry (CV) measurements.[107]

4.3.2 Chemical (Equilibrium) Stability

Electrode-SE interfacial stability

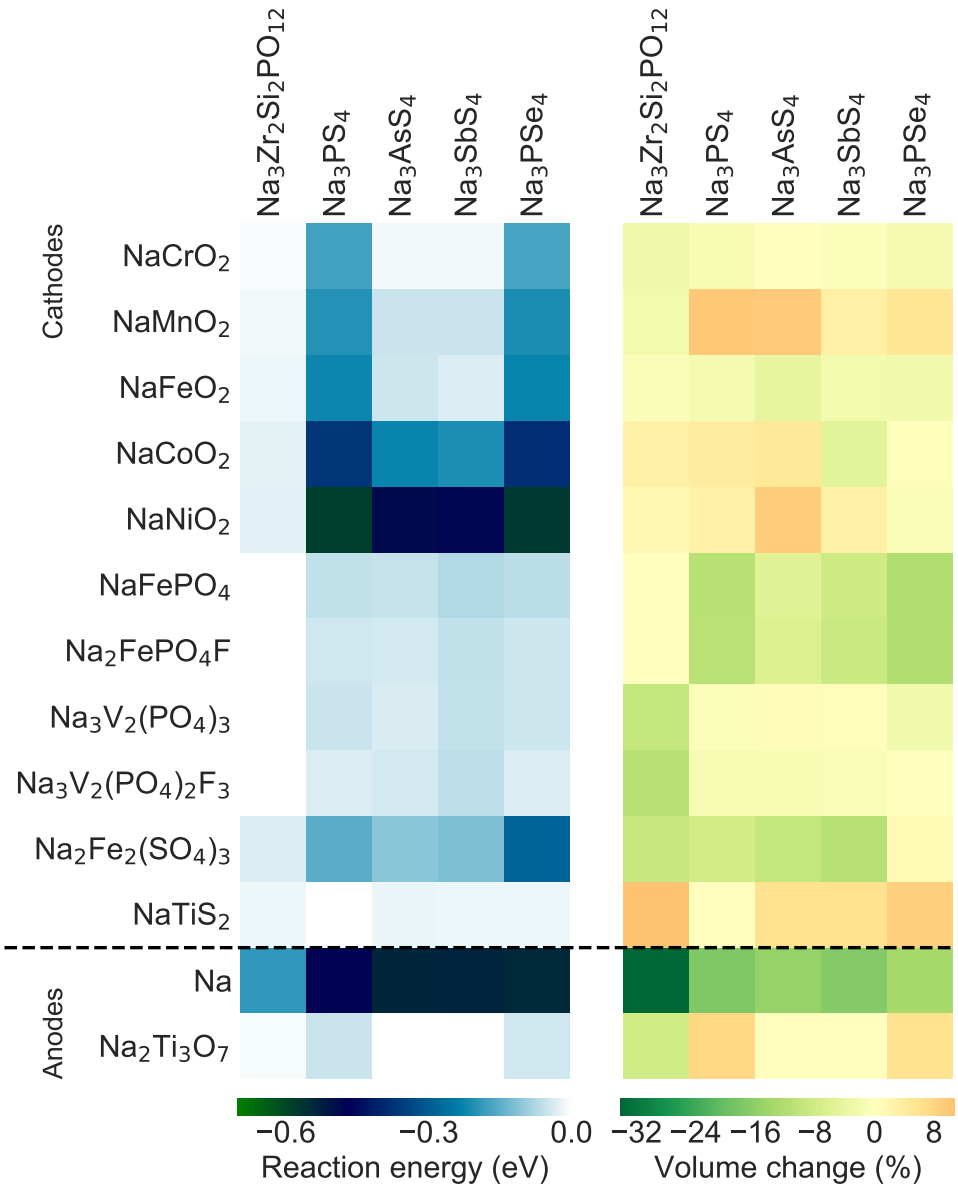

Figure 4.2: Reaction energies (left) and volume changes (right) for electrode-SE pairs. The reactions are calculated for the discharged cathode.

Figure 4.2 shows the calculated reaction energies (left) and volume changes (right) between various discharged electrode-SE pairs using approach 2. We may make the following key observations:

1. Highly unstable cathode/SE combinations arise when a non-polyanion cathode (such as the layered $NaMO_2$ oxides) are paired with Na_3PS_4 or Na_3PSe_4 due to the displacement reaction of the S^{2-} and Se^{2-} by O^{2-} to form the highly stable PO_4 compounds, e.g., $NaCrO_2$ + $Na_3PS(Se)_4 \longrightarrow Na_3PO_4$ + $NaCrS(Se)_2$. This observation is consistent with those made previously [9] and [18]. The volume changes depend on the transition metal species, with $NaCoO_2$, $NaNiO_2$ and $NaMnO_2$ exhibiting relatively large positive volume changes.

2. Substitution of P by As and Sb tends to improve the chemical stability of the layered $NaMO_2$/SE interface. Though the DFT phase diagrams still predict the occurrence of exchange reactions, these tend to be incomplete in the case of As and Sb, i.e., not all As and Sb are consumed in forming As_xO_y or Sb_xO_y polyanions, respectively, which may account for the lower reaction energy compared to P.

3. The PO_4-containing polyanion cathodes – $NaFePO_4$, $NaFePO_4F$, $Na_3V_2(PO_4)_3$, and $Na_3V_2(PO_4)_2F_3$ – show significantly better chemical stability with all sulfide and selenide SEs. However, the two Fe-containing cathodes, $NaFePO_4$ and $NaFePO_4F$, are predicted to exhibit relatively larger negative volume changes upon reactions with sulfide and selenide SEs, while the two V-containing cathodes, $Na_3V_2(PO_4)_3$ and $Na_3V_2(PO_4)_2F_3$, show comparatively smaller volume changes ($|\Delta V| < 2.5\%$) The main reason is the reaction products for the Fe-based cathodes lack low-density chalcogenides (e.g., Na_2S and VS_2). The SO_4-containing $Na_2Fe_2(SO_4)_3$ has a chemical stability in between that of the PO_4-containing and non-polyanion oxide cathodes.

4. Unsurprisingly, the NASICON $Na_3Zr_2Si_2PO_{12}$ shows the best chemical compatibility with

all oxide cathodes among the SEs.

5. The $NaTiS_2$ shows good compatibility with all sulfide and selenide SEs. Somewhat surprisingly, the chemical stability of the NASICON/$NaTiS_2$ interface is predicted to be worse than that of the NASICON/PO_4-containing cathode interface. A NASICON/PO_4-containing cathode interface has either no reaction (e.g., $NaFePO_4$ and Na_2FePO_4F), or non-redox reaction with negligible driving force (e.g., $Na_3V_2(PO_4)_3$ and $Na_3V_2(PO_4)_2F_3$), while NASICON/$NaTiS_2$ interface undergoes a redox reaction with larger driving force.

6. Finally, highly reactive Na metal anode is predicted to be chemically unstable with all SEs, with large negative volume changes. $Na_2Ti_3O_7$ shows much better chemical-mechanical compatibility, with especially low reaction energies and small volume changes with the Na_3AsS_4 and Na_3SbS_4 SEs.

We have performed a similar analysis using a few selected cathodes in the charged state (as opposed to discharged). Generally, charged cathodes are more oxidizing than discharged cathodes, resulting in more negative reaction energies and larger volume changes. Nevertheless, we find that the overall trends in chemical stability across cathode-SE chemistry pairs remain fairly consistent with that of the discharged cathodes.

Evaluation of potential buffer layer materials

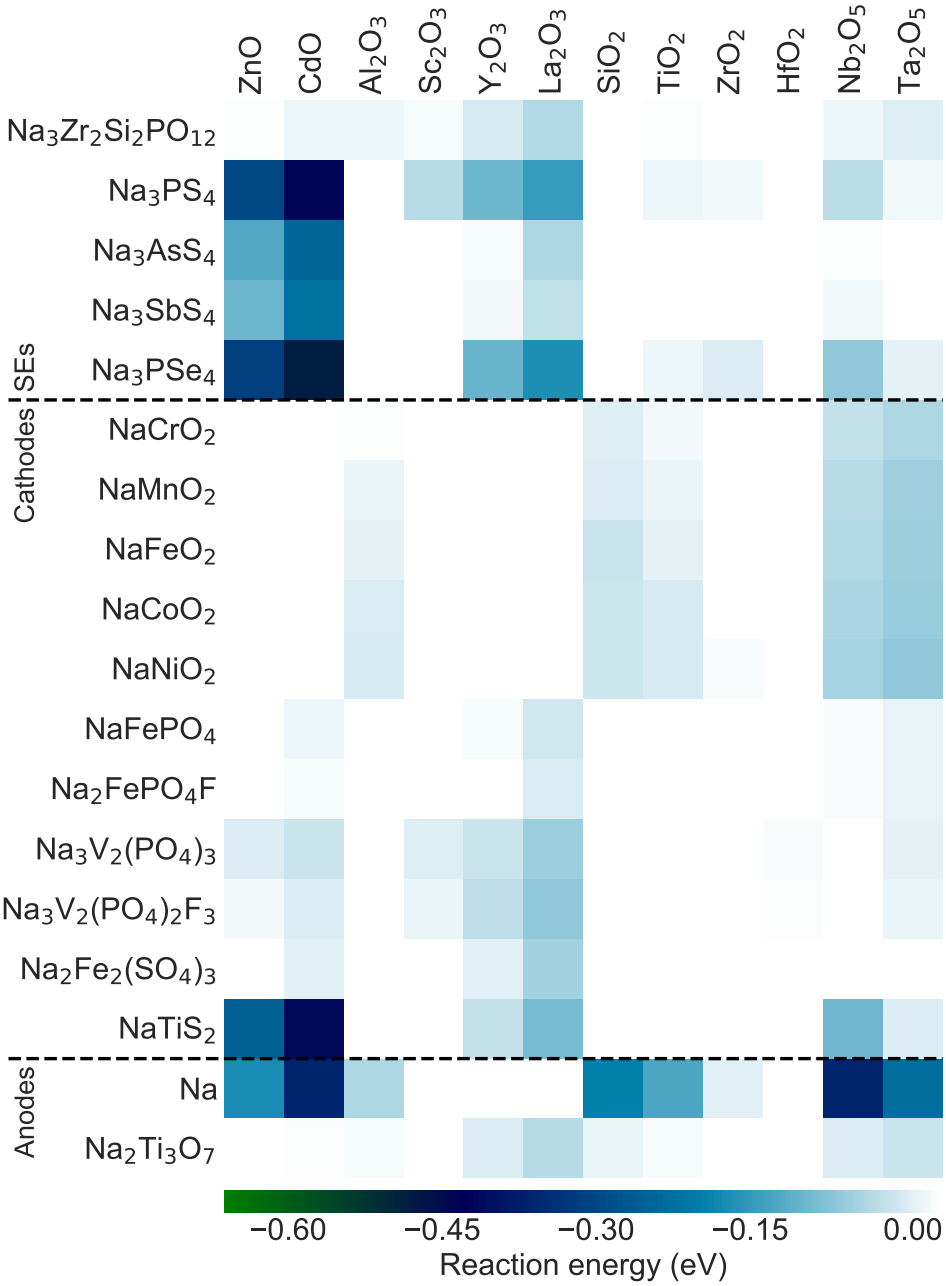

Figure 4.3: Reaction energies between potential buffer layer materials (binary oxides) and various active materials in SSNaBs.

Binary oxides are commonly used as buffer layer materials to protect the electrode/SE interface in alkali-ion batteries.[108, 109] A good buffer layer material should exhibit limited reactivity with both materials at the heterogeneous interface. Figure 4.3 shows the calculated reaction energies of potential buffer layer materials and active materials in SSNaBs. We find that Al_2O_3, a commonly-used buffer layer material,[110] show extremely low reactivity with most SEs and cathodes, and slight reactivity with Na metal. Interestingly, HfO_2 is predicted to be another particularly promising buffer layer material, showing even lower reactivity across nearly all SEs and electrodes compared to Al_2O_3. Indeed, there have been a few attempts to use HfO_2 as protective materials for anodes in alkali-ion batteries.[111, 112] ZrO_2 is another promising candidate as well, though it is predicted to have somewhat higher reactivity with Na_3PSe_4. For the interface between polyanionic cathodes and SEs, SiO_2 is another inexpensive and stable option.

For the Na metal anode/SE interface, only HfO_2, Sc_2O_3 and ZrO_2 are predicted to have low reactivity with Na metal while maintaining low reactivity with the sulfide and selenide SEs.

4.3.3 AIMD Simulations of Explicit Interfacial Models

Due to computational expense, AIMD simulations were carried out on explicit interfacial models for one model system only: layered O3-$NaCoO_2$ cathode, Na_3PS_4 (cubic) SE and Na metal anode, with or without Al_2O_3 as a buffer layer. For the $NaCoO_2$ cathode, both the charged $Na_{0.5}CoO_2$ and fully-discharged $NaCoO_2$ cathode materials were modeled to assess the effect of state of charge on the interfacial reactivity. It should be noted that layered oxides such as $NaCoO_2$ are typically charged only to half theoretical capacity during operation to avoid the collapse of the layered structure; hence, we have used $Na_{0.5}CoO_2$ as the model for the charged cathode. A total of five interfacial models were studied (see Figure 2.4). We will outline the RDF analysis approach in greater detail using the comparatively simpler Na_3PS_4/Na interfacial system to illustrate the key principles, while only key results will be discussed for the other interfacial systems.

Na_3PS_4/Na (SE/anode) interface

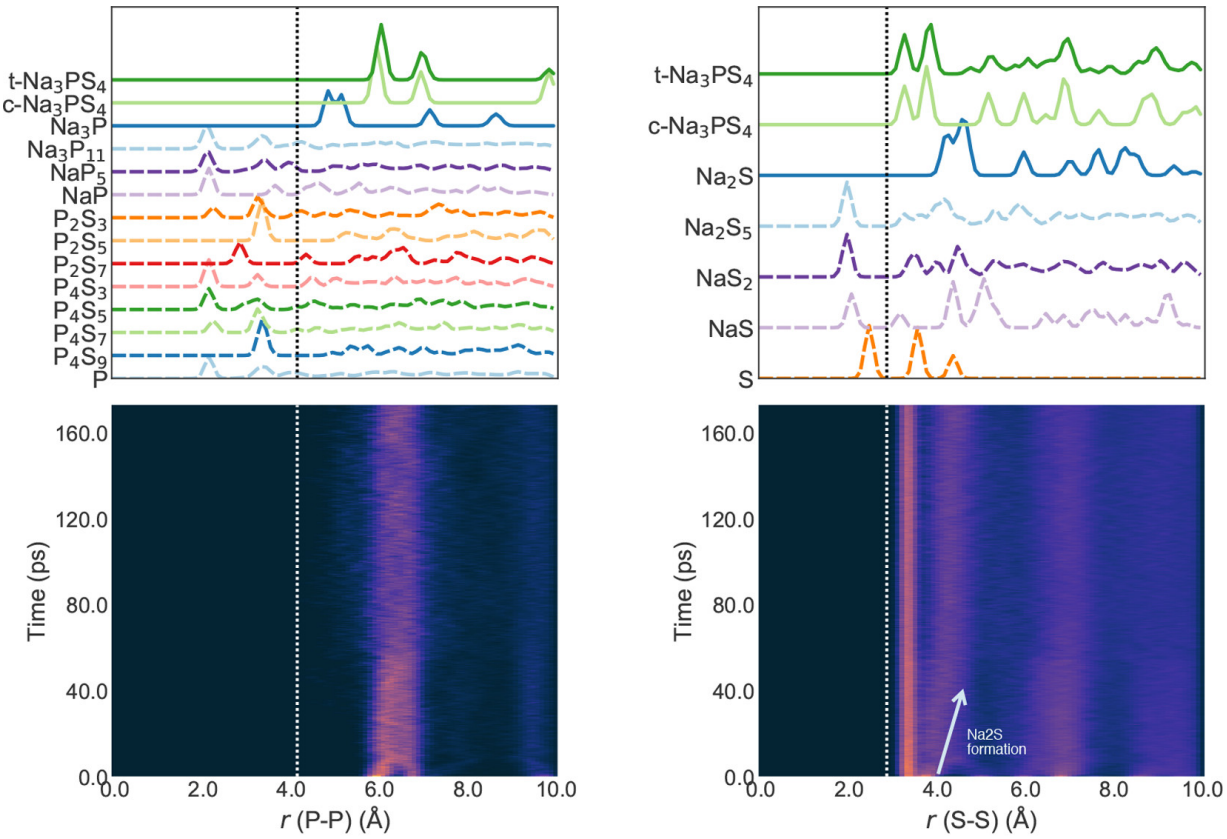

(a) P-P pair (b) S-S pair

Figure 4.4: Evolution of the (a) P-P and (b) S-S RDFs of the Na_3PS_4/Na interface with respect to AIMD simulation time plotted as a heat map, with higher brightness indicating a higher value of *g(r)*, and dashed lines are used to indicate the RDF of phases that are eliminated due to the absence of certain peaks during the AIMD simulations. White arrows and text indicate formation of interfacial reaction phases. The RDF of reference materials are provided above the heat map. Note that t-Na_3PS_4 and c-Na_3PS_4 refer to the tetragonal and cubic phases respectively.

Figure 4.4 shows the evolution of the Na_3PS_4/Na interface model with respect to the simulation time. From Figure 4.4(a), we may observe that there is a negligible density of P-P bonds below 4.2Å throughout the entire simulation, which eliminates P, P_xS_y, NaP, NaP_5 and Na_3P_{11} as potential phases present. From Figure 4.4(b), we similarly observe that there is a negligible density of S-S bonds below 2.9Å, which further eliminates S, NaS_2 and Na_2S_5 as potential phases present at the interface. Through this process of elimination, we conclude that the

potential phases present at the interface are Na_3PS_4, Na_3P and Na_2S. We note that the RDFs in Figure 4.4(a) and 4.4(b) show no presence of peaks corresponding to Na_3P ($\min r(P-P) \sim 5.0$Å) and Na_2S ($\min r(S-S) \sim 4.6$Å), respectively, at the start of the simulation ($t = 0$), but these peaks become progressively stronger over the course of the simulation. We may therefore conclude that the dominant reaction products at the Na_3PS_4/Na interface are Na_2S and Na_3P, which is consistent with the predicted interfacial reaction by thermodynamic approaches and previous experimental studies.[98].

$NaCoO_2$/Na_3PS_4 (cathode/SE) interface

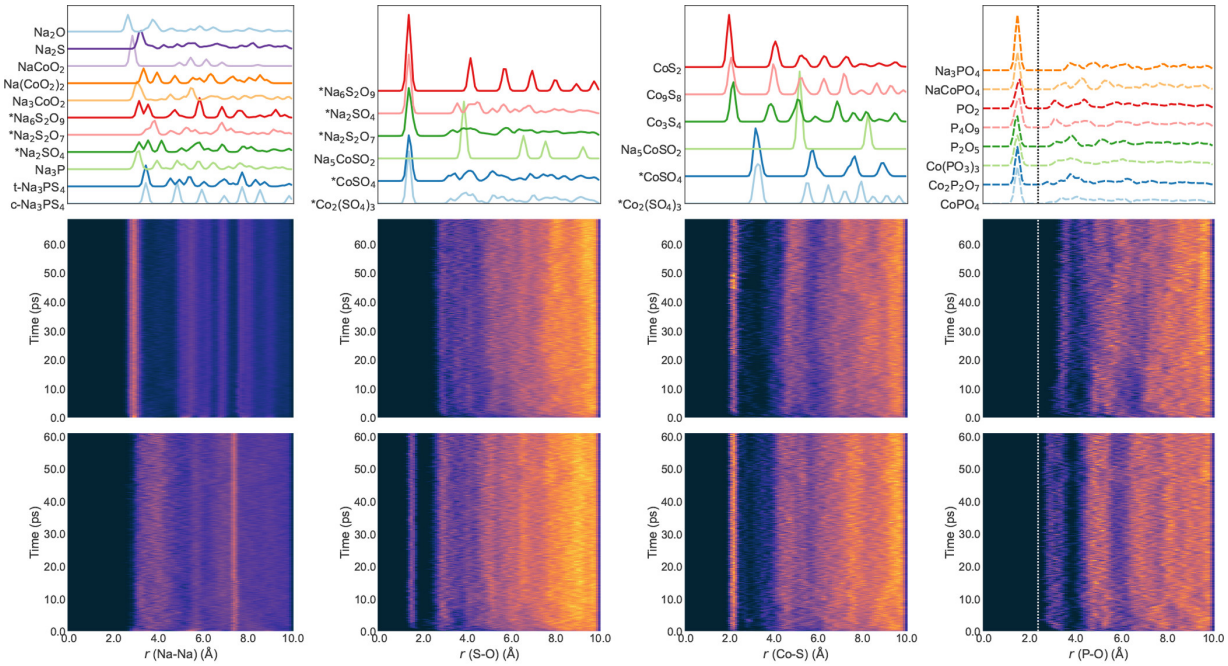

(a) Na-Na pair (b) S-O pair (c) Co-S pair (d) P-O pair

Figure 4.5: Evolution of the (a) Na-Na, (b) S-O, (c) Co-S and (d) P-O RDFs of the cathode/SE interfaces with respect to AIMD simulation time. The middle and bottom heat maps are $NaCoO_2$/Na_3PS_4 and $Na_{0.5}CoO_2$/Na_3PS_4 interfaces respectively. Note that the references labeled with an asterisk are belong to the charged $Na_{0.5}CoO_2$/Na_3PS_4 interface only, and that only some references for the Na-Na and P-O pairs are shown for clarity.

Figure 4.5 shows comparisons between the evolution of interface models with the discharged $NaCoO_2$ and charged $Na_{0.5}CoO_2$ cathode with respect to the simulation time. Unsurpris-

ingly, we observe that the discharged cathode is much less reactive with the Na_3PS_4 SE than the more oxidizing charged cathode. For instance, strong Na-Na peaks corresponding to $NaCoO_2$ persist throughout the entire length of the simulation (Figure 4.5(a)). We will henceforth focus our discussion on the charged $Na_{0.5}CoO_2/Na_3PS_4$ interface.

From Figure 4.5(b), we find that well-defined S-O peaks corresponding to the formation of ${SO_4}^{2-}$ groups ($r_{S-O} \sim 1.5$ Å) become progressively stronger in the $Na_{0.5}CoO_2/Na_3PS_4$ interface after 1 ps. We also observe in Figure 4.5(c) that clear Co-S peaks (~ 2.2 Å) corresponding to Co_xS_y compounds. Finally, based on the P-containing RDFs (Co-P, Na-P, P-S, P-O, P-P), we may conclude that Na_3P is the only other phase present at the interface. Indeed, no P-O signatures corresponding to ${PO_4}^{3-}$ groups ($r_{P-O} \sim 1.5$ Å) are observed (Figure 4.5(d)). This result disagrees with the predicted reaction products for the $NaCoO_2/Na_3PS_4$ and CoO_2/Na_3PS_4 interfaces from the thermodynamic approximations, which include Na_3PO_4 and/or $NaCoPO_4$.

From the above findings, we may infer that the initial interface reaction favors the formation of ${SO_4}^{2-}$ and Co_xS_y by the reaction between S from Na_3PS_4 and the O and Co from $Na_{0.5}CoO_2$, respectively. This is accompanied by the reduction of P in Na_3PS_4 to form Na_3P. We will discuss the possible reasons for the discrepancy between the AIMD results and thermodynamic approximations in the Discussion section.

4.3.4 Buffer/Cathode, SE and Anode Interfaces

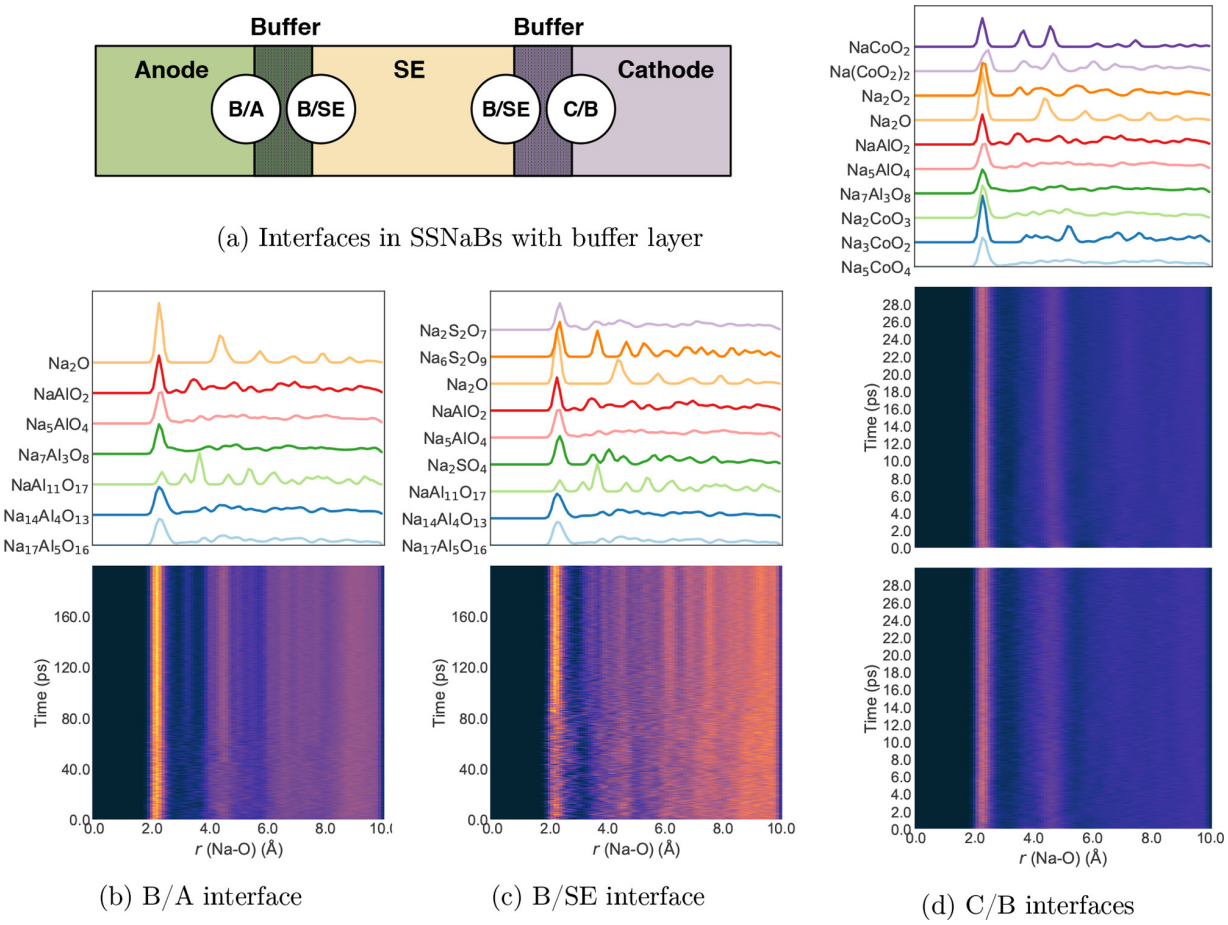

(a) Interfaces in SSNaBs with buffer layer

(b) B/A interface

(c) B/SE interface

(d) C/B interfaces

Figure 4.6: (a) Schematic diagram of interfaces in $NaCoO_2/Na_3PS_4/Na$ SSNaB with Al_2O_3 buffer layer. Evolution of the Na-O in (b) the B/A interface, (c) B/SE interface and (d) the C/B interfaces with respect to AIMD simulation time. Note in (d), the middle and bottom heat maps are discharged $NaCoO_2/Al_2O_3$ and charged $Na_{0.5}CoO_2/Al_2O_3$ interfaces respectively and only some references are shown for clarity.

From Figure 4.6 as well as Figures S7-9 in Supporting Information, we find that generally, the Al_2O_3 interfaces with the Na anode, Na_3PS_4 SE and $NaCoO_2$ cathode are relatively stable, with little change in the RDFs of most bonds. This is consistent with the thermodynamic predictions showing relatively low/zero driving force for the reaction between Al_2O_3 and the electrodes and Na_3PS_4.

4.4 Discussion

4.4.1 Prediction of Interfacial Reaction Products

Comparing the three approaches to predicting interfacial reactions presented in this work, we may conclude that there is a reasonable agreement between the predicted reaction products and driving forces, especially at the SE/anode interface. To take the Na_3PS_4/Na interface as an example, all approaches predict Na_3P and Na_2S among the interfacial reaction products, in line with experimental findings. [98] Both the multi-species chemical reactivity (Approach 2) and explicit interface modeling (Approach 3) approaches predict low reactivities between the commonly used Al_2O_3 buffer material and the cathode, SE and anode, again, in line with experimental findings.[98, 100, 101, 102]

However, there are significant differences in the predictions of the interfacial reaction products at the more complex cathode/SE interfaces, where multiple species with different mobilities generally participate in the reaction. Here, approach 1 (electrochemical reactivity), where ultra-fast alkali diffusion is assumed, is a rather blunt approximation and predicts the same interfacial products regardless of cathode chemistry.

Approach 2 (chemical reactivity), which assumes multi-species equilibrium, provides a more realistic picture in the limit of full thermodynamic equilibrium. This limit applies at high temperatures (e.g., synthesis conditions) or long time-frames. In general, this approach predicts that mixing of non-polyanion cathodes (e.g., $NaCoO_2$) and polyanion (e.g., ${PS_4}^{3-}$) SEs tend to lead to large interfacial reaction energies due to the exchange of polyanion cation, e.g., to form ${PO_4}^{3-}$). This is consistent with previous theoretical and experimental studies. [18]

Finally, approach 3 (kinetic interface model) provides the most realistic picture of interfacial reactivity, albeit at relatively small cell sizes and short time scales. For the $NaCoO_2$ cathode and Na_3PS_4 SE, the AIMD simulations predict that the initial reaction between the two materials, especially in the case of the charged cathode, comprises ${SO_4}^{2-}$ compounds and Na_3P, with no

evidence of PO_4^{3-} formation. We note that the P in Na_3PS_4 are enclosed within PS_4^{3-} tetrahedra. Our hypothesis therefore is that the initial interface reaction takes place via the oxidation of the more accessible S^{2-} on the outside of these tetrahedra by the highly oxidizing cathode to form SO_4^{2-}, with the concomitant reduction of P to form Na_3P. In other words, the formation of the relatively stable SO_4^{2-} groups is kinetically preferred over the thermodynamically preferred PO_4^{3-} groups. Once the tightly-bound SO_4^{2-} units are formed, we do not observe any further reaction to form PO_4^{3-}. We acknowledge that a possible reason could be that the time scale of our AIMD simulations are too short to observe PO_4^{3-} formation. We have performed additional AIMD simulations of the more reactive charged $Na_{0.5}CoO_2/Na_3PS_4$ interface at an elevated temperature of 600K; no PO_4^{3-} was observed over 20 ps of simulation time. It should be noted that the voltage in the interface model is not the equilibrium voltage, and hence, the rates of reaction may differ from the true reaction rates in an actual battery cell, especially if long range electron transfer are involved.[113] Indeed, the predicted phases are relatively consistent across both the charged and discharged cathodes, with the main difference being the observed reaction rates. **We hope that these predictions can be verified by future experiments, e.g., via XPS characterization of the interface.**

It should be noted that all three approaches have limitations, and the best results are obtained by considering the predictions from all three approaches. The chemical and electrochemical activity predictions are computationally relatively inexpensive, but makes certain simplifying assumptions above the mobilities of the various species. The explicit interface model is more realistic, but its high computational expense limits the length and time scale of the simulations. Further, the RDF analysis to ascertain the reaction products in the interface simulation becomes combinatorially more complex as the number of species, and hence more candidate RDFs to be analyzed, increases. Nevertheless, we have outlined an elimination approach in which a vast number of candidates can be excluded on the basis of a few bond choices. We believe this is a useful approach that can be extended to other heterogeneous interfaces beyond energy storage.

4.4.2 Choice of Buffer Layers

Another major finding from our work is the identification of buffer layers for various cathode/SE and anode/SE combinations. Despite the imperfect accuracy in predicting exact reaction products/mechanisms (as discussed above), Figure 4.3 still provides useful guidance on materials selection strategies. We chose to focus on binaries oxides in this work because oxides are common and easy to handle, and thin films of binary oxides can be fabricated with well-controlled thicknesses using modern deposition methods such as atomic layer deposition. Most binary oxides are also chemically stable electronic insulators.[112]

The main observation from Figure 4.3 is that buffer layer selection should be tailored according to electrode and SE chemistry. Sc_2O_3, SiO_2, TiO_2, ZrO_2 and HfO_2 all have similar or even better chemical stability against thiophosphate SEs and TM oxide cathodes compared to the commonly used Al_2O_3. On the Na anode/SE interface, the most promising coating materials are Sc_2O_3, ZrO_2 and HfO_2. It should be noted that a key limitation of this analysis is that the diffusion of Na through the buffer layer has not been taken into account. Any buffer material must exhibit reasonable Na diffusivity to ensure that rate capability is not adversely affected, even after accounting for the short diffusion length scales in the buffer layer (typically $\sim$ 10-370 nm [7, 16] thick).

4.5 Conclusion

To conclude, the reactions at the interfaces between common electrodes, solid electrolytes and buffer oxides were studied using a range of thermodynamic and kinetic interfacial models in this work. In the limit of full thermodynamic equilibrium, we find that exchange reactions, especially between simple oxides and thiophosphate groups to form PO_4^{3-}, are the main reason for large driving forces for cathode/SE interfacial reactions. Similarly, high reactivity with large volume changes are predicted at the Na anode/SE interface, while the $Na_2Ti_3O_7$ anode

is predicted to be much more stable against a broad range of SEs. We have also identified several promising binary oxide buffer materials with similar or better chemical stability with most electrodes and solid electrolytes than the commonly used Al_2O_3. In particular, HfO_2 is a promising candidate that deserves further experimental consideration. Finally, we find that an explicit AIMD simulation of the $NaCoO_2$/Na_3PS_4 interface predicts that the formation SO_4^{2-}-containing compounds and Na_3P are kinetically favored over the PO_4^{3-}-containing compounds. These insights into interfacial reactions provide useful guidelines for designing stable electrode/SE and buffer/SE interfaces, a crucial bottleneck in the development of all-solid-state sodium-ion batteries.

4.6 Acknowledgement

Chapter 4, in full, is a reprint of the material "Probing solid–solid interfacial reactions in all-solid-state sodium-ion batteries with first-principles calculations" as it appears in Chemistry of Materials, Hanmei Tang, Zhi Deng, Zhuonan Lin, Zhenbin Wang, Iek-Heng Chu, Chi Chen, Zhuoying Zhu, Chen Zheng, Shyue Ping Ong, 2017 Dec 28;30(1):163-73. The dissertation author was the primary investigator and author of this paper.

Chapter 5

Revealing Nanoscale Solid-Solid Interfacial Phenomena for Long Life High Energy All-Solid-State Batteries

5.1 Introduction

All-solid-state batteries (ASSBs) have attracted much attention in recent years, owing to their many advantages over liquid counterparts. These include enhanced safety, absence of electrolyte leakage, and improved energy densities from enabling the use of metallic lithium anode.[114] While various oxide and sulfide solid-state electrolytes (SSEs) with high Li+ conductivities have been reported over the years, [115] sulfide-based superionic conductors are considered more practical as they have higher ionic conductivities, facile room-temperature synthesis, and favorable mechanical properties that allow intimate contact with electrodes. [116, 117] However, the electrochemical performance of these sulfide superionic conductors are still not comparable with the conventional liquid electrolytes, mainly as a result of severe interfacial problems between electrodes and sulfide SSEs. [118, 102, 7] Moreover, the narrow electrochemi-

cal stability windows of sulfide SSEs induce decomposition during charging, forming a highly resistive solid electrolyte interphase (SEI). [7, 119, 120] Although such phenomena have been commonly reported in the literature using routine electrochemical tools, [121, 100, 122, 101] these methods alone cannot provide detailed spatial and chemical information at the interface as well as the identity of its products. As such the coupled effects of interfacial reactions, electrochemical decomposition and its resulting interface passivation are still not fully investigated. Understanding the consequences of the decomposition process and its progression over extended cycling is essential toward designing stable interfaces to enable practical ASSBs.

To understand these effects, the various reactions are first decoupled by controlling the electrochemical state of each material according to the schematic illustrated in Figure 5.1. First-principles calculations are used to identify thermodynamically favored decomposition products along with atomic-scale visualization of interfacial reactions, followed by experimental tools such as X-ray diffraction (XRD), X-ray absorption spectroscopy (XAS), cryogenic electron microscopy, X-ray photoelectron spectroscopy (XPS), and Raman to determine their presence and spatial distributions. The results show that $LiNi_{0.85}Co_{0.1}Al_{0.05}O_2$ (NCA) is intrinsically unstable with Li6PS5Cl (LPSCl), and this instability is further aggravated at the higher charge states. We demonstrate that such unwanted reactions can be avoided by using a 5 nm thick $LiNbO_3$ (LNO) coating at the cathode. We also show that electrochemical oxidation of LPSCl occurs at the first charge, forming a stable self-passivating layer that enables long cyclability of the ASSB.

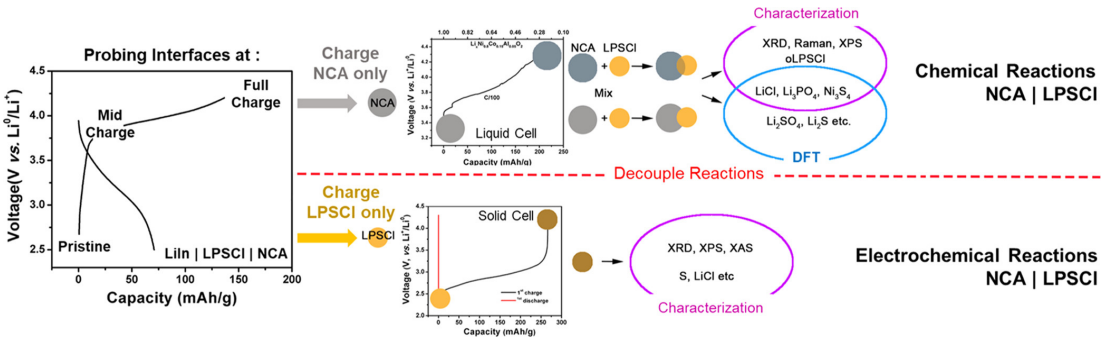

Figure 5.1: Schematic of interfacial study in this work. The chemical reactions at $LiNi_{0.85}Co_{0.1}Al_{0.05}O_2$ (NCA) - Li_6PS_5Cl (LPSCl) interface, and electrochemical decomposition of LPSCl were segregated and their reaction products explored with both experimental tools and computation.

5.2 Methods

All density functional theory (DFT) calculations in this work were performed using Vienna *ab initio* simulation package (VASP) [69] within the projector augmented wave approach [70] using the Perdew-Burke-Ernzerhof (PBE) generalized-gradient (GGA) functional [71]. All analyses are performed using the Python Materials Genomics (Pymatgen) package [27] and Pymatgen-diffusion package. [32] The Size of diffusion channel R_c is the free radius determined using *Zeo++*, an open source topological analysis package.

5.2.1 DFT Parameters

Geometry optimization

For structure relaxations and total energy calculations, GGA with Hubbard (+U) correction was applied. All calculation parameters, such as the plane wave energy cutoff of 520 eV and k-point density of at least 1000/(number of atom) were selected to keep consistent with the settings of Materials Project (MP). [105, 39]

AIMD

Non-spin-polarized AIMD calculations were performed using Gamma-point grid and a time step of 2 fs up to 50 ps. A NpT-NVT scheme was applied to minimize the interfacial stress caused by lattice mismatch, which is similar to previous work by the authors. [11]

5.2.2 NCA Enumeration

To handle the large number of orderings of the highly-disordered NCA, an enumeration of all symmetrically distinct $LiNi_{0.89}Co_{0.11}O_2$ (NCO) structures were carried out first using the disordered $LiCo_{0.1}Ni_{0.9}O_2$ (ICSD ID: 174452) obtained from ICSD database (Inorganic Crystal Structure Database. Retrieved from http://icsd.fiz-karlsruhe.de). Then the NCO configuration with the lowest energy was used to generate symmetrically distinct NCA orderings by substituting Co or Ni sites to Al atoms. Finally, the NCA structure with the lowest energy ($LiNi_{0.85}Co_{0.11}Al_{0.04}O_2$) was selected to construct phase diagram.

The energy above hull (E_{hull}) is a descriptor to evaluate the phase stability of a given compound at 0 K. [35] An E_{hull} of 0 meV/atom indicates the compound is stable phase and a more positive value corresponding to a less stable phase. For example, to evaluate the phase stability of NCO, one needs to first construct the phase diagram in Li-Ni-Co-O chemical space and determine the energy above hull for the most stable NCO configuration. Using this method, we have verified the NCO and NCA are all stable phases with an E_{hull} value of 0 meV/atom.

5.2.3 Chemical Stability at Selected Interfaces

Chemical equilibriums of interfaced formed by discharged NCA cathode, LPSCl electrolyte and LNO coating are predicted using multispecies assumption illustrated in previous work. [9, 11] A series of reactions with different reactant ratios can be determined by constructing the pseudobinary phase diagram between the two reactants (e.g. NCA and LPSCl). The more

negative value indicates a more reactive interface. For example, the reaction energy between two phases a and b can be determined using the following equation:

$$\Delta E_{\text{rxn}}(c_a, c_b) = \min_{x\in[0,1]} \frac{1}{N}\{E_{\text{eq}}[xc_a + (1-x)c_b] - xE[c_a] - (1-x)E[c_b]\}, \tag{5.1}$$

where c_a, c_b are the compositions of phases a and b and x is the proportion of c_a in the mixed reactants. $E_{eq}[xc_a + (1-x)c_b]$ refers to the total energy of the mixed composition $xc_a + (1-x)c_b$; $E[c_a]$ and $E[c_b]$ indicate the DFT total energy of composition c_a and c_b, respectively. N is the total number of atoms involved in the reaction, which normalize the unit of energy into eV/atom.

Another term related with the heterogeneous reaction is the volume change, ΔV. This is determined by comparing the total volume of the products to that of the reactants. The fully relaxed volume from DFT calculations of both reactants and products are used. A negative value indicates the total volume decrease after reaction, which may cause voids and thus less intimate contact at interface. A positive value of ΔV indicates an increased volume after reaction, which may cause additional strain and other mechanical failure at interface.

5.2.4 Electrochemical Stability of Selected Compounds

The electrochemical stability windows of the selected compositions are calculated using grand potential approach assuming the fast diffusion of Li. [34, 14] The interface is treated as an open system to Li and can be described using the chemical potential of Li or the voltage applied. This gives an voltage range (electrochemical stability window) for a given compound that within this rage the compound would not decompose due to the Li insertion or extraction.

5.2.5 Interface Construction

Considering the low concentration of Al in NCA, in ab initio molecular dynamics (AIMD) simulations were performed for the approximate interface NCO/LPSCl at half-discharged state. The initial structure of Li_6PS_5Cl (MP id, mp-985592) was obtained from MP database. The coherent interface model was constructed by matching $Li_{0.5}Ni_{0.89}Co_{0.11}O_2$ and LPSCl with a mean absolute strain of 1.75% using the algorithm proposed by Stradi et al. [38]

$$\bar{\varepsilon} = \frac{|\varepsilon_{xx}| + |\varepsilon_{xy}| + |\varepsilon_{yy}|}{3} \tag{5.2}$$

where, ε_{xx}, ε_{xy} and ε_{yy} are components of plane strain caused by matching two slabs.

5.2.6 Geometry Analysis

Changing of the bonds are tracked using radial distribution functions (RDFs) of various species at the interface. Then RDFs of interface throughout the AIMD simulations are compared with known crystalline compounds in Li-Co-Ni-P-S-Cl chemical system extracted from MP database with an E_{hull} value less than 20 meV/atom. In consider of the limited time scale of AIMD simulation, the P-P and Cl-Cl pairs were not used in matching RDFs due to the low concentration (< 0.05) of P and Cl atoms as well as their commonly long bond lengths (> 3Å). As a result, the RDF spectra matching were performed for the rest 13 pairs, which is similar to previous work by the authors. [11]

5.2.7 Material Synthesis

All material synthesis, cell fabrication and testing were performed inside the glove box (MBraun MB 200B, $H_2O < 0.5$ ppm, $O_2 < 1.0$ ppm) due to high air-sensitivity of precursors and solid electrolytes. $LiNi_{0.85}Co_{0.1}Al_{0.05}O_2$ (NCA) was purchased from TODA Chemical.

Li_6PS_5Cl was synthesized by ball milling the mixture of stoichiometric amount Li_2S (99.9%, Aldrich), P_2S_5 (99.8%, Aldrich) and LiCl (99%, Aldrich). Ball milling was carried out at 600 rpm for 18 hours using a planetary ball mill apparatus (Retsch, PM400) and an air-tight zirconia pot (50 ml) with 11 ZrO_2 balls of 10 mm size. $Li_{0.5}In$ alloy was prepared by mixing stoichiometric amount of lithium powder (FMC) and indium powder (Alfa Asear 99.6%) for 5 mins in the vortex mixer.

Solution method was employed to coat $LiNbO_3$ (LNO) on the NCA particle. To be specific, lithium ethoxide (Aldrich 99.8%) and niobium ethoxide (Aldrich 99%) were first dissolved in dry ethanol (Aldrich 99.8%). NCA powder was added into the solution and the solution was stirred for one hour. The dry powder was collected by evaporating the ethanol using rotator vapor and followed by the heat-treatment at 450°C for one hour to get the LNO coated NCA. The coated powder was dried overnight at 100°C under vacuum before transferring to the inside of the glove box for storage and fabrication of solid state battery. LPSCl/activated carbon composite (7:3 wt%) was made by ball mill method at 300 rpm for 30 mins using 5 mm ZrO_2 balls under Ar atmosphere.

5.2.8 Chemical Reaction between NCA and LPSCl

Both pristine and charged (bare and LNO-coated) NCA were hand mixed with LPSCl for at least 15 mins (to exaggerate the chemical reaction) using mortar pestle. The ratio of NCA and LPSCl was 11:16 (w/w). The charged samples were harvested by disassembling the coin cells inside the glove box, which were charged to 4.3 V at C/100. The pellets were made of 200 mg materials under 360 MPa pressure and used as electrode without any conductive additive and binder. The liquid electrolyte is 1 M $LiPF_6$ in ethylene carbonate (EC)/Dimethyl carbonate (DMC) (50:50 v/v).

To remove the unreacted LPSCl, the LPSCl-NCA mixture was washed by the dry ethanol solution to dissolve the LPSCl. In order to highlight these reaction products, the unreacted LPSCl

was removed by washing the NCA/LPSCl mixture with ethanol; in ethanol, LPSCl is soluble, LiCl and Li_3PO_4 are sparingly soluble, and Ni_3S_4 is insoluble. After washing, the XRD peaks of the LPSCl disappear while those new peaks are retained; LiCl, Ni_3S_4, and Li_3PO_4 were clearly identified.

5.2.9 Electrochemical Characterization

LPSCl pellet was prepared by cold press with 360 MPa pressure. The conductivity of LPSCl was measured in the Ti/LPSCl/Ti cells. The composite electrode was prepared with 10 mg of NCA, 16 mg of LPSCl and 1mg of carbon as conductive additive. All components were hand grinded with an agate mortar to make a homogeneous mixture. Solid electrolyte was pressed with 360 MPa pressure to make the pellet. 10 mg of the composite cathode was pressed on top of with same pressure. Finally, 70 mg of $Li_{0.5}In$ alloy was pressed with 144 MPa pressure on other side of the pellet. All the procedures were performed in a polyaryletheretherketone (PEEK) mould (diameter = 13 mm) with two Ti metal rods as current collectors. Fabrication of solid state Lithium metal battery was made with 50 micron meter thickness Li metal foil with applied pressure of 20 MPa. Galvanostatic charge discharge measurement was performed at different current densities and 180 mA/g is equivalent to 1C. All the cells were operated within the potential range between 2.5 and 4.3 V vs. Li/Li^+.

R2032 coin cell was used for the NCA/Li cell with liquid electrolyte. Composite slurry was made by mixing NCA powder, super P and poly(vinylidene fluoride) (PVDF) binder using N-Methylpyrrolidone as solvent. The weight ratio of the NCA, super P and PVDF were 85:10:5. The slurry was casted on Al foil and dried at 100 0C under vacuum. Li metal was used as counter and reference electrode. 1 M LiPF6 in ethylene carbonate and Dimethyl carbonate (50:50 v/v) was used as electrolyte.

Electrochemical impedance spectroscopy (EIS) was performed using Solartron 1260 impedance analyzer. Conductivity measurement of LPSCl (Ti/LPSCl/Ti) was done with an

applied AC potential of 50mV over a frequency range of 1MHz to 1Hz. Impedance measurement of the solid-state cells were performed after charging at 3.675 V (vs. Li0.5In/Li+) and kept with constant voltage of 3.675 vs. reference electrode. The AC perturbation signal was 10 mV, and the frequency range was from 10-2 to 106 Hz in the EIS.

5.2.10 Chemical Characterizations

Boron rich capillary tube (Charles Supper) was used to load few milligrams of sample for X-ray diffraction measurement. The sample was loaded inside the glove box and caped with clay before to bring outside where it was flame sealed using a butane torch. Bruker Kappa goniometer equipped with a Bruker Vantec 500 detector was used for measuring the sample. The diffraction data was collected using Cu K_α radiation at 45 kV and 50 mA.

Raman (Renishaw inVia/Bruker Innova) spectra were measured using illumination of a Modu-Laser 50 mW Ar^+ ion laser with wavelength of 514 nm. Samples for Raman measurement were made inside the glove where it was kept on top of glass slides and sealed with Kapton (to avoid the air contamination) tape before to bring it outside.

The XPS samples were prepared inside the glove box and carried outside with a sealed metal canister where it was transferred into the nitrogen filled glove box, attached with XPS chamber. Solid state cells were disassembled after different charge discharge cycle and isolate the cathode composites to prepare the XPS sample. X-ray photoelectron spectroscopy (XPS) was measured with a Kratos Axis Ultra spectrometer with a focused 500 mm Rowland circle monochromator Al K_α radiation at 15 KeV. Avantage software was used for data calibration, fitting and analyzing the chemical species at the cathode electrolyte interface. All spectra were calibrated with reference of carbon 1s peak (284.8 eV) and fitted with Shirley type background.

XAS measurements at S K-edge were performed at the Advanced Photon Source on the bending-magnet beamline 9-BM-B with electron energy of 7 GeV and average current of 100 mA. The radiation was monochromatized by a Si (111) double-crystal monochromatic. At the S

K-edge, spectra were collected in fluorescence mode using a four-element vortex detector. For energy calibration, a sodium thiosulfate sample was measured. The peak position by Gaussian fitting was adjusted to 2469.2 eV. In situ batteries were operated by a Maccor battery tester with a current density of 0.1 mA/g. Data reduction and analysis were processed by Athena software.

(S)TEM: TEM was recorded on a field emission gun JEOL-2800 at 200 kV with Gatan OneView Camera (full 4 K $\times$ 4 K resolution). STEM/EDX was performed on primary particles using a JEOL JEM-2800 at annular dark field (ADF) mode. All ADF images and were acquired at 200 kV and with a beam size of $\sim$ 5 Å. To minimize possible electron beam irradiation effects, ADF images were acquired from areas without pre-beam irradiation.

5.3 Results

5.3.1 Electrochemical Performance of Li-In-LPSCl-NCA Cell

LPSCl was synthesized via mechanical ball milling, achieving pure phase as determined by XRD and a high ionic conductivity of 1.03 $\text{mS} \cdot \text{cm}^{-1}$ as measured by electrochemical impedance spectroscopy (EIS). The ASSBs were fabricated with NCA-LPSCl-C cathode composite in the weight ratio of 11:16:1 respectively. LPSCl was used as the electrolyte, and $Li_{0.5}In$ (0.62 V vs. Li/Li^+) alloy as the anode. The assembled cell was cycled at room temperature at a rate of 0.1C. Figure 5.2 (a) depicts the voltage profiles of the ASSBs with and without LNO coating on the cathode. The cell using uncoated bare NCA delivers a low capacity of 71 $\text{mAh} \cdot \text{g}^{-1}$, while the cell using LNO coated NCA delivers a high capacity of 147 $\text{mAh} \cdot \text{g}^{-1}$, close to that of a conventional liquid cell. The LNO coated NCA shows much better rate performance then the uncoated one. The low capacity of bare NCA was likely caused by parasitic reactions at the electrode/electrolyte interface, which increases the interfacial resistance reflected by large cell polarizations in the voltage curves. The presence of 2 wt% LNO on the surface of NCA helps to mitigate this interfacial resistance growth, evident from dramatic reductions of the low-frequency semicircle in

Figure 5.2 (b). The coating was characterized with scanning transmission electron microscopy (STEM) and XPS. The STEM mapping (Figure 5.2 (c)) shows a conformal amorphous LNO coating layer on the NCA cathode and its average thickness was determined to be 5 nm. Strong signals from Nb was found in the XPS spectra (Figure 5.2 (d)), with the peak position of 3d5/2 at 207.55 eV, indicative of its +5 oxidation. The cell performance and impedance measurements validated the effectiveness of LNO coating to improve the electrochemical performance of high voltage NCA cathode. However, to investigate the fundamental reasons for these improvements, the chemical and electrochemical reaction components at the interface were separated, and their reaction products probed with both bulk and surface-sensitive characterization tools. Additionally, computational calculations were used to support these findings, which will be discussed in later sections.

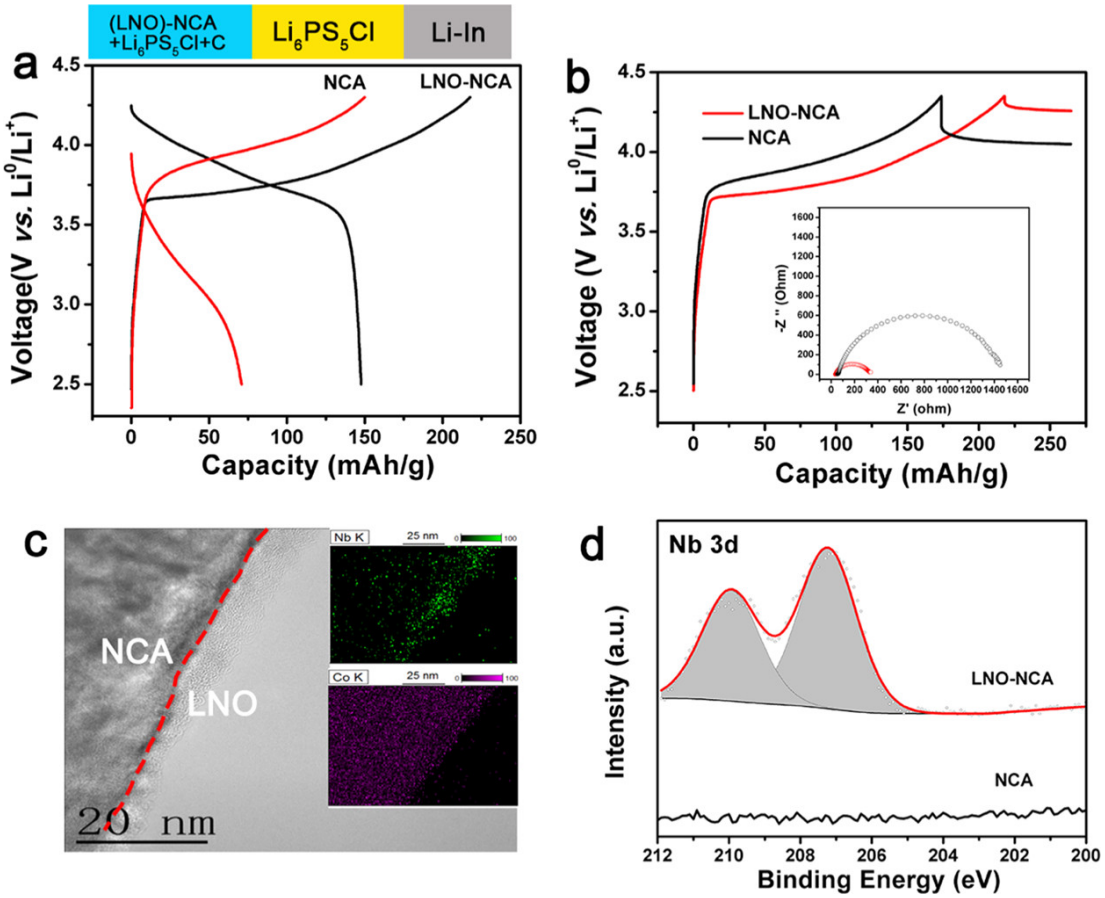

Figure 5.2: Comparisons between bare and LNO coated NCA. (a) Voltage profile of the first cycle and (b) overpotential curves after the first charge cycle, inset compares their corresponding impedance growths. (c) STEM image and (d) XPS binding energies of Nb 3d regions. The inset images in (c) compares elemental distribution of Nb (green) and Co (violet), measured via energy-dispersive X-ray spectroscopy (EDX).

5.3.2 Chemical Reactions between LPSCl and NCA

The spontaneous chemical reactions between NCA and LPSCl were examined by physically mixing LPSCl with bare NCA or LNO-NCA (Figure 5.2 (b)) at both the pristine and charged state respectively (Figure 5.3). Charged NCA was harvested from a cell using liquid electrolyte charged to 4.3V (Figure 5.3a). From XRD analysis of pristine NCA and LPSCl, new diffraction peaks were observed upon mixing of both powders. Presence of these peaks are indicative of new phases formed from chemical reactions between the electrode and electrolyte.

Such chemical reaction become more severe when the charged NCA was used (to 4.3 V vs. Li/Li^+), with intense peaks from new phases forming as seen in Figure 5.3 (c). This is expected as the charged NCA is more reactive than pristine NCA due to its higher oxidation state. These new peaks can be assigned to LiCl, Ni_3S_4, and Li_3PO_4 along with the formation of additional other unknown phases (Figure 5.3 (c)). By contrast, no new peaks were found in the XRD pattern of the LNO-NCA/LPSCl mixture, indicating that the LNO coating is able to suppress the chemical reactions that occur between bare NCA and LPSCl. To corroborate these observations, XPS was conducted to confirm the three major interfacial products formed at the interface.

Binding energies measured in the Ni 2p3/2 region of bare NCA showed a red shift from 857.3 eV to 853.7 eV after mixing with LPSCl, suggesting the reduction of Ni to form Ni_3S_4 or NiS_2. [123] Additionally, both S and P regions show partial oxidation, reflected as new peaks at higher binding energies. The new peak in the S 2p region corresponds to Ni3S4 or NiS2 and phosphorus polysulfide (P_2S_x), while those in the P 2p region originate from the P_2S_x and formed P-O bonds. [124, 125] These observations agree with computational phase equilibria at the NCA/LPSCl interface, which will be discussed later. Formation of such compounds results in the formation of a highly resistive interfacial layer that impedes Li^+ transport. However, these can be avoided when LNO coating is used. From the XRD patterns, none of the previously mentioned byproducts are found in the mixtures of charged LNO-NCA and LPSCl (Figure 5.3 (c)). This demonstrates the coating's ability to prevent parasitic reactions between the cathode and electrolyte at both the pristine and charged states.

Raman spectroscopy was also performed to examine the short-range structural changes at the cathode/electrolyte interface. As shown in Figure 3d, LPSCl exhibits t1g symmetric stretching mode (PS_4^{3-}) centered at 425 cm^{-1} while NCA shows vibrational modes at wavenumbers 470, 550 and 1100 cm^{-1} which relate to vibrational modes between transition metals and oxygen [126]. When LPSCl was mixed with either pristine or charged NCA, no visible new peaks are seen. Low concentrations of interfacial products buried under unreacted NCA and LPSCl likely

drowned the signals from the interfacial products. To enhance signals from these products, excess LPSCl in the mixture was washed away with ethanol, revealing two new peaks at 284 and 940 cm^{-1}, attributed to Ni_3S_4 and Li_3PO_4 respectively. [127, 128] These findings are consistent with the XRD results. However, these were once again not observed in the charged LNO-NCA/LPSCl mixture, further confirming the effectiveness of LNO coating to prevent electrode/electrolyte interfacial reactions.

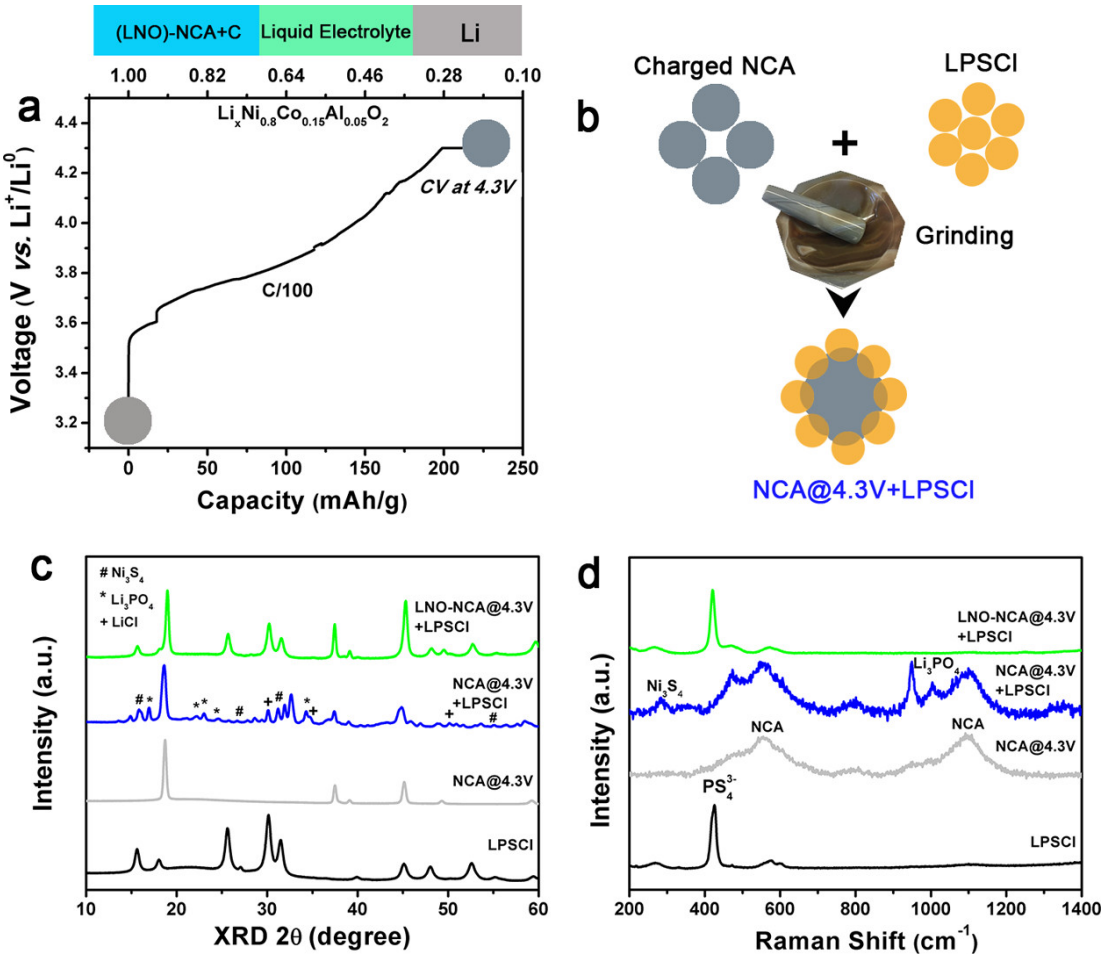

Figure 5.3: Chemical reaction characterization between LPSCl and NCA. (a) Potential curve of NCA charged to 4.3 V in a liquid cell. Similar profiles are seen for LNO-NCA. (b) Schematic of sample mixture preparation used for (c) XRD and (d) Raman spectra of each mixture at different states of charge.

5.3.3 First Principles Calculations

Figure 5.4a shows the density functional theory (DFT)-computed reaction diagrams between NCA and LPSCl and LNO and LPSCl at various mixing compositions. The highly exothermic (negative) reaction energies for NCA and LPSCl means that NCA and LPSCl are chemically unstable with each other. Upon contact, among the major products formed include LiCl, Li_3PO_4, and Ni_3S_4/NiS_2, especially closer to the LPSCl (reactions 1-3 labeled in Figure 5.4a). These predictions agree with our characterization study (using XRD, XPS, Raman, and TEM) discussed in the previous section. While additional products such as Li_2S and Li_2SO_4 are expected, they could not be detected experimentally, possibly due to further exchange reactions with LPSCl to form Li_3PO_4 or LiCl. Conversely, the LNO coating is predicted to have an order of magnitude less exothermic reaction energy with LPSCl (Figures 5.4a) leading to greater improvements in interfacial stability and reduced formation of the undesirable products.

Using a 50% state of charge provides a realistic visualization of interfacial phenomena during the bulk of cell cycling duration compared to a pristine or fully charged state. The explicit model of the half-charged interface is shown in Figure 5.4c. The dynamic changes at 50% state of charge were simulated through ab *initio* molecular dynamics (AIMD) at 300 K, and the variation of the structure was tracked using radial distribution function *g(r)* (RDF), which is similar to previous work by the author. [11] The lower part in Figure 5.4b shows the evolution of P-O pair during the first 50 ps at the half-charged NCA/LPSCl interface; the upper part plots P-O RDF of the known crystalline compounds in Li-Co-Ni-P-S-Cl chemical system extracted from Materials Project (MP) database [105, 39] and the interface model before simulation is also provided as a reference structure labeled as “before MD”. At the very beginning of the simulation, no P-O bonds can be found matching those in $[PO_4]^{3-}$ tetrahedra ($\sim$ 1.5 Å) and its initial formation is at $\sim$ 2 ps. This oxidation process of PS_4 is consistent with the thermodynamic prediction of forming Li3PO4 at equilibrium as well as experimental characterizations.

As a summary, Figure 5.4c shows all of the new bonds found after AIMD simulation

as well as the model before AIMD. In addition to the formation of characteristic P-O bonds discussed previously, M-S (M = Co, Ni) and Li-Cl bonds formed within the first 2 ps, which is also consistent with both the thermodynamically predicted reaction products and experimental observations of Li_3PO_4, M_xS_y (M = Co, Ni), and LiCl formation at interface after reaction. Elemental S was also found and it might come from LPSCl electrochemical decomposition, which agrees with the electrochemical product found experimentally and will be discussed in a later section. From our best understanding, this is reported for the first time that AIMD can simulate electrochemical reaction.

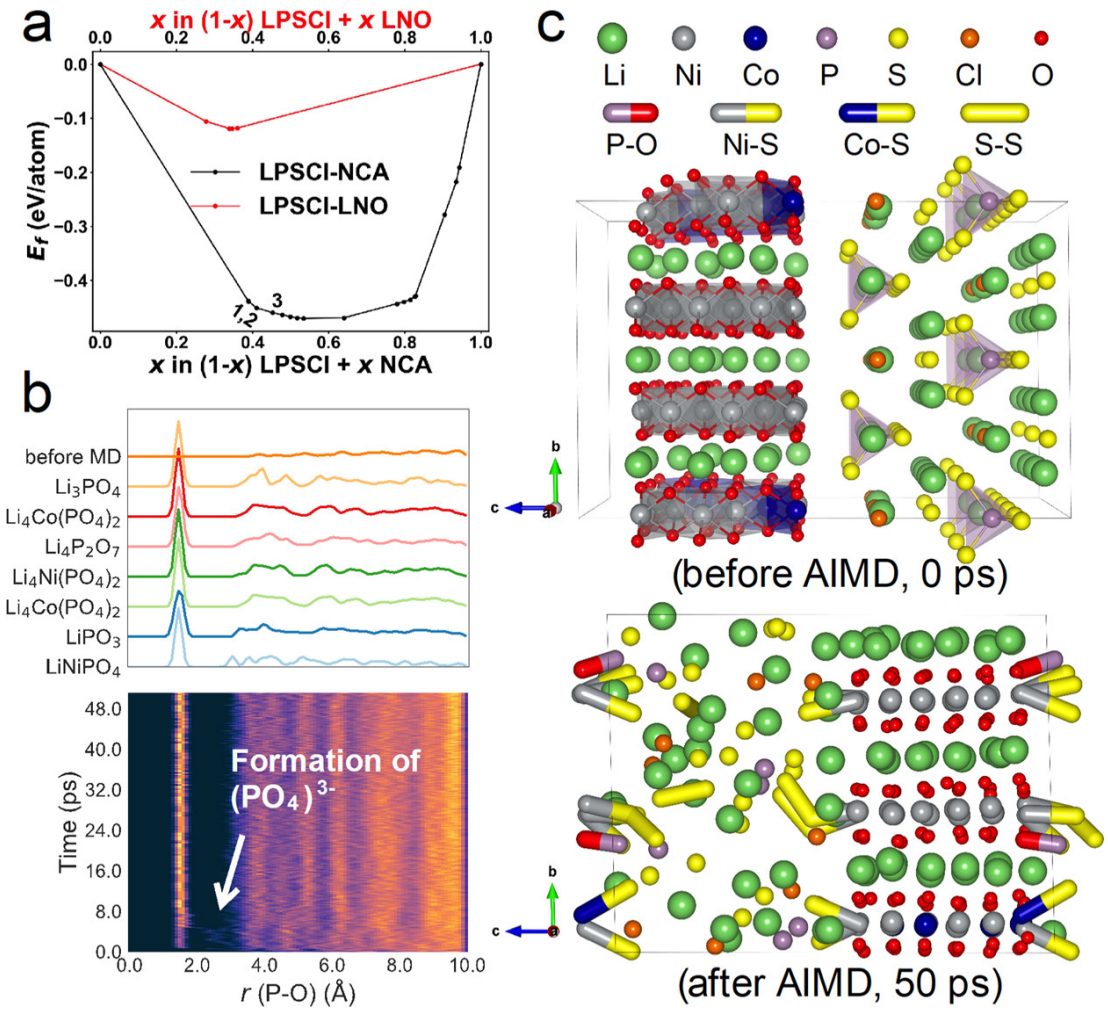

Figure 5.4: (a) Pseudo-binary phase diagram between LPSCl electrolyte and discharged NCA cathode at different mixing ratios, the red line indicates the case with LNO coating. (b) Visualization of the formation of characteristic PO bonds in PO4 polyhedra at the half-charged NCA/LPSCl interface using RDF. (c) Atomic structure of the half-charged NCA/LPSCl interface at 0 and 50 ps, which summarized the key observations in AIMD simulation.

5.3.4 New Interfacial Product oLPSCl

Although DFT calculations are a powerful tool to identify potential reaction products from material databases, unknown materials may still be present at the interface. This was found in the case of NCA/LPSCl, where a slight blue shift of the LPSCl Raman peak (PS_4^{3-}) was detected when it is mixed with bare NCA at both pristine and charged states (Figure 5.5 (a)).

Such a shift was previously reported in the structure of the $Li_{10}GeP_2S_{12}$ after partial substitution of sulfur with oxygen. [129] Note in AIMD simulation, the partially oxidized PS_4 tetrahedra might be a feature of oLPSCl. Thus, we hypothesized that the peak shift arises as a consequence of $PS_4{}^{3-}$-polyhedra in LPSCl's reaction with oxygen within NCA (Figure 5.5 (b)). To verify this, pristine LPSCl was oxidized via exposure to dry oxygen, and the resultant sample denoted as oLPSCl. Subsequent Raman analysis revealed similar peak shifts between those found in the electrode/electrolyte mixture, and that of oLPSCl (Figure 5.5 (a)). Further examination of oLPSCl with XRD showed that majority of its peaks matched the charged bare NCA/LPSCl mixture, along with the products Ni_3S_4, LiCl and Li_3PO_4 (Figure 5.5 (b)). Therefore, both Raman and XRD suggest that oxygen within NCA does participate in chemical reactions with LPSCl to form oLPSCl. The ionic conductivity of oLPSCl was also measured and found to be 10×10^6 S/cm, three orders lower than that of LPSCl (Figure 5.5 (d)). This newly formed highly insulate product contributes additional interfacial impedance on top of the existing phases identified (oLPSCl, Ni_3S_4, LiCl and Li_3PO_4). However, the use of LNO coating was able to prevent the above reaction; where no blue shift was detected when LPSCl was mixed with LNO-NCA. Further interfacial reaction was confirmed with cryo-STEM where without LNO coating, part of Ni, Co, P, S and Cl is prone to aggregate on the surface of the NCA particle.

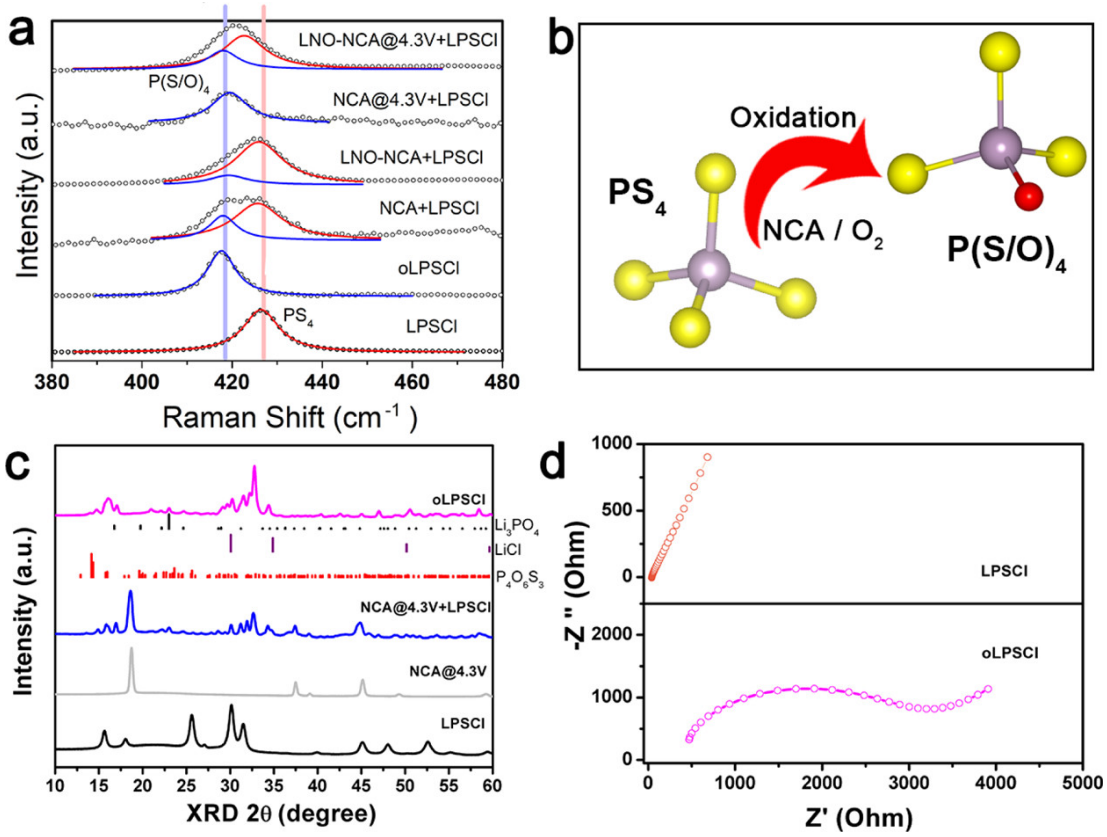

Figure 5.5: New interfacial product oLPSCl. (a) Raman spectra of the oLPSCl, mixtures of the LPSCl/bare and LNO-NCA at both charged and discharged state, (b) Illustration of O doped LPSCl to form oLPSCl, (c) XRD of the oLPSCl compared with the mixture of bare NCA/LPSCl and charged NCA, (d) EIS comparison between LPSCl and oLPSCl.

Although LNO coating was shown to eliminate chemical reactions between NCA and LPSCl, the solid state cell still shows higher polarization and lower Coulombic efficiency when compared to its liquid based counterpart (Figure 5.6 (a)). Moreover, the initial charge plateau starts at 3.3 V compared to 3.6 V in the liquid based cell. This are features of LPSCl electrochemical decomposition at the onset of charging due to its narrow electrochemical stability window. To quantify the redox activity of LPSCl, a cell comprising of only LPSCl and conductive carbon (70:30 wt%) at the cathode was used. Upon charging to 4.3 V, LPSCl was oxidized and found to deliver a large capacity of $\sim 250\ \text{mAh} \cdot \text{g}^{-1}$ (Figure 5.6 (b)), corresponding to 50% of its theoretical capacity ($499\ \text{mAh} \cdot \text{g}^{-1}$). The onset of this charge plateau is similar to that seen in

the above ASSBs, confirming the initial electrolyte decomposition in a typical cell. However, it is observed that LPSCl oxidation only occurs at the first charge cycle. No reversible capacity was found when the cell is discharged to 2.3 V. As such, it can be inferred that the decomposed species formed during the first charge terminates any subsequent electrochemical decomposition of LPSCl. This demonstrates the self-passivating nature of LPSCl. XRD and in-situ XAS was performed to determine the decomposed products of LPSCl (Figures 5.6 (c-d)). The XRD pattern shows that S and LiCl are formed while some unreacted LPSCl remains. In the S K-edge XANES spectra, the pre-edge shift to higher energies and enhancement of the elemental S peak at 2470 eV [130], suggests the continuous oxidation of S^{2-} in LPSCl to elemental S during charging.

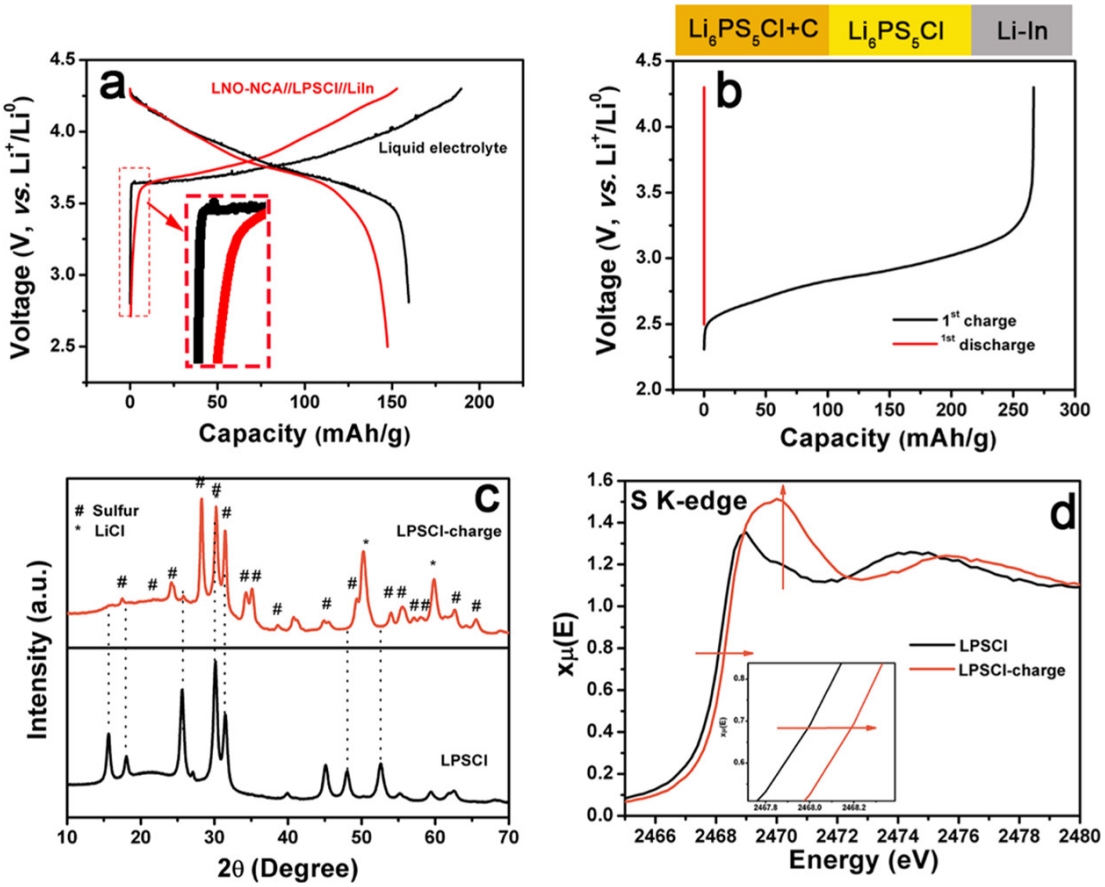

Figure 5.6: Characterization of electrochemical decomposition products of LPSCl. (a) Voltage profile of LNO-NCA with solid-state electrolyte and liquid electrolyte at the first cycle, (b) voltage profile of LPSCl-conductive carbon composite (70:30 wt%), (c) XRD and (d) XAS of bare and charged LPSCl.

The self-passivating nature of LPSCl was further explored with XPS. As shown in Figures 5.7 (a-b), new peaks are found in both the S 2p and P 2p regions after the 1st charge. These are assigned to Li_2S_x and P_2S_x species from the oxidative decomposition of LPSCl. [131] As expected, intensities of these peaks do not change significantly after the 3rd and 50th cycle, indicating that little additional decomposition occurs after the 1st charge. As a result, the initial charge plateau previous observed between 2.3-3.6 V at the 1st cycle vanishes at the 2nd cycle (Figure 5.7 (c)). This self-terminative electrolyte decomposition was subsequently found to enable excellent cycling stability of the ASSB, with a capacity retention of (93%) at 100 cycles (Figure 5.7 (d)).

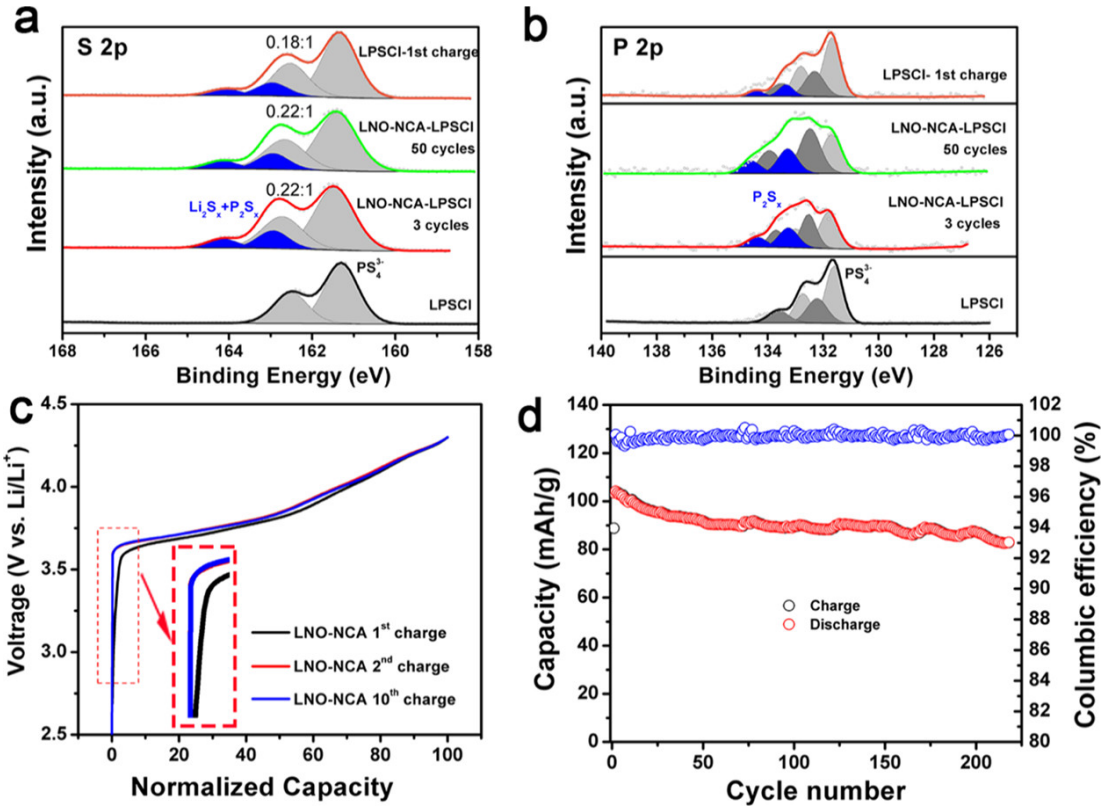

Figure 5.7: XPS spectra of S (a) and P 2p (b) of LPSCl at various cycles, the charging profile (c) of LPSCl and NCA-LPSCl ASSBs at the 1st, 2nd and 10th cycle; cycling stability of (d) ASSBs for LNO-coated and bare NCA at rate of C/3.5.

5.4 Discussion

The electrochemical performance of ASSBs is mainly governed by the properties of the interface between the electrode and electrolyte. Solid electrolytes with higher ionic conductivities but lower interface stability will ultimately yield low Coulombic efficiencies and poor cyclic performance, making it an unfavorable tradeoff when electrolyte material factors are considered. Constructing a stable interface with a low charge-transfer resistance is essential for long-term operation of any sulfide-based ASSB. As such, protective coating materials such as LNO used in this study are vital to prevent undesirable side reactions at the interface. Building upon this fact, the properties of other potential coating materials were screened by the DFT calculations to offer alternative options in the interfacial design (Figure 5.8). Factors considered include reaction energies with NCA ($\Delta E_{\text{rxn}}^{\text{NCA}}$) and with LPSCl SE ($\Delta E_{\text{rxn}}^{\text{SE}}$) in eV/atom, volume change after reacting with NCA (ΔV_{NCA}) and SE (ΔV_{SE}), diffusion channel radius (R_c) in Åas an indicator of ionic diffusivity, band gap (E_g) in eV, and energy above hull (E_{hull}) in eV/atom. [132, 32] Evaluations of ΔE_{rxn}, ΔV, R_c, and E_{hull} are illustrated in Methods section; E_g values were directly extracted from MP database. A good coating candidate should be chemically and electrochemically stable with both cathode (e.g., NCA) and electrolyte (e.g., LPSCl) and possess the ability to conduct Li^+. Based on these criteria, $Li_4Ti_5Ox_{12}$, $LiAlO_2$, Li_2SiO_3, and $Li_2La_2Ti_3O_{10}$ were determined to be promising alternatives with high oxidative stability and negligible (electro)chemical reactions with high-voltage cathodes and sulfide electrolytes. Poor coating materials include Li_2PNO_2 and $Li_7La_3Zr_2O_{12}$ which both exhibit limited oxidative stabilities at 2.9 V.

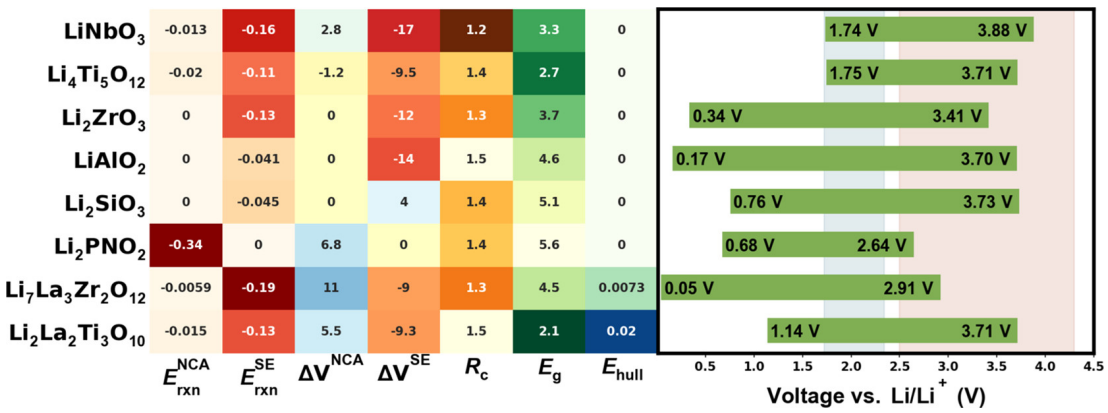

Figure 5.8: Properties of possible coating materials at the NCA/LPSCl interface. Left: Properties related to interfacial reactivity. From left to right, are reaction energies with pristine NCA ($\Delta E_{\text{rxn}}^{\text{NCA}}$) and with LPSCl SE ($\Delta E_{\text{rxn}}^{\text{SE}}$) in eV/atom, percentages of volume change after reacting with NCA (ΔV_{NCA}) and SE (ΔV_{SE}), diffusion channel radius (R_c) in Å, band gap (E_g) in eV, and energy above hull (E_{hull}) in eV/atom. Right: The electrochemical windows of selected coatings; the LPSCl electrochemical window, and NCA voltage range are labeled as blue and red ribbons for reference.

While protective coating layers prevent reactions between the cathode and electrolyte, they cannot prevent intrinsic electrochemical decomposition of the electrolyte itself. Because of the narrow electrochemical stability windows of sulfides, such decompositions are inevitable. Despite the formation of insulative SEI components such as LiCl, S, and P_2S_x, it forms a stable passivation layer that prevents further decomposition of the electrolyte. This effectively widens the operating potential of LPSCl and allows for extended cyclability of the ASSB. [10]

5.5 Conclusion

This work sheds light on the underlying causes of interfacial instability between NCA and LPSCl. Contributions from both chemical reactions between NCA and LPSCl and the electrochemical decomposition of LPSCl were separated and characterized, respectively. XRD, XAS, XPS, Raman, and cryo-TEM were used to identify the interfacial products of Ni_3S_4, LiCl, Li_3PO_4, and oLPSCl from the spontaneous chemical reaction between NCA and LPSCl. These findings were also supported by DFT calculations and AIMD simulations. Subsequently, the

effectiveness of a coating material LNO to prevent these chemical reactions was demonstrated. The electrochemical decomposition of LPSCl was studied and determined to only occur in the first cycle. Its decomposition products were found to form a self-passivating interface, allowing excellent long-term cycling stability of the ASSBs. These findings elucidate the reaction mechanism at both the NCA/LPSCl interface and LPSCl decomposition, which has not been fully understood till date. The knowledge gained here highlights the importance of protective coating layers and the passivating nature of sulfide solid electrolytes and can be extended to new coating material selection philosophy for other high-voltage cathodes used in sulfide-based ASSBs.

5.6 Acknowledgement

Chapter 5, in full, is a reprint of the material "Revealing Nanoscale Solid-Solid Interfacial Phenomena for Long-Life and High-Energy All-Solid-State Batteries" as it appears in ACS applied materials & interfaces, Abhik Banerjee, Hanmei Tang, Xuefeng Wang, Ju-hsiang Cheng, Han Nguyen, Minghao Zhang, Darren Tan, Thomas Wynn, Erik Wu, Jean-Marie Doux, Tianpin Wu, Lu Ma, George E Sterbinsky, Macwin Dsouza, Shyue Ping Ong, and Ying Shirley Meng, 2019 Oct 23. The dissertation author was the primary investigator and author of this paper.

Bibliography

[1] M. S. Whittingham. History, Evolution, and Future Status of Energy Storage. 100:1518–1534.

[2] James H. Williams, Benjamin Haley, Fredrich Kahrl, Jack Moore, Andrew D. Jones, Margaret S. Torn, and Haewon McJeon. Pathways to Deep Decarbonization in the United States.

[3] Yung-Fang Yu Yao and J.T. Kummer. Ion exchange properties of and rates of ionic diffusion in beta-alumina. 29(9):2453–2475.

[4] John B. Goodenough and Kyu-Sung Park. The Li-Ion Rechargeable Battery: A Perspective. 135(4):1167–1176.

[5] Kazunori Takada. Progress and prospective of solid-state lithium batteries. 61(3):759–770.

[6] Anubhav Jain, Yongwoo Shin, and Kristin A. Persson. Computational predictions of energy materials using density functional theory. 1(1):15004.

[7] Atsushi Sakuda, Akitoshi Hayashi, and Masahiro Tatsumisago. Interfacial Observation between LiCoO 2 Electrode and Li 2 S-P 2 S 5 Solid Electrolytes of All-Solid-State Lithium Secondary Batteries Using Transmission Electron Microscopy †. 22(3):949–956.

[8] Gerbrand Ceder, Marc Doyle, Pankaj Arora, and Yuris Fuentes. Computational Modeling and Simulation for Rechargeable Batteries. 27(8):619–623.

[9] William D. Richards, Lincoln J. Miara, Yan Wang, Jae Chul Kim, and Gerbrand Ceder. Interface Stability in Solid-State Batteries. 28(1):266–273.

[10] Yizhou Zhu, Xingfeng He, and Yifei Mo. Origin of Outstanding Stability in the Lithium Solid Electrolyte Materials: Insights from Thermodynamic Analyses Based on First-Principles Calculations. 7(42):23685–23693.

[11] Hanmei Tang, Zhi Deng, Zhuonan Lin, Zhenbin Wang, Iek-Heng Chu, Chi Chen, Zhuoying Zhu, Chen Zheng, and Shyue Ping Ong. Probing Solid-Solid Interfacial Reactions in All-Solid-State Sodium-ion Batteries with First Principles Calculations. 30:163–173.

[12] William Davidson Richards, Tomoyuki Tsujimura, Lincoln J. Miara, Yan Wang, Jae Chul Kim, Shyue Ping Ong, Ichiro Uechi, Naoki Suzuki, and Gerbrand Ceder. Design and synthesis of the superionic conductor Na10SnP2S12. 7:11009.

[13] Iek-Heng Chu, Christopher S. Kompella, Han Nguyen, Zhuoying Zhu, Sunny Hy, Zhi Deng, Ying Shirley Meng, and Shyue Ping Ong. Room-Temperature All-solid-state Rechargeable Sodium-ion Batteries with a Cl-doped Na3PS4 Superionic Conductor. 6(1):33733.

[14] Shyue Ping Ong, Yifei Mo, William Davidson Richards, Lincoln Miara, Hyo Sug Lee, and Gerbrand Ceder. Phase stability, electrochemical stability and ionic conductivity of the Li 10+/-1 MP 2 X 12 (M = Ge, Si, Sn, Al or P, and X = O, S or Se) family of superionic conductors. 6(1):148–156.

[15] Yifei Mo, Shyue Ping Ong, and Gerbrand Ceder. First Principles Study of the Li 10 GeP 2 S 12 Lithium Super Ionic Conductor Material. 24(1):15–17.

[16] Sebastian Wenzel, Simon Randau, Thomas Leichtweiß, Dominik A. Weber, Joachim Sann, Wolfgang G. Zeier, and Jürgen Janek. Direct Observation of the Interfacial Instability of the Fast Ionic Conductor Li 10 GeP 2 S 12 at the Lithium Metal Anode. 28(7):2400–2407.

[17] Yizhou Zhu, Xingfeng He, and Yifei Mo. First principles study on electrochemical and chemical stability of solid electrolyte–electrode interfaces in all-solid-state Li-ion batteries. 4(9):3253–3266.

[18] Yaosen Tian, Tan Shi, William Davidson Richards, Juchuan Li, Jae Chul Kim, Shouhang Bo, and Gerbrand Ceder. Compatibility issues between electrodes and electrolytes in solid-state batteries. 10(5):1150–1166.

[19] G. Ceder, Y.-M. Chiang, D. R. Sadoway, M. K. Aydinol, Y.-I. Jang, and B. Huang. Identification of cathode materials for lithium batteries guided by first-principles calculations. 392(6677):694–696.

[20] K. Kang. Electrodes with High Power and High Capacity for Rechargeable Lithium Batteries. 311(5763):977–980.

[21] Georg K. H. Madsen. Automated Search for New Thermoelectric Materials: The Case of LiZnSb. 128(37):12140–12146.

[22] Hong Zhu, Geoffroy Hautier, Umut Aydemir, Zachary M. Gibbs, Guodong Li, Saurabh Bajaj, Jan-Hendrik Pöhls, Danny Broberg, Wei Chen, Anubhav Jain, Mary Anne White, Mark Asta, G. Jeffrey Snyder, Kristin Persson, and Gerbrand Ceder. Computational and experimental investigation of TmAgTe $_2$ and XYZ $_2$ compounds, a new group of thermoelectric materials identified by first-principles high-throughput screening. 3(40):10554–10565.

[23] T. F. Jaramillo, K. P. Jorgensen, J. Bonde, J. H. Nielsen, S. Horch, and I. Chorkendorff. Identification of Active Edge Sites for Electrochemical H2 Evolution from MoS2 Nanocatalysts. 317(5834):100–102.

[24] Felix Studt, Irek Sharafutdinov, Frank Abild-Pedersen, Christian F. Elkjær, Jens S. Hummelshøj, Søren Dahl, Ib Chorkendorff, and Jens K. Nørskov. Discovery of a Ni-Ga catalyst for carbon dioxide reduction to methanol. 6(4):320–324.

[25] Anubhav Jain, Geoffroy Hautier, Charles J. Moore, Shyue Ping Ong, Christopher C. Fischer, Tim Mueller, Kristin A. Persson, and Gerbrand Ceder. A high-throughput infrastructure for density functional theory calculations. 50(8):2295–2310.

[26] Anubhav Jain, Shyue Ping Ong, Geoffroy Hautier, Wei Chen, William Davidson Richards, Stephen Dacek, Shreyas Cholia, Dan Gunter, David Skinner, Gerbrand Ceder, and Kristin A. Persson. Commentary: The Materials Project: A materials genome approach to accelerating materials innovation. 1(1):011002.

[27] Shyue Ping Ong, William Davidson Richards, Anubhav Jain, Geoffroy Hautier, Michael Kocher, Shreyas Cholia, Dan Gunter, Vincent L. Chevrier, Kristin a. Persson, and Gerbrand Ceder. Python Materials Genomics (pymatgen): A robust, open-source python library for materials analysis. 68:314–319.

[28] Anubhav Jain, Shyue Ping Ong, Wei Chen, Bharat Medasani, Xiaohui Qu, Michael Kocher, Miriam Brafman, Guido Petretto, Gian-Marco Rignanese, Geoffroy Hautier, Daniel Gunter, and Kristin A. Persson. FireWorks: A dynamic workflow system designed for high-throughput applications. 27(17):5037–5059.

[29] Graeme Henkelman and Hannes Jónsson. Improved tangent estimate in the nudged elastic band method for finding minimum energy paths and saddle points. 113(22):9978–9985.

[30] Bruce J Berne, Giovanni Ciccotti, and David F Coker. Classical and Quantum Dynamics in Condensed Phase Simulations. In *Classical and Quantum Dynamics in Condensed Phase Simulations*. WORLD SCIENTIFIC.

[31] Søren Smidstrup, Andreas Pedersen, Kurt Stokbro, and Hannes Jónsson. Improved initial guess for minimum energy path calculations. 140(21):214106.

[32] Zhi Deng, Zhuoying Zhu, Iek-Heng Chu, and Shyue Ping Ong. Data-Driven First-Principles Methods for the Study and Design of Alkali Superionic Conductors. 29:281–288.

[33] Lincoln J. Miara, William Davidson Richards, Yan E. Wang, and Gerbrand Ceder. First-Principles Studies on Cation Dopants and Electrolyte—Cathode Interphases for Lithium Garnets. 27(11):4040–4047.

[34] Iek-Heng Chu, Han Nguyen, Sunny Hy, Yuh-Chieh Lin, Zhenbin Wang, Zihan Xu, Zhi Deng, Ying Shirley Meng, and Shyue Ping Ong. Insights into the Performance Limits of the Li 7 P 3 S 11 Superionic Conductor: A Combined First-Principles and Experimental Study. 8(12):7843–7853.

[35] Shyue Ping Ong, Lei Wang, Byoungwoo Kang, and Gerbrand Ceder. Li-Fe-P-O2 Phase Diagram from First Principles Calculations. 20(5):1798–1807.

[36] Denis Kramer and Gerbrand Ceder. Tailoring the Morphology of LiCoO 2 : A First Principles Study. 21(16):3799–3809.

[37] Jun Haruyama, Keitaro Sodeyama, Liyuan Han, Kazunori Takada, and Yoshitaka Tateyama. Space–Charge Layer Effect at Interface between Oxide Cathode and Sulfide Electrolyte in All-Solid-State Lithium-Ion Battery. 26(14):4248–4255.

[38] Daniele Stradi, Line Jelver, Søren Smidstrup, and Kurt Stokbro. Method for determining optimal supercell representation of interfaces. 29(18):185901.

[39] Shyue Ping Ong, Shreyas Cholia, Anubhav Jain, Miriam Brafman, Dan Gunter, Gerbrand Ceder, and Kristin a. Persson. The Materials Application Programming Interface (API): A simple, flexible and efficient API for materials data based on REpresentational State Transfer (REST) principles. 97:209–215.

[40] J.-M. Tarascon and M. Armand. Issues and challenges facing rechargeable lithium batteries. 414(6861):359–367.

[41] Michael D. Slater, Donghan Kim, Eungje Lee, and Christopher S. Johnson. Sodium-Ion Batteries. 23(8):947–958.

[42] Verónica Palomares, Paula Serras, Irune Villaluenga, Karina B. Hueso, Javier Carretero-González, and Teófilo Rojo. Na-ion batteries, recent advances and present challenges to become low cost energy storage systems. 5(3):5884.

[43] Sung-Wook Kim, Dong-Hwa Seo, Xiaohua Ma, Gerbrand Ceder, and Kisuk Kang. Electrode Materials for Rechargeable Sodium-Ion Batteries: Potential Alternatives to Current Lithium-Ion Batteries. 2(7):710–721.

[44] Shyue Ping Ong, Vincent L. Chevrier, Geoffroy Hautier, Anubhav Jain, Charles Moore, Sangtae Kim, Xiaohua Ma, and Gerbrand Ceder. Voltage, stability and diffusion barrier differences between sodium-ion and lithium-ion intercalation materials. 4(9):3680.

[45] B. Dunn, H. Kamath, and J.-M. Tarascon. Electrical Energy Storage for the Grid: A Battery of Choices. 334(6058):928–935.

[46] Fangyi Cheng, Jing Liang, Zhanliang Tao, and Jun Chen. Functional Materials for Rechargeable Batteries. 23(15):1695–1715.

[47] Kuppan Saravanan, Chad W. Mason, Ashish Rudola, Kim Hai Wong, and Palani Balaya. The First Report on Excellent Cycling Stability and Superior Rate Capability of Na $_3$ V $_2$ (PO $_4$) $_3$ for Sodium Ion Batteries. 3(4):444–450.

[48] Wei Shen, Cong Wang, Haimei Liu, and Wensheng Yang. Towards Highly Stable Storage of Sodium Ions: A Porous Na $_3$ V $_2$ (PO $_4$) $_3$ /C Cathode Material for Sodium-Ion Batteries. 19(43):14712–14718.

[49] Changbao Zhu, Kepeng Song, Peter A. van Aken, Joachim Maier, and Yan Yu. Carbon-Coated Na $_3$ V $_2$ (PO $_4$) $_3$ Embedded in Porous Carbon Matrix: An Ultrafast Na-Storage Cathode with the Potential of Outperforming Li Cathodes. 14(4):2175–2180.

[50] Shuo Li, Yifan Dong, Lin Xu, Xu Xu, Liang He, and Liqiang Mai. Effect of Carbon Matrix Dimensions on the Electrochemical Properties of Na $_3$ V $_2$ (PO $_4$) $_3$ Nanograins for High-Performance Symmetric Sodium-Ion Batteries. 26(21):3545–3553.

[51] Hui Li, Ying Bai, Feng Wu, Yu Li, and Chuan Wu. Budding willow branches shaped Na3V2(PO4)3/C nanofibers synthesized via an electrospinning technique and used as cathode material for sodium ion batteries. 273:784–792.

[52] Zelang Jian, Wenze Han, Xia Lu, Huaixin Yang, Yong-Sheng Hu, Jing Zhou, Zhibin Zhou, Jianqi Li, Wen Chen, Dongfeng Chen, and Liquan Chen. Superior Electrochemical Performance and Storage Mechanism of Na $_3$ V $_2$ (PO $_4$) $_3$ Cathode for Room-Temperature Sodium-Ion Batteries. 3(2):156–160.

[53] Yongjin Fang, Lifen Xiao, Xinping Ai, Yuliang Cao, and Hanxi Yang. Hierarchical Carbon Framework Wrapped Na $_3$ V $_2$ (PO $_4$) $_3$ as a Superior High-Rate and Extended Lifespan Cathode for Sodium-Ion Batteries. 27(39):5895–5900.

[54] Hui Li, Ying Bai, Feng Wu, Qiao Ni, and Chuan Wu. Na3V2(PO4)3/C nanorods as advanced cathode material for sodium ion batteries. 278:281–286.

[55] Ke Du, Hongwei Guo, Guorong Hu, Zhongdong Peng, and Yanbing Cao. Na3V2(PO4)3 as cathode material for hybrid lithium ion batteries. 223:284–288.

[56] Hailong Fei, Xiaomin Wu, Huan Li, and Mingdeng Wei. Novel sodium intercalated (NH4)2V6O16 platelets: High performance cathode materials for lithium-ion battery. 415:85–88.

[57] Shi Tao, Peixin Cui, Weifeng Huang, Zhen Yu, Xingbo Wang, Shenghui Wei, Daobin Liu, Li Song, and Wangsheng Chu. Sol–gel design strategy for embedded Na3V2(PO4)3 particles into carbon matrices for high-performance sodium-ion batteries. 96:1028–1033.

[58] Hui Li, Xuanxuan Bi, Ying Bai, Yifei Yuan, Reza Shahbazian-Yassar, Chuan Wu, Feng Wu, Jun Lu, and Khalil Amine. High-Rate, Durable Sodium-Ion Battery Cathode Enabled by Carbon-Coated Micro-Sized Na $_3$ V $_2$ (PO $_4$) $_3$ Particles with Interconnected Vertical Nanowalls. 3(9):1500740.

[59] Wei Wang, Bo Jiang, Liwen Hu, Zheshuai Lin, Jungang Hou, and Shuqiang Jiao. Single crystalline VO2 nanosheets: A cathode material for sodium-ion batteries with high rate cycling performance. 250:181–187.

[60] Sung-Yoon Chung, Jason T. Bloking, and Yet-Ming Chiang. Electronically conductive phospho-olivines as lithium storage electrodes. 1(2):123–128.

[61] Hui Li, Chuan Wu, Ying Bai, Feng Wu, and Muzi Wang. Controllable synthesis of high-rate and long cycle-life Na3V2(PO4)3 for sodium-ion batteries. 326:14–22.

[62] Hui Li, Xiqian Yu, Ying Bai, Feng Wu, Chuan Wu, Liang-Yu Liu, and Xiao-Qing Yang. Effects of Mg doping on the remarkably enhanced electrochemical performance of Na $_3$ V $_2$ (PO $_4$) $_3$ cathode materials for sodium ion batteries. 3(18):9578–9586.

[63] M. J. Aragón, P. Lavela, G. F. Ortiz, and J. L. Tirado. Effect of Iron Substitution in the Electrochemical Performance of Na $_3$ V $_2$ (PO $_4$) $_3$ as Cathode for Na-Ion Batteries. 162(2):A3077–A3083.

[64] María J. Aragón, Pedro Lavela, Gregorio F. Ortiz, and José L. Tirado. Benefits of Chromium Substitution in Na $_3$ V $_2$ (PO $_4$) $_3$ as a Potential Candidate for Sodium-Ion Batteries. 2(7):995–1002.

[65] M.J. Aragón, P. Lavela, R. Alcántara, and J.L. Tirado. Effect of aluminum doping on carbon loaded Na3V2(PO4)3 as cathode material for sodium-ion batteries. 180:824–830.

[66] R. Klee, P. Lavela, M.J. Aragón, R. Alcántara, and J.L. Tirado. Enhanced high-rate performance of manganese substituted Na 3 V 2 (PO 4) 3 /C as cathode for sodium-ion batteries. 313:73–80.

[67] Wei Shen, Hui Li, Ziyang Guo, Zhihong Li, Qunjie Xu, Haimei Liu, and Yonggang Wang. Improvement on the high-rate performance of Mn-doped Na $_3$ V $_2$ (PO $_4$) $_3$ /C as a cathode material for sodium ion batteries. 6(75):71581–71588.

[68] Hui Li, Ying Bai, Feng Wu, Qiao Ni, and Chuan Wu. Na-Rich Na $_{3+x}$ V $_{2-x}$ Ni $_x$ (PO $_4$) $_3$ /C for Sodium Ion Batteries: Controlling the Doping Site and Improving the Electrochemical Performances. 8(41):27779–27787.

[69] G Kresse and J Furthmüller. Efficient iterative schemes for ab initio total-energy calculations using a plane-wave basis set. 54(16):11169–11186.

[70] P. E. Blöchl. Projector augmented-wave method. 50(24):17953–17979.

[71] John P. Perdew, Kieron Burke, and Matthias Ernzerhof. Generalized Gradient Approximation Made Simple. 77(18):3865–3868.

[72] G. Bergerhoff, R. Hundt, R. Sievers, and I. D. Brown. The inorganic crystal structure data base. 23(2):66–69.

[73] Gus L. W. Hart and Rodney W. Forcade. Algorithm for generating derivative structures. 77(22):224115.

[74] Su-Huai Wei and S. B. Zhang. Chemical trends of defect formation and doping limit in II-VI semiconductors: The case of CdTe. 66(15):155211.

[75] Sung-Yoon Chung and Yet-Ming Chiang. Microscale Measurements of the Electrical Conductivity of Doped LiFePO[sub 4]. 6(12):A278.

[76] Nonglak Meethong, Yu-Hua Kao, Scott A. Speakman, and Yet-Ming Chiang. Aliovalent Substitutions in Olivine Lithium Iron Phosphate and Impact on Structure and Properties. 19(7):1060–1070.

[77] K. Y. Li, J. J. Shao, and D. F. Xue. Calculation of impurity energy levels of transition metal ions in inorganic crystals based on electronegativity. 17(4):218–223.

[78] Dong-Wook Han, Sung-Jin Lim, Yong-Il Kim, Seung Ho Kang, Yoon Cheol Lee, and Yong-Mook Kang. Facile Lithium Ion Transport through Superionic Pathways Formed on the Surface of Li $_3$ V $_2$ (PO $_4$) $_3$ /C for High Power Li Ion Battery. 26(12):3644–3650.

[79] Wei Shen, Cong Wang, Qunjie Xu, Haimei Liu, and Yonggang Wang. Nitrogen-Doping-Induced Defects of a Carbon Coating Layer Facilitate Na-Storage in Electrode Materials. 5(1):1400982.

[80] Bo Wang, Binghui Xu, Tiefeng Liu, Peng Liu, Chenfeng Guo, Shuo Wang, Qiuming Wang, Zhigang Xiong, Dianlong Wang, and X. S. Zhao. Mesoporous carbon-coated LiFePO $_4$ nanocrystals co-modified with graphene and Mg $^{2+}$ doping as superior cathode materials for lithium ion batteries. 6(2):986–995.

[81] Kyu-Sung Park, Penghao Xiao, So-Yeon Kim, Anthony Dylla, Young-Min Choi, Graeme Henkelman, Keith J. Stevenson, and John B. Goodenough. Enhanced Charge-Transfer Kinetics by Anion Surface Modification of LiFePO $_4$. 24(16):3212–3218.

[82] Yongmin Wu, Zhenhai Wen, and Jinghong Li. Hierarchical Carbon-Coated LiFePO4 Nanoplate Microspheres with High Electrochemical Performance for Li-Ion Batteries. 23(9):1126–1129.

[83] Guangyin Li, Zhenlei Huang, Zicheng Zuo, Zhanjun Zhang, and Henghui Zhou. Understanding the trace Ti surface doping on promoting the low temperature performance of LiNi 1/3 Co 1/3 Mn 1/3 O 2 cathode. 281:69–76.

[84] M. Armand and J.-M. Tarascon. Building better batteries. 451(7179):652–657.

[85] Jürgen Janek and Wolfgang G. Zeier. A solid future for battery development. 1(9):16141.

[86] J.B. Goodenough, H.Y-P. Hong, and J.A. Kafalas. Fast Na+-ion transport in skeleton structures. 11(2):203–220.

[87] Yoshiyuki Inaguma, Chen Liquan, Mitsuru Itoh, and Tetsuro Nakamura. High Ionic Conductivity in Lithium Lanthanum Titanate. 86(10):689–693.

[88] Ramaswamy Murugan, Venkataraman Thangadurai, and Werner Weppner. Fast Lithium Ion Conduction in Garnet-Type Li7La3Zr2O12. 46(41):7778–7781.

[89] Noriaki Kamaya, Kenji Homma, Yuichiro Yamakawa, Masaaki Hirayama, Ryoji Kanno, Masao Yonemura, Takashi Kamiyama, Yuki Kato, Shigenori Hama, Koji Kawamoto, and Akio Mitsui. A lithium superionic conductor. 10(9):682–686.

[90] Yoshikatsu Seino, Tsuyoshi Ota, Kazunori Takada, Akitoshi Hayashi, and Masahiro Tatsumisago. A sulphide lithium super ion conductor is superior to liquid ion conductors for use in rechargeable batteries. 7(2):627–631.

[91] Akitoshi Hayashi, Kousuke Noi, Atsushi Sakuda, and Masahiro Tatsumisago. Superionic glass-ceramic electrolytes for room-temperature rechargeable sodium batteries. 3(1):856.

[92] Yuki Kato, Satoshi Hori, Toshiya Saito, Kota Suzuki, Masaaki Hirayama, Akio Mitsui, Masao Yonemura, Hideki Iba, and Ryoji Kanno. High-power all-solid-state batteries using sulfide superionic conductors. 1(4):16030.

[93] Masahiro Tatsumisago and Akitoshi Hayashi. Sulfide Glass-Ceramic Electrolytes for All-Solid-State Lithium and Sodium Batteries. 5(3):226–235.

[94] Akitoshi Hayashi, Kousuke Noi, Naoto Tanibata, Motohiro Nagao, and Masahiro Tatsumisago. High sodium ion conductivity of glass–ceramic electrolytes with cubic Na3PS4. 258:420–423.

[95] Abhik Banerjee, Kern Ho Park, Jongwook W. Heo, Young Jin Nam, Chang Ki Moon, Seung M. Oh, Seung-Tae Hong, and Yoon Seok Jung. Na_3SbS_4 : A Solution Processable Sodium Superionic Conductor for All-Solid-State Sodium-Ion Batteries. 128(33):9786–9790.

[96] Zhaoxin Yu, Shun-Li Shang, Joo-Hwan Seo, Daiwei Wang, Xiangyi Luo, Qingquan Huang, Shuru Chen, Jun Lu, Xiaolin Li, Zi-Kui Liu, and Donghai Wang. Exceptionally High Ionic Conductivity in $Na_3P_{0.62}As_{0.38}S_4$ with Improved Moisture Stability for Solid-State Sodium-Ion Batteries. 29(16):1605561.

[97] Rayavarapu Prasada Rao, Haomin Chen, Lee Loong Wong, and Stefan Adams. $Na_{3+x}M_xP_{1-x}S_4$ ($M = Ge^{4+}$, Ti^{4+}, Sn^{4+}) enables high rate all-solid-state Na-ion batteries $Na_{2+2\delta}Fe_{2-\delta}(SO_4)_3$ —$Na_{3+x}M_xP_{1-x}S_4$ —$Na_2Ti_3O_7$. 5(7):3377–3388.

[98] Sebastian Wenzel, Thomas Leichtweiss, Dominik A. Weber, Joachim Sann, Wolfgang G. Zeier, and Jürgen Janek. Interfacial Reactivity Benchmarking of the Sodium Ion Conductors Na 3 PS 4 and Sodium β-Alumina for Protected Sodium Metal Anodes and Sodium All-Solid-State Batteries. 8(41):28216–28224.

[99] Xiaogang Han, Yunhui Gong, Kun (Kelvin) Fu, Xingfeng He, Gregory T Hitz, Jiaqi Dai, Alex Pearse, Boyang Liu, Howard Wang, Gary Rubloff, Yifei Mo, Venkataraman Thangadurai, Eric D Wachsman, and Liangbing Hu. Negating interfacial impedance in garnet-based solid-state Li metal batteries. 16(5):572–579.

[100] N. Ohta, K. Takada, L. Zhang, R. Ma, M. Osada, and T. Sasaki. Enhancement of the High-Rate Capability of Solid-State Lithium Batteries by Nanoscale Interfacial Modification. 18(17):2226–2229.

[101] Narumi Ohta, Kazunori Takada, Isao Sakaguchi, Lianqi Zhang, Renzhi Ma, Katsutoshi Fukuda, Minoru Osada, and Takayoshi Sasaki. LiNbO3-coated LiCoO2 as cathode material for all solid-state lithium secondary batteries. 9(7):1486–1490.

[102] Kazunori Takada, Narumi Ohta, Lianqi Zhang, Katsutoshi Fukuda, Isao Sakaguchi, Renzhi Ma, Minoru Osada, and Takayoshi Sasaki. Interfacial modification for high-power solid-state lithium batteries. 179(27-32):1333–1337.

[103] P. Ganesh, P. R. C. Kent, and De-en Jiang. Solid–Electrolyte Interphase Formation and Electrolyte Reduction at Li-Ion Battery Graphite Anodes: Insights from First-Principles Molecular Dynamics. 116(46):24476–24481.

[104] P. Ganesh, De-en Jiang, and P. R. C. Kent. Accurate Static and Dynamic Properties of Liquid Electrolytes for Li-Ion Batteries from ab initio Molecular Dynamics. 115(12):3085–3090.

[105] Anubhav Jain, Geoffroy Hautier, Shyue Ping Ong, Charles J. Moore, Christopher C. Fischer, Kristin A. Persson, and Gerbrand Ceder. Formation enthalpies by mixing GGA and GGA + U calculations. 84(4):045115.

[106] M. Parrinello and A. Rahman. Crystal Structure and Pair Potentials: A Molecular-Dynamics Study. 45(14):1196–1199.

[107] Long Zhang, Dechao Zhang, Kun Yang, Xinlin Yan, Limin Wang, Jianli Mi, Bo Xu, and Yueming Li. Vacancy-Contained Tetragonal Na 3 SbS 4 Superionic Conductor. 3(10):1600089.

[108] Zonghai Chen, Yan Qin, Khalil Amine, and Yang-Kook Sun. Role of surface coating on cathode materials for lithium-ion batteries. 20:7606–7612.

[109] Yu He, Xiqian Yu, Yanhong Wang, Hong Li, and Xuejie Huang. Alumina-Coated Patterned Amorphous Silicon as the Anode for a Lithium-Ion Battery with High Coulombic Effi ciency. 23:4938–4941.

[110] Jaephil Cho, Yong Jeong Kim, and Byungwoo Park. Novel LiCoO 2 Cathode Material with Al 2 O 3 Coating for a Li Ion Cell. 4(12):3788–3791.

[111] Nulati Yesibolati, Muhammad Shahid, Wei Chen, M. N. Hedhili, M. C. Reuter, F. M. Ross, and H. N. Alshareef. SnO2 anode surface passivation by atomic layer deposited HfO2 improves li-ion battery performance. 10(14):2849–2858.

[112] Bilal Ahmed, Dalaver H. Anjum, Mohamed N. Hedhili, and Husam N. Alshareef. Mechanistic Insight into the Stability of HfO 2 -Coated MoS 2 Nanosheet Anodes for Sodium Ion Batteries. 11(34):4341–4350.

[113] Kevin Leung. Predicting the voltage dependence of interfacial electrochemical processes at lithium-intercalated graphite edge planes. 17(3):1637–1643.

[114] Zhonghui Gao, Huabin Sun, Lin Fu, Fangliang Ye, Yi Zhang, Wei Luo, and Yunhui Huang. Promises, Challenges, and Recent Progress of Inorganic Solid-State Electrolytes for All-Solid-State Lithium Batteries. 30(17):1705702.

[115] Arumugam Manthiram, Xingwen Yu, and Shaofei Wang. Lithium battery chemistries enabled by solid-state electrolytes. 2(4):16103.

[116] Zhi Deng, Zhenbin Wang, Iek-Heng Chu, Jian Luo, and Shyue Ping Ong. Elastic Properties of Alkali Superionic Conductor Electrolytes from First Principles Calculations. 163(2):A67–A74.

[117] Masahiro Tatsumisago, Motohiro Nagao, and Akitoshi Hayashi. Recent development of sulfide solid electrolytes and interfacial modification for all-solid-state rechargeable lithium batteries. 1(1):17–25.

[118] Lin Xu, Shun Tang, Yu Cheng, Kangyan Wang, Jiyuan Liang, Cui Liu, Yuan-Cheng Cao, Feng Wei, and Liqiang Mai. Interfaces in Solid-State Lithium Batteries. 2(10):1991–2015.

[119] Fudong Han, Yizhou Zhu, Xingfeng He, Yifei Mo, and Chunsheng Wang. Electrochemical Stability of $Li_{10}GeP_2S_{12}$ and $Li_7La_3Zr_2O_{12}$ Solid Electrolytes. 6(8):1501590.

[120] Jérémie Auvergniot, Alice Cassel, Jean-Bernard Ledeuil, Virginie Viallet, Vincent Seznec, and Rémi Dedryvère. Interface Stability of Argyrodite Li_6PS_5Cl toward $LiCoO_2$, $LiNi_{1/3}Co_{1/3}Mn_{1/3}O_2$, and $LiMn_2O_4$ in Bulk All-Solid-State Batteries. 29(9):3883–3890.

[121] Jae Ha Woo, Jonathan J. Travis, Steven M. George, and Se-Hee Lee. Utilization of Al_2O_3 Atomic Layer Deposition for Li Ion Pathways in Solid State Li Batteries. 162(3):A344–A349.

[122] Wenbo Zhang, Dominik A. Weber, Harald Weigand, Tobias Arlt, Ingo Manke, Daniel Schröder, Raimund Koerver, Thomas Leichtweiss, Pascal Hartmann, Wolfgang G. Zeier, and Jürgen Janek. Interfacial Processes and Influence of Composite Cathode Microstructure Controlling the Performance of All-Solid-State Lithium Batteries. 9(21):17835–17845.

[123] Nan Jiang, Qing Tang, Meili Sheng, Bo You, De-en Jiang, and Yujie Sun. Nickel sulfides for electrocatalytic hydrogen evolution under alkaline conditions: A case study of crystalline NiS, NiS_2, and Ni_3S_2 nanoparticles. 6(4):1077–1084.

[124] Christian Dietrich, Raimund Koerver, Michael W. Gaultois, Gregor Kieslich, Giannantonio Cibin, Jürgen Janek, and Wolfgang G. Zeier. Spectroscopic characterization of lithium thiophosphates by XPS and XAS – a model to help monitor interfacial reactions in all-solid-state batteries. 20(30):20088–20095.

[125] Naoto Tanibata, Minako Deguchi, Akitoshi Hayashi, and Masahiro Tatsumisago. All-Solid-State Na/S Batteries with a Na $_3$ PS $_4$ Electrolyte Operating at Room Temperature. 29(12):5232–5238.

[126] Jinglei Lei, Frank McLarnon, and Robert Kostecki. In Situ Raman Microscopy of Individual LiNi $_{0.8}$ Co $_{0.15}$ Al $_{0.05}$ O $_2$ Particles in a Li-Ion Battery Composite Cathode. 109(2):952–957.

[127] T. Suzuki, K. Uchinokura, T. Sekine, and E. Matsuura. Raman scattering of NiS2. 23(11):847–852.

[128] Naoaki Kuwata, Naoya Iwagami, Yoshinari Tanji, Yasutaka Matsuda, and Junichi Kawamura. Characterization of Thin-Film Lithium Batteries with Stable Thin-Film Li[sub 3]PO[sub 4] Solid Electrolytes Fabricated by ArF Excimer Laser Deposition. 157(4):A521.

[129] Yulong Sun, Kota Suzuki, Kosuke Hara, Satoshi Hori, Taka-aki Yano, Masahiko Hara, Masaaki Hirayama, and Ryoji Kanno. Oxygen substitution effects in Li10GeP2S12 solid electrolyte. 324:798–803.

[130] Takashi Hakari, Minako Deguchi, Kei Mitsuhara, Toshiaki Ohta, Kohei Saito, Yuki Orikasa, Yoshiharu Uchimoto, Yoshiyuki Kowada, Akitoshi Hayashi, and Masahiro Tatsumisago. Structural and Electronic-State Changes of a Sulfide Solid Electrolyte during the Li Deinsertion–Insertion Processes. 29(11):4768–4774.

[131] Raimund Koerver, Felix Walther, Isabel Aygün, Joachim Sann, Christian Dietrich, Wolfgang G. Zeier, and Jürgen Janek. Redox-active cathode interphases in solid-state batteries. 5(43):22750–22760.

[132] Zhuoying Zhu, Iek Heng Chu, and Shyue Ping Ong. Li3Y(PS4)2 and Li5PS4Cl2: New Lithium Superionic Conductors Predicted from Silver Thiophosphates using Efficiently Tiered Ab Initio Molecular Dynamics Simulations. 29(6):2474–2484.